ÉCOLE CENTRALE PARIS
LABORATOIRE DE MÉCANIQUE
SOLS, STRUCTURES ET MATÉRIAUX
GRANDE VOIE DES VIGNES, F-92295 CHATENAY MALABRY

FACULTEIT TOEGEPASTE WETENSCHAPPEN
DEPARTEMENT BURGERLIJKE BOUWKUNDE
AFDELING BOUWMECHANICA
KASTEELPARK ARENBERG 40 B-3001 HEVERLEE

KATHOLIEKE
UNIVERSITEIT
LEUVEN

Three-dimensional modelling of free field and structural vibration due to harmonic and transient loading in a tunnel

Promotoren:
Dr. ir. D. Clouteau
Prof. dr. ir. G. Degrande
Assessoren:
Dr. ir. G. Lombaert
Dr. ir. P. Chatterjee

Eindwerk voorgedragen tot het verkrijgen van de graad van Burgerlijk Bouwkundig Ingenieur

door

Maarten ARNST

E2003

Leuven, april 2003.

Voorwoord

Dit eindwerk besluit voor mij de studie voor burgerlijk bouwkundig ingenieur aan de Katholieke Universiteit Leuven. In de ingenieursjaren boeiden de vakken van de afdeling bouwmechanica mij het meest en een keuze voor een eindwerk aan deze afdeling lag dan ook voor de hand. De afdeling bouwmechanica werkt reeds lange tijd samen met de Ecole Centrale in Parijs voor de studie van grond-structuur-interactie problemen. Binnen het kader van het Europese onderzoeksproject CONVURT bestond de mogelijkheid om gedurende een vijftal maanden mee te werken aan dit project aan de Ecole Centrale. Van deze mogelijkheid heb ik heel graag gebruik gemaakt en in de periode van september 2002 tot februari 2003 studeerde ik aan de Ecole Centrale in Parijs. In de onderzoeksgroep van Dr. Didier Clouteau werkte ik mee aan gevarieerde thema's binnen het onderzoek naar trillingen in gebouwen voortgebracht door metroverkeer. Ik kreeg er ook de kans een aantal vakken te volgen uit de specialisatie-opleiding 'Dynamique des structures et systèmes couplés'. Deze vakken waren niet alleen heel nuttig voor dit eindwerk, maar ik heb ze ook met zeer veel interesse gevolgd.

Ik zou van dit voorwoord willen gebruik maken om een aantal mensen te bedanken. Tout d'abord, j'aimerais bien remercier dr. Didier Clouteau qui m'a accueilli dans l'équipe structures à l'Ecole Centrale de Paris. L'équipe structures est une équipe très agréable et très ouverte, dans laquelle j'ai vraiment aimé mon séjour. J'aimerais bien remercier Dr. Didier Clouteau de son aide et de la variété de sujets de recherche qu'il m'a offerts dans le cadre du projet. Je remercie Nader, Gérald, Rémi, Ramzi, Adrien, Eric, Guillaume, Tuan Ahn, Oscar, Christophe, Regis, prof. Al Hussaini, prof. Aubry, dr. Balmes et tous les autres de leur aide, de nos soirées amusantes ensemble, des petites heures de sport,...

Ik zou ook graag mijn promotor, prof. Geert Degrande, bedanken om dit eindwerk te hebben ondersteund zowel voor, tijdens, als na mijn verblijf aan de Ecole Centrale. Ik zou ook Pranesh, Lincy en Geert willen bedanken bij wie ik ook steeds terecht kon met vragen.

Ook de Fondation Biermans-Lapôtre zou ik graag bedanken voor de schitterende woonaccomodatie in Parijs. De mensen die met mij op de vierde verdieping woonden, zou ik graag bedanken voor de gezellige uurtjes 's avonds.

Er zijn ook veel mensen die zeer belangrijk zijn, en dit zeker niet alleen tijdens dit eindwerk. Mijn ouders en broers zou ik daarom graag bedanken voor hun steun en interesse op alle momenten. En ook mijn vrienden wil ik bedanken voor deze vijf toffe jaren zowel in Leuven, als tot ver erbuiten.

Maarten Arnst
Leuven, april 2003.

Contents

Table of contents . . . iii
List of figures . . . vii
List of tables . . . xi

1 Introduction **1**

2 Periodic soil-structure interaction **3**
2.1 The general soil-structure interaction problem . . . 3
2.1.1 Notations and general equations . . . 3
2.1.2 Domain decomposition . . . 5
2.1.3 Variational formulation . . . 6
2.1.4 The boundary element method . . . 8
2.1.5 The soil impedance . . . 9
2.1.6 The forces induced by the incident field . . . 10
2.2 The periodic soil-structure interaction problem . . . 11
2.2.1 The Floquet Transformation . . . 11
2.2.2 Soil-structure interaction in the frequency-wavenumber domain . . . 12
2.2.3 Domain decomposition in the frequency-wavenumber domain . . . 13
2.2.4 Variational formulation in the frequency-wavenumber domain . . . 13
2.2.5 The periodic boundary element method . . . 15
2.2.6 The kinematic basis for the structure . . . 17
2.2.7 The computation for the negative wavenumbers . . . 18
2.2.8 The symmetry of the kinematical basis. . . . 19

3 Optimisation of the periodic BEM implementation **22**
3.1 A description of the old implementation . . . 22
3.2 Profiling of the old implementation . . . 23

3.3 Optimisation in two stages . . . 24
3.4 Optimisation results . . . 25
3.5 Conclusions and perspectives . . . 26

4 Numerical model of the Cité Universitaire site in Paris 27
4.1 Introduction . . . 27
4.2 The applied forces . . . 29
4.3 The visualization model . . . 29
4.4 The convergence analysis . . . 30
4.4.1 The reduced modal basis . . . 30
4.4.2 The periodic boundary element method . . . 32
4.4.3 The sampling in the wavenumber-frequency domain . . . 32
4.5 The generalized impedance of the tunnel and of the soil . . . 33

5 Impulse loads on a tunnel invert: response in the free field 35
5.1 The transfer functions in the spatial-frequency domain . . . 35
5.2 The response on harmonic loads on the tunnel invert . . . 36
5.3 The transfer functions in the slowness-frequency domain . . . 39
5.3.1 A first simplified model: an infinite plate . . . 39
5.3.2 The influence of the plate curvature . . . 41
5.3.3 A second simplified model: an infinite soil layer on an infinite plate . . . 41
5.3.4 A third simplified model: an infinite plate on an elastic half space . . . 45
5.4 The response on transient loads on the tunnel invert . . . 46
5.4.1 The transient tunnel excitation . . . 46
5.4.2 The transient tunnel response . . . 47
5.5 Conclusion and further development . . . 52

6 Impulse loads on a tunnel invert: response in a nearby building 54
6.1 The characteristics of the building . . . 54
6.1.1 The location of the "Maison du Mexique" with respect to the tunnel . . . 54
6.1.2 Material properties and geometrical characteristics of the building frame . 56
6.1.3 The constraint equations . . . 57
6.1.4 The foundation of the building . . . 58
6.2 The dynamic soil-structure interaction analysis . . . 58
6.2.1 The kinematic basis . . . 58

6.2.2 The variational formulation . . . 59
6.2.3 The numerical implementation . . . 61
6.3 The building response on harmonic loads on the tunnel invert . . . 64
6.4 The transfer functions . . . 68
6.5 Conclusion and further development . . . 70

A Matlab and MISS input files: the harmonic response of the tunnel-soil-system 72
A.1 The problem characteristics . . . 72
A.2 The Matlab pre-processing results files . . . 73
A.3 The MISS processing . . . 73
A.3.1 Description . . . 73
A.3.2 The MISS input files . . . 73
A.3.3 The MISS program . . . 73
A.3.4 The MISS output files . . . 74
A.4 The Matlab-SDT post processing . . . 74
A.4.1 Description . . . 74
A.4.2 The MISS-Matlab coupling routines . . . 74
A.4.3 The post processing routines . . . 74
A.5 The Animations . . . 75

B Matlab and MISS input files: the transient response of the tunnel-soil-system 76
B.1 The problem characteristics . . . 76
B.2 The pre-processing . . . 76
B.3 The processing . . . 77
B.3.1 Description . . . 77
B.3.2 The processing files . . . 77
B.4 The animations . . . 77

C Matlab and MISS input files: the harmonic response of the tunnel-soil-building system 78
C.1 The problem characteristics . . . 78
C.2 The Matlab and MISS pre-processing . . . 79
C.2.1 Description . . . 79
C.2.2 The construction of the building model . . . 79
C.3 The MISS processing . . . 82

C.3.1 Description 82
C.3.2 The MISS input files 82
C.3.3 The MISS program 82
C.3.4 The MISS output files 82
C.4 The Matlab postprocessing 82

List of Figures

1 The model layout and notations. . . . 3
2 The radiated field. . . . 6
3 The locally diffracted field. . . . 6
4 The normal vectors $\boldsymbol{n}^{int}$ and $\boldsymbol{n}^{ext}$. . . . 10
5 A very long periodic structure and the restriction to a single generic cell, introducing new interfaces. . . . 13

1 The plan of the test site. . . . 28
2 The metro tunnel at the station Cité Universitaire. . . . 28
3 The cross section of the metro tunnel. . . . 28
4 The model of the cross section of the tunnel and soil characteristics. . . . 29
5 The single generic cell and the position of the applied forces. . . . 29
6 The tunnel, the non-moving force and the free surface. . . . 30
7 Mode 11 at 57.6 Hz (Only x-z displacements). . . . 30
8 Mode 17 at 101.5 Hz (only y-displacements). . . . 30
9 The amplitude of the vertical displacement in the tunnel point under the force, computed with different numbers of modes. . . . 31
10 The real part of element (11,11) of the soil impedance matrix for p=0 s/m and for different numbers N_c. . . . 32
11 The amplitude of the vertical displacement in the wavenumber domain for f=5 Hz for different tunnel points. . . . 33
12 The amplitude of the vertical velocity in the slowness-frequency domain in the tunnel point under the force. . . . 33
13 The real part of the element (11,11) of the generalized tunnel impedance matrix. 33
14 The real part of element (11,11) of the generalized tunnel impedance matrix for slowness p=0 s/m. . . . 33
15 The real part of the element (11,11) of the soil impedance matrix. . . . 34
16 The imaginary part of element (11,11) of the soil impedance matrix. . . . 34

1 The amplitude of the vertical displacement in points at the free surface. 35

2 The amplitude of the vertical displacement of tunnel points and points at the free surface. 35

3 The harmonic response of the tunnel and the free field at 14 Hz at the time steps t=0 s, t=$T/8$, t=$T/4$ and t=$3T/8$ respectively, with the period T=1/14 s. 36

4 The harmonic response of the tunnel and the free field at 80 Hz at the timesteps t=0 s, t=$T/8$, t=$T/4$ and t=$3T/8$ respectively, with the period T=1/80 s. 37

5 The harmonic response of the tunnel at 80 Hz at the timesteps t=0 s and t=$T/8$ with T=1/80 s. 38

6 The phase of the vertical displacement at the free surface along a line in the y-direction at x=-4 m at 80 Hz. 38

7 The amplitude of the vertical velocity in a point at the tunnel roof in the frequency-slowness domain. 39

8 The amplitude of the vertical velocity in a point at the tunnel invert in the frequency-slowness domain. 39

9 The model of an infinite plate. 39

10 The dispersion curves for a plate with thickness 0.6 m and for a plate with thickness 1.5 m. Ths slowness (the inverse of the phase speed determined by the dispersion relation (5.4) is shown in function of the frequency. 40

11 The model of an infinite layer on an infinite plate. 41

12 The amplitude of the vertical velocity in a point at the tunnel roof for a force applied at the tunnel invert in the frequency-slowness domain. 44

13 The amplitude of the vertical velocity in a point at the tunnel roof for a force applied at the tunnel roof in the frequency-slowness domain. 44

14 The dispersion curves of the infinite soil layer on an infinite plate model in the frequency-slowness domain. 44

15 The dispersion curves of an infinite soil layer on infinite plate system on top of the amplitude of the vertical velocity in a point at the tunnel roof for a force applied at the tunnel roof in the frequency-slowness domain. (more contours than in figure 13 are shown.) 44

16 The dispersion curves of a free plate with the characteristics of the bottom plate of the tunnel; of a free plate with the double thickness of the tunnel bottom plate of the tunnel. c_p and c_s are the phase speeds of the third soil layer. 45

17 The modulus of the determinant divided by ω^2 of the infinite plate on elastic half space model versus slowness and frequency (for a plate with thickness 0.4 m). The colour scale is logaritmic. 45

18 Time history of the applied Gaussian force (t_1=0.1 s, t_2=1.1 s and T=0.0025 s). 46

19 Frequency content of the applied Gaussian force. 46

20 The response of the tunnel and the free field on the downwards Gaussian hammer impact at the timesteps t=0.1 s, t=0.116 s, t=0.136 s and t=0.0156 s, respectively. 48

21 The seismogram of the vertical displacements for points on a line y=0 at the free surface for the Gaussian transient force applied at the tunnel invert. 49

22 The seismogram of the horizontal displacements for points on a line y=0 at the free surface for the Gaussian transient force applied at the tunnel invert. 49

23 The amplitude of the vertical displacement in the $\omega - p$ domain for a vertical Dirac impulse applied at a depth of 0 m. 50

24 The seismogram of the vertical displacements for points on a line y=0 at the free surface for the Gaussian transient force applied at a depth of 0 m. 50

25 The amplitude of the vertical displacement in the $\omega - p$ domain for a vertical Dirac impulse applied at a depth of 3 m. 50

26 The seismogram of the vertical displacements for points on a line y=0 at the free surface for the Gaussian transient force applied at a depth of 3 m. 50

27 The amplitude of the vertical displacement in the $\omega - p$ domain for a vertical Dirac impulse applied at a depth of 9 m. 50

28 The seismogram of the vertical displacements for points on a line y=0 at the free surface for the Gaussian transient force applied at a depth of 9 m. 50

29 The time to the arrival at the free surface of a refracted P-wave created at t=0 s at the point (-2.5,0,-8.25). 51

30 Two refracted P-waves created by a source at the point (-2.5,0,-8.25); (the reflected waves and the created SV waves have been omitted). 51

1 The front view of the "Maison du Mexique." 55

2 The plan of the test site. 55

3 The ground floor. 55

4 The side view of the "Maison du Mexique". 55

5 The position of the building with respect to the tunnel. 56

6 The beam-column connection. 56

7 The chosen foundation. 58

8 Model layout and notations. 58

9 The 6 rigid body displacement modes of one rigid foundation plate. 59

10 The 6 modes $\boldsymbol{u}_b(\boldsymbol{\Psi}_m)(\boldsymbol{x})$ corresponding to the 6 rigid body modes of the first foundation plate. The colors are relative to the vertical displacement component. 61

11 A few modes $\boldsymbol{\Phi}_i(\boldsymbol{x})$. 62

12 The amplitude of the vertical displacement component of the field radiated by the tunnel and of the field diffracted by the building at the free surface at 30 Hz. 63

13 The visualisation model. 64

14 The harmonic response at 10 Hz at the timesteps t=0 s, t=$T/8$, t=$T/4$ and t=$3T/8$ with the period T=1/10 s. 65

15 The harmonic response at 20 Hz at the timesteps t=0 s, t=$T/8$, t=$T/4$ and t=$3T/8$ with the period T=1/20 s. 66

16 The harmonic response at 60 Hz at the timesteps t=0 s, t=$T/8$, t=$T/4$ and t=$3T/8$ with the period T=1/60 s. 67

17 The amplitude of the vertical velocities at the middle of transverse beams and plates at the first and the sixth floor, as well as the amplitude of the vertical velocity component of the field radiated by the tunnel. 69

18 The amplitude of the vertical accelerations at the middle of transverse beams and plates at the first and the sixth floor, as well as the amplitude of the vertical acceleration component of the field radiated by the tunnel. 69

19 A comparison of the predicted vertical acceleration amplitudes with the measured acceleration amplitudes divided by the measured force in point F501z event m06-1. 70

1 The position of the building with respect to the tunnel. Used axes in the computation. 79

List of Tables

3.1 A comparison of the three MISS releases. On Bacchus, the same experiment has been repeated two times and three times, for the first and the second optimisation stage, respectively. 25

4.1 The soil stratigraphy. 29

4.2 The eigenfrequencies of the generic tunnel cell. 31

6.1 Column and beam dimensions at all floors. 56

Chapter 1

Introduction

Vibrations induced by underground railway traffic are a major environmental concern in urban areas. Those vibrations, propagating from a tunnel to nearby buildings, are a possible cause of structural damage, but reradiated noise is the major source of complaints.

In order to reduce the disturbance, many solutions have been proposed in the past, both on the source and on the receiver side, based on empirical design laws and on highly simplified deterministic modelling. Many of these solutions, however, did not lead to satisfactory results.

As far as deterministic modelling is concerned, two-dimensional approaches have been considered, assuming a translation invariant tunnel cross section. Analytical solutions have been used, modelling the soil as a homogeneous full space. Methods based on a finite element model for the tunnel section have also been proposed, coupled either to a finite element model either to a boundary element model for the infinite soil domain. The FEM-FEM option, meshing only a finite part of the soil domain, introduces absorbing boundaries to avoid that waves, propagating away from the tunnel, reflect on the boundary of the mesh. The FEM-BEM option has the advantage that the radiation conditions are automatically taken into account.

The waves propagating away from the tunnel introduce damping in the tunnel-soil-system. Two-dimensional models have the disadvantage that they underestimate this radiation damping. Furthermore, the wave propagation in the direction of the tunnel axis is not taken into account in these models.

In a European context, the Convurt project, "The CONtrol of Vibrations from Underground Railway Traffic", with among its partners universities, metro operators and engineering companies proposes a validated three-dimensional, numerical prediction model.

The key component of the model is a three dimensional tunnel-soil interaction model. The case of an infinite, periodic tunnel in a horizontally layered soil medium is considered. A Floquet transform is used to reduce the problem to a single generic cell. A FEM-BEM coupling is elaborated to describe the dynamical behaviour of this single generic cell, fully taking the dynamical tunnel-soil interaction into account.

Ballast, sleepers and tracks can easily be included in the model. Supposing weakly coupled models, the model can be extended with an excitation model describing the vehicle-track interaction, with a three-dimensional soil-building interaction model, and, finally, with a model describing the reradiated noise.

To validate the numerical prediction model, measurements have been performed at the Cité Universitaire site in Paris. Accelerations have been measured in a tunnel (the RATP RER B line), in the free field (the Cité Universitaire site), and in a nearby building (the "Maison du Mexique", a student dormitory). The vibrations induced by hammer impact on the track, as well as induced by test trains and service trains have been recorded. Similar measurements will be performed at a site in London, in Regent's park, for the Bakerloo and Jubilee lines of London Underground.

Within the frame of the Convurt project, the thesis work can be summarized as follows:

- First, the existing implementation of the periodic boundary element method has to be optimised. A restructuring of the central routine should lead to a far more efficient program, offering moderate computation times even on workstations, no longer limiting the computation to a supercomputer.
- Secondly, an extension of the existing FEM and BEM parts of the Cité Universitaire model with a post-processing module is proposed, leading to an animation of the free field vibration induced by hammer impact on the tunnel invert. A study of the wave propagation both in the direction of the tunnel and in the direction of the tunnel axis becomes possible.
- Finally, a three-dimensional soil-building interaction model has to be constructed from the existing FEM model of the "maison du Mexique." Afterwards, the model should be coupled to the tunnel-soil interaction model, and a post-processing module should again be written to compute a full animation of the vibration at the Cité Universitaire site due to hammer impact. A study of the wave propagation becomes again possible.

The first chapter introduces the theoretical background of the thesis. After a brief introduction of the general soil structure interaction problem, the chapter concentrates on the periodic case. A new way to compute the kinematical basis for the tunnel generic cell is presented, as well as an extensive study on symmetry properties.

Chapter 3 reports on the optimisation work. The restructuring of the central routine is explained and the optimisation is evaluated.

Chapter 4 presents the Cité Universitaire site and its numerical model. It briefly reports on the convergence analysis.

Chapter 5 computes and animates the response to point forces on the tunnel invert. First, the harmonic response is considered and the results are studied using simplified models to explain an identified low frequency resonance, as well as the wave propagation in the direction of the tunnel at high frequencies. Finally, the response on a transient, point force is computed. The wave propagation perpendicular to the tunnel is investigated and is shown to be strongly affected by the presence of the free surface and by the soil layering.

Chapter 6 introduces the "Maison du Mexique" in the model and proposes a method to compute the transmission of the vibrations from the tunnel to the building. The harmonic response of the building is computed due to a point force on the tunnel invert and a first analysis of the results is presented.

Chapters 5 and 6 both conclude summing up the major contributions of this work and discussing future developments and refinements.

Chapter 2

Periodic soil-structure interaction

This chapter presents the numerical modelling of a soil-structure interaction problem, periodic in one direction. The periodic case presented is a particular case of the more general approach of a soil-structure interaction problem, based on the coupling of a boundary element formulation for the soil medium, with a finite element formulation for the structure, as presented already in [8, 7, 12, 17, 20, 10].

The chapter first presents the general approach of a soil-structure interaction problem. A second section then concentrates on the particular periodic case. Finally, a method to compute a kinematical basis for the structure in a periodic case is proposed.

The numerical model is implemented in the MISS program for the BEM part [9], and in the Matlab Toolbox SDT for the FEM part [4].

2.1 The general soil-structure interaction problem

2.1.1 Notations and general equations

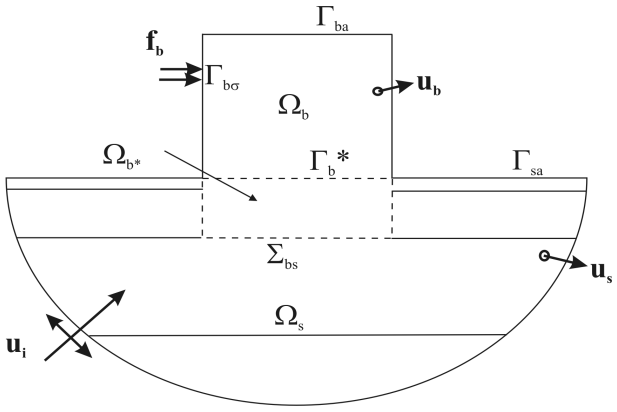

Figure 1: The model layout and notations.

The physical domain is decomposed into two subdomains: the soil denoted by Ω_s and the structure denoted by Ω_b as shown in figure 1. The interface between these domains is denoted by Σ_{bs}. The other boundaries are denoted by Γ_{sa}, Γ_{ba} and $\Gamma_{b\sigma}$, respectively. On Γ_{sa} and Γ_{ba}, free boundary conditions are assumed. On the boundary $\Gamma_{b\sigma}$, a surface force $\boldsymbol{f}_b$ is applied. The displacement fields of the soil and the structure are denoted by $\boldsymbol{u}_s$ and $\boldsymbol{u}_b$, respectively.

The displacement fields on Ω_s and Ω_b due to static loads are supposed to be known. $\boldsymbol{u}_s$ and $\boldsymbol{u}_b$ are assumed to be the dynamic perturbations of these fields due to dynamic loadings.

These dynamic perturbations are assumed to be small enough to allow a linear approximation of the constitutive and equilibrium equations in the vicinity of the static state. Thus, the dynamic perturbations of the stress tensors denoted by $\boldsymbol{\sigma}_s$ and $\boldsymbol{\sigma}_b$ can be expressed as linear functions of the dynamic fluctuation of the stress tensors denoted by $\boldsymbol{\epsilon}_s$ and $\boldsymbol{\epsilon}_b$ using Hooke's law:

$$\sigma_{ij}(\boldsymbol{u}) = \lambda(div\boldsymbol{u})\delta_{ij} + 2\mu\epsilon_{ij}(\boldsymbol{u}) \tag{2.1}$$

$$\epsilon_{ij}(\boldsymbol{u}) = \frac{1}{2}(\partial_i u_j + \partial_j u_i) \tag{2.2}$$

with δ_{ij} the Kronecker symbol ($\delta_{ii} = 1$ and $\delta_{ij} = 0$ with $i \neq j$). λ and μ are the Lamé parameters with a small imaginary part to model hysteretic damping. The traction vectors applying on an interface with an outward normal vector $\boldsymbol{n}$ are denoted by $\boldsymbol{t}_s(\boldsymbol{u}_s)$ and $\boldsymbol{t}_b(\boldsymbol{u}_b)$:

$$\boldsymbol{t}(\boldsymbol{u}) = \boldsymbol{\sigma}(\boldsymbol{u})\boldsymbol{n} \tag{2.3}$$

The displacement field $\boldsymbol{u}_s(\boldsymbol{x}, t)$ of the soil is decomposed in the incident field $\boldsymbol{u}_i(\boldsymbol{x}, t)$ and in the field $\boldsymbol{u}_d(\boldsymbol{x}, t)$ diffracted by the structure.

$$\boldsymbol{u}_s(\boldsymbol{x}, t) = \boldsymbol{u}_i(\boldsymbol{x}, t) + \boldsymbol{u}_d(\boldsymbol{x}, t) \tag{2.4}$$

The incident field is an elastodynamic field defined on $\Omega_s \cup \Omega_{b*}$. Ω_{b*} denotes the excavated part of the soil or the interior domain. Ω_s indicates the soil with excavation or the exterior domain. The diffracted field is defined on Ω_s.

It is assumed that the fields $\boldsymbol{u}_d(\boldsymbol{x}, t)$ and $\boldsymbol{u}_b(\boldsymbol{x}, t)$ satisfy the following causality conditions:

$$\boldsymbol{u}_d(\boldsymbol{x}, t) = 0 \qquad \forall t < 0 \qquad \text{and } \forall \boldsymbol{x} \epsilon \Omega_s \tag{2.5}$$

$$\boldsymbol{u}_b(\boldsymbol{x}, t) = 0 \qquad \forall t < 0 \qquad \text{and } \forall \boldsymbol{x} \epsilon \Omega_b \tag{2.6}$$

The time variable t is transformed to the frequency ω by means of a Fourier transformation. The following convention is used:

$$\hat{f}(\boldsymbol{x}, \omega) = \int_{-\infty}^{\infty} f(\boldsymbol{x}, t) \exp(i\omega t) dt \tag{2.7}$$

$$f(\boldsymbol{x}, t) = \frac{1}{2\pi} \int_{-\infty}^{\infty} \hat{f}(\boldsymbol{x}, \omega) \exp(-i\omega t) d\omega \tag{2.8}$$

where $i = \sqrt{-1}$ is the imaginary unit.

The complete system of Navier equations and boundary conditions in the frequency domain can be written as:

The incident field

$$\boldsymbol{div}\boldsymbol{\sigma}(\boldsymbol{u}_i) = -\omega^2\rho\boldsymbol{u}_i \qquad \text{in } \Omega_s \cup \Omega_{b*} \tag{2.9}$$

$$\boldsymbol{t}_s(\boldsymbol{u}_i) = 0 \qquad \text{on } \Gamma_{sa} \cup \Gamma_{b*} \tag{2.10}$$

The diffracted field

$$\boldsymbol{div}\boldsymbol{\sigma}(\boldsymbol{u}_d) = -\omega^2\rho\boldsymbol{u}_d \qquad \text{in } \Omega_s \tag{2.11}$$

$$\boldsymbol{t}_s(\boldsymbol{u}_d) = 0 \qquad \text{on } \Gamma_{sa} \tag{2.12}$$

The building

$$\boldsymbol{div}\boldsymbol{\sigma}(\boldsymbol{u}_b) = -\omega^2\rho\boldsymbol{u}_b \qquad \text{in } \Omega_b \tag{2.13}$$

$$\boldsymbol{t}_b(\boldsymbol{u}_b) = 0 \qquad \text{on } \Gamma_{ba} \tag{2.14}$$

$$\boldsymbol{t}_b(\boldsymbol{u}_b) = \boldsymbol{f}_b \qquad \text{on } \Gamma_{b\sigma} \tag{2.15}$$

Continuity and equilibrium

$$\boldsymbol{u}_d + \boldsymbol{u}_i = \boldsymbol{u}_b \qquad \text{on } \Sigma_{bs} \tag{2.16}$$

$$\boldsymbol{t}_s(\boldsymbol{u}_d + \boldsymbol{u}_i) + \boldsymbol{t}_b(\boldsymbol{u}_b) = 0 \qquad \text{on } \Sigma_{bs} \tag{2.17}$$

together with radiation conditions for the diffracted field in the soil.

2.1.2 Domain decomposition

The displacements on the interface Σ_{bs} are decomposed on a basis of modes $\boldsymbol{\Psi}_m(\boldsymbol{x})$. In order to verify the continuity equation, these fields are imposed as boundary conditions on both the subdomains Ω_b and Ω_s.

First, the trace on Σ_{bs} of the displacement fields $\boldsymbol{u}_b(\boldsymbol{x},\omega)$ and $\boldsymbol{u}_s(\boldsymbol{x},\omega)$ is written as a linear combination of new displacement fields $\boldsymbol{\Psi}_m(\boldsymbol{x})$.

$$\boldsymbol{u}_b(\boldsymbol{x},\omega)\Big|_{\Sigma_{bs}} = \boldsymbol{u}_s(\boldsymbol{x},\omega)\Big|_{\Sigma_{bs}} = \sum_m c_m(\omega)\boldsymbol{\Psi}_m(\boldsymbol{x}) \tag{2.18}$$

The displacement fields $\boldsymbol{u}_b(\boldsymbol{x},\omega)$ and $\boldsymbol{u}_d(\boldsymbol{x},\omega)$ can then be expanded as:

$$\boldsymbol{u}_d(\boldsymbol{x},\omega) = \sum_m c_m(\omega)\boldsymbol{u}_d(\boldsymbol{\Psi}_m)(\boldsymbol{x},\omega) + \boldsymbol{u}_{d0}(\boldsymbol{x},\omega) \text{ in } \Omega_s \tag{2.19}$$

$$\text{where } \boldsymbol{u}_d(\boldsymbol{\Psi}_m)(\boldsymbol{x})\Big|_{\Sigma_{bs}} = \boldsymbol{\Psi}_m(\boldsymbol{x}); \boldsymbol{u}_i(\boldsymbol{x},\omega) + \boldsymbol{u}_{d0}(\boldsymbol{x},\omega)\Big|_{\Sigma_{bs}} = 0$$

$$\boldsymbol{u}_b(\boldsymbol{x},\omega) = \sum_m c_m(\omega)\boldsymbol{u}_b(\boldsymbol{\Psi}_m)(\boldsymbol{x}) + \sum_i c_i(\omega)\boldsymbol{\Phi}_i(\boldsymbol{x}) \text{ in } \Omega_b \tag{2.20}$$

$$\text{where } \boldsymbol{u}_b(\boldsymbol{\Psi}_m)(\boldsymbol{x})\Big|_{\Sigma_{bs}} = \boldsymbol{\Psi}_m(\boldsymbol{x}); \boldsymbol{\Phi}_i(\boldsymbol{x})\Big|_{\Sigma_{bs}} = 0$$

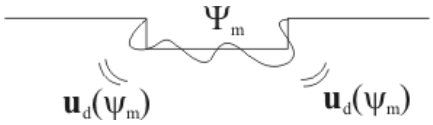

Figure 2: The radiated field.

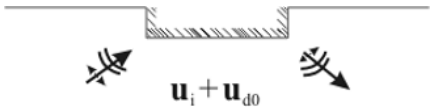

Figure 3: The locally diffracted field.

Figures 2 and 3 show the interpretation of the different fields. The fields $\boldsymbol{u}_d(\boldsymbol{\Psi}_m)(\boldsymbol{x},\omega)$ are the fields radiated in the soil when displacements $\boldsymbol{\Psi}_m(\boldsymbol{x})$ are imposed on the interface Σ_{bs}. Their sum is called the radiated field. The sum of the locally diffracted field $\boldsymbol{u}_{d0}(\boldsymbol{x},\omega)$ and the incident field $\boldsymbol{u}_i(\boldsymbol{x},\omega)$ vanishes on the soil-structure interfacs Σ_{bs}. The sum of the radiated field $\sum_m c_m(\omega)\boldsymbol{u}_d(\boldsymbol{\Psi}_m)(\boldsymbol{x},\omega)$ and the locally diffracted field $\boldsymbol{u}_{d0}(\boldsymbol{x},\omega)$ is called the diffracted field $\boldsymbol{u}_d(\boldsymbol{x},\omega)$. The appropriate radiation conditions have to be imposed on the different fields.

$\boldsymbol{u}_b(\boldsymbol{\Psi}_m)(\boldsymbol{x})$ are the displacement fields in the structure when the displacements $\boldsymbol{\Psi}_m(\boldsymbol{x})$ are imposed on the interface. $\boldsymbol{\Phi}_i(\boldsymbol{x})$ are admissible displacement fields of the structure on a fixed interface.

2.1.3 Variational formulation

The equations (2.13)-(2.17) are written in a weak form using a variational formulation. First, the equilibrium equation of the structure (2.13), verified by a solution $\boldsymbol{u}_b$, is multiplied with a virtual field $\boldsymbol{v}_b$ and integrated over the domain Ω_b:

$$\int_{\Omega_b} \boldsymbol{div}\boldsymbol{\sigma}(\boldsymbol{u}_b)\cdot\boldsymbol{v}_b d\Omega = -\omega^2\int_{\Omega_b}\rho\boldsymbol{u}_b\cdot\boldsymbol{v}_b d\Omega \tag{2.21}$$

Gauss' theorem is applied and yields:

$$\int_{\Omega_b}\boldsymbol{\sigma}(\boldsymbol{u}_b):\boldsymbol{\epsilon}(\boldsymbol{v}_b)d\Omega - \omega^2\int_{\Omega_b}\rho\boldsymbol{u}_b\cdot\boldsymbol{v}_b d\Omega = \int_{\partial\Omega_b}\boldsymbol{t}_b(\boldsymbol{u}_b)\cdot\boldsymbol{v}_b dS \tag{2.22}$$

The fields $\boldsymbol{u}_b$ and $\boldsymbol{v}_b$ both must satisfy the appropriate Dirichlet boundary conditions and the integrals in equation (2.22) must be bounded. The domain decomposition proposed in the previous paragraph is introduced in this equation, expanded with a bounded error on a finite basis:

$$\boldsymbol{u}_b \simeq \sum_m^M c_m\boldsymbol{u}_b(\boldsymbol{\Psi}_m) + \sum_i^I c_i\boldsymbol{\Phi}_i = \boldsymbol{u}_b(\boldsymbol{\Psi})\boldsymbol{c}_M + \boldsymbol{\Phi}\boldsymbol{c}_I \text{ in } \Omega_b \tag{2.23}$$

$$\boldsymbol{u}_s \simeq \sum_m^M c_m\boldsymbol{u}_d(\boldsymbol{\Psi}_m) + \boldsymbol{u}_{d0} + \boldsymbol{u}_i \text{ in } \Omega_s \tag{2.24}$$

The right integral of equation (2.22) is elaborated as follows:

$$\begin{aligned}\int_{\partial\Omega} \boldsymbol{t}_b(\boldsymbol{u}_b)\cdot\boldsymbol{v}_b dS &= \int_{\Sigma_{bs}} \boldsymbol{t}_b(\boldsymbol{u}_b)\cdot\boldsymbol{v}_b dS + \int_{\Gamma_{b\sigma}} \boldsymbol{t}_b(\boldsymbol{u}_b)\cdot\boldsymbol{v}_b dS \\ &= -\int_{\Sigma_{bs}} \boldsymbol{t}_s(\boldsymbol{u}_s)\cdot\boldsymbol{v}_b dS + \int_{\Gamma_{b\sigma}} \boldsymbol{f}_b\cdot\boldsymbol{v}_b dS \text{ (equilibrium (2.17))} \\ &= -\int_{\Sigma_{bs}} \boldsymbol{t}_s(\boldsymbol{u}_i+\boldsymbol{u}_{d0}+\sum_m^M c_m\boldsymbol{u}_d(\boldsymbol{\Psi}_m))\cdot\boldsymbol{v}_b dS + \int_{\Gamma_{b\sigma}} \boldsymbol{f}_b\cdot\boldsymbol{v}_b dS \\ &= -\int_{\Sigma_{bs}} \boldsymbol{t}_s(\boldsymbol{u}_i+\boldsymbol{u}_{d0})\cdot\boldsymbol{v}_b dS - \sum_m^M c_m(\int_{\Sigma_{bs}} \boldsymbol{t}_s(\boldsymbol{u}_d(\boldsymbol{\Psi}_m))\cdot\boldsymbol{v}_b dS) + \int_{\Gamma_{b\sigma}} \boldsymbol{f}_b\cdot\boldsymbol{v}_b dS\end{aligned} \tag{2.25}$$

A standard Galerkin procedure then yields the system of equations describing the soil-structure interaction in the frequency domain,

$$\left[\boldsymbol{K}_s(\omega)-\omega^2\boldsymbol{M}_b+\boldsymbol{K}_b\right]\begin{bmatrix}\boldsymbol{c}_M(\omega)\\ \boldsymbol{c}_I(\omega)\end{bmatrix} = \begin{bmatrix}\boldsymbol{F}_{s1}(\omega)\\ \boldsymbol{F}_{s2}(\omega)\end{bmatrix} + \begin{bmatrix}\boldsymbol{F}_{b1}(\omega)\\ \boldsymbol{F}_{b2}(\omega)\end{bmatrix} \tag{2.26}$$

with:

$$\boldsymbol{K}_b = \begin{bmatrix}\boldsymbol{u}_b(\boldsymbol{\Psi})^\intercal \boldsymbol{K}_b^{FEM}\boldsymbol{u}_b(\boldsymbol{\Psi}) & \boldsymbol{u}_b(\boldsymbol{\Psi})^\intercal \boldsymbol{K}_b^{FEM}\boldsymbol{\Phi}\\ \boldsymbol{\Phi}^\intercal \boldsymbol{K}_b^{FEM}\boldsymbol{u}_b(\boldsymbol{\Psi}) & \boldsymbol{\Phi}^\intercal \boldsymbol{K}_b^{FEM}\boldsymbol{\Phi}\end{bmatrix} \tag{2.27}$$

$$\boldsymbol{M}_b = \begin{bmatrix}\boldsymbol{u}_b(\boldsymbol{\Psi})^\intercal \boldsymbol{M}_b^{FEM}\boldsymbol{u}_b(\boldsymbol{\Psi}) & \boldsymbol{u}_b(\boldsymbol{\Psi})^\intercal \boldsymbol{M}_b^{FEM}\boldsymbol{\Phi}\\ \boldsymbol{\Phi}^\intercal \boldsymbol{M}_b^{FEM}\boldsymbol{u}_b(\boldsymbol{\Psi}) & \boldsymbol{\Phi}^\intercal \boldsymbol{M}_b^{FEM}\boldsymbol{\Phi}\end{bmatrix} \tag{2.28}$$

$$\begin{bmatrix}\boldsymbol{F}_{s1}(\omega)\\ \boldsymbol{F}_{s2}(\omega)\end{bmatrix} = \begin{bmatrix}-\int_{\Sigma_{bs}} \boldsymbol{u}_b(\boldsymbol{\Psi})^\intercal \boldsymbol{t}_s(\boldsymbol{u}_i+\boldsymbol{u}_{d0})(\omega)dS\\ -\int_{\Sigma_{bs}} \boldsymbol{\Phi}^\intercal \boldsymbol{t}_s(\boldsymbol{u}_i+\boldsymbol{u}_{d0})(\omega)dS\end{bmatrix} = \begin{bmatrix}-\int_{\Sigma_{bs}} \boldsymbol{u}_d(\boldsymbol{\Psi})^\intercal \boldsymbol{t}_s(\boldsymbol{u}_i+\boldsymbol{u}_{d0})(\omega)dS\\ 0\end{bmatrix} \tag{2.29}$$

$$\boldsymbol{K}_s(\omega) = \begin{bmatrix}\int_{\Sigma_{bs}} \boldsymbol{u}_b(\boldsymbol{\Psi})^\intercal \boldsymbol{t}_s(\boldsymbol{u}_d(\boldsymbol{\Psi}))(\omega)dS & 0\\ \int_{\Sigma_{bs}} \boldsymbol{\Phi}^\intercal \boldsymbol{t}_s(\boldsymbol{u}_d(\boldsymbol{\Psi}))(\omega)dS & 0\end{bmatrix} = \begin{bmatrix}\int_{\Sigma_{bs}} \boldsymbol{u}_d(\boldsymbol{\Psi})^\intercal \boldsymbol{t}_s(\boldsymbol{u}_d(\boldsymbol{\Psi}))(\omega)dS & 0\\ 0 & 0\end{bmatrix} \tag{2.30}$$

$$\begin{bmatrix}\boldsymbol{F}_{b1}(\omega)\\ \boldsymbol{F}_{b2}(\omega)\end{bmatrix} = \begin{bmatrix}\int_{\Gamma_{b\sigma}} \boldsymbol{u}_b(\boldsymbol{\Psi})^\intercal \boldsymbol{f}_b(\omega)dS\\ \int_{\Gamma_{b\sigma}} \boldsymbol{\Phi}^\intercal \boldsymbol{f}_b(\omega)dS\end{bmatrix} \tag{2.31}$$

$\boldsymbol{K}_b$ and $\boldsymbol{M}_b$ are the stiffness and the mass matrix of the structure, respectively. They are computed using finite elements. $\boldsymbol{F}_{s1}(\omega)$ is the force induced by the incident field on the structure. $\boldsymbol{F}_{b1}(\omega)$ and $\boldsymbol{F}_{b2}(\omega)$ are the equivalent forces applied on the structure due to exterior forces $\boldsymbol{f}_b$.

Hysteretic damping is introduced in the system (2.26),

$$\left[\boldsymbol{K}_s(\omega)+\boldsymbol{Z}_b(\omega)\right]\begin{bmatrix}\boldsymbol{c}_M(\omega)\\ \boldsymbol{c}_I(\omega)\end{bmatrix} = \begin{bmatrix}\boldsymbol{F}_{s1}(\omega)\\ 0\end{bmatrix} + \begin{bmatrix}\boldsymbol{F}_{b1}(\omega)\\ \boldsymbol{F}_{b2}(\omega)\end{bmatrix} \tag{2.32}$$

with $\boldsymbol{Z}_b(\omega)$ the generalized impedance matrix of the structure:

$$\boldsymbol{Z}_b(\omega) = (1-2i\beta)\boldsymbol{K}_b - \omega^2\boldsymbol{M}_b \tag{2.33}$$

2.1.4 The boundary element method

A direct boundary element method is used to approximate the factors $\boldsymbol{t}_s(\boldsymbol{u}_d(\boldsymbol{\Psi}))(\omega)$ and $\boldsymbol{t}_s(\boldsymbol{u}_i + \boldsymbol{u}_{d0})(\omega)$ in the expressions for $\boldsymbol{K}_s(\omega)$ and $\boldsymbol{F}_{s1}(\omega)$ respectively. The method uses direct boundary integral equations and is based on the reciprocity theorem.

Theorem 1 (Reciprocity Theorem) *Let Ω be a bounded or unbounded region; Γ a bounded boundary; $\boldsymbol{u}$ and $\boldsymbol{v}$ elastodynamic displacement fields satisfying the radiation conditions for an unbounded domain Ω. Then:*

$$\int_\Gamma \{\boldsymbol{t}_n(\boldsymbol{u}) \cdot \boldsymbol{v} - \boldsymbol{t}_n(\boldsymbol{v}) \cdot \boldsymbol{u}\} dS = 0$$

The displacement field $\boldsymbol{v}$ is chosen to be the Green's function $\boldsymbol{u}^G(\boldsymbol{x}, \boldsymbol{y}, \boldsymbol{e}_k; \omega)$, corresponding to the displacement at point $\boldsymbol{x}$ generated by a unit point force $\boldsymbol{e}_k$ at point $\boldsymbol{y}$. The representation theorem then takes the following form:

Theorem 2 (Representation Theorem) *Let Ω be a bounded or unbounded region; Γ a bounded and regular boundary; $\boldsymbol{u}$ an elastodynamic displacement field satisfying the radiation conditions for an unbounded domain Ω. Then,*

$$\int_\Gamma \boldsymbol{t}_n(\boldsymbol{u})(\boldsymbol{x}, \omega) \cdot \boldsymbol{u}^G(\boldsymbol{x}, \boldsymbol{\xi}, \boldsymbol{e}_k; \omega) dS - \oint_\Gamma \boldsymbol{t}_n(\boldsymbol{u}^G(\boldsymbol{x}, \boldsymbol{\xi}, \boldsymbol{e}_k; \omega)) \cdot \boldsymbol{u}(\boldsymbol{x}, \omega) dS = \kappa(\boldsymbol{\xi}) \boldsymbol{u}(\boldsymbol{\xi}; \omega) \cdot \boldsymbol{e}_k \quad (2.34)$$

with:

$$\kappa(\boldsymbol{\xi}) = 1 \text{ with } \boldsymbol{\xi} \in \Omega \backslash \Gamma$$
$$\kappa(\boldsymbol{\xi}) = \frac{1}{2} \text{ with } \boldsymbol{\xi} \in \Gamma$$
$$\kappa(\boldsymbol{\xi}) = 0 \text{ with } \boldsymbol{\xi} \notin \Omega$$

The bounded boundary Γ is approximated by N_e boundary elements. The fields $\boldsymbol{u}(\boldsymbol{x}, \omega)$ and $\boldsymbol{t}_n(\boldsymbol{u})(\boldsymbol{x}, \omega)$ are discretized, approximating them with a constant value over each element of the mesh,

$$\boldsymbol{u}(\boldsymbol{x}, \omega) = \sum_{E=1}^{N_e} \sum_{i=1}^{3} u_{Ei}(\omega) \boldsymbol{w}_{Ei}(\boldsymbol{x}) \quad (2.35)$$

$$\boldsymbol{t}_n(\boldsymbol{u}(\boldsymbol{x}, \omega)) = \sum_{E=1}^{N_e} \sum_{i=1}^{3} t_{Ei}(\omega) \boldsymbol{w}_{Ei}(\boldsymbol{x}) \quad (2.36)$$

with $\boldsymbol{w}_{Ei}(\boldsymbol{x})$ defined by

$$\boldsymbol{w}_{Ei}(\boldsymbol{x}) = \boldsymbol{0} \text{ for } \boldsymbol{x} \notin E$$
$$\boldsymbol{w}_{Ei}(\boldsymbol{x}) = \boldsymbol{e}_i \text{ for } \boldsymbol{x} \in E$$

The discretisation is introduced in equation (2.34) and, when $\boldsymbol{\xi}$ is chosen on the boundary Γ:

$$\sum_{E=1}^{N_e}\sum_{i=1}^{3}\left\{t_{Ei}(\omega)\int_E \boldsymbol{w}_{Ei}(\boldsymbol{x})\cdot\boldsymbol{u}^G(\boldsymbol{x},\boldsymbol{\xi},\boldsymbol{a};\boldsymbol{\omega})dS - u_{Ei}(\omega)\oint_E \boldsymbol{t}_{n(E)}(\boldsymbol{u}^G(\boldsymbol{x},\boldsymbol{\xi},\boldsymbol{e}_k;\boldsymbol{\omega}))\cdot\boldsymbol{w}_{Ei}(\boldsymbol{x})dS\right\} = \frac{1}{2}\sum_{E=1}^{N_e}\sum_{i=1}^{3}u_{Ei}(\omega)\boldsymbol{w}_{Ei}(\boldsymbol{\xi})\cdot\boldsymbol{e}_k \tag{2.37}$$

A collocation method is applied writing the equation for the point $\boldsymbol{\xi}$ subsequently in each centre of gravity of the boundary elements, leading to the following system for the $3\times N_e$ traction vector $\boldsymbol{t}(\omega)$,

$$[\boldsymbol{U}^g(\omega)]\boldsymbol{t}(\omega) = [\boldsymbol{T}^g(\omega)]\boldsymbol{u}(\omega) \tag{2.38}$$

with:

$$\boldsymbol{t}(\omega) = (t_{11}(\omega), t_{12}(\omega), ..., t_{Ei}(\omega), ..., t_{N_e3}(\omega))^\intercal \tag{2.39}$$

$$[\boldsymbol{U}^g(\omega)]_{EiFk} = \int_E \boldsymbol{e}_i\cdot\boldsymbol{u}^G(\boldsymbol{x}_E,\boldsymbol{\xi}_F,\boldsymbol{e}_k;\omega)dS(\boldsymbol{x}_E) \tag{2.40}$$

$$[\boldsymbol{T}^g(\omega)]_{EiFk} = \oint_E \boldsymbol{e}_i\cdot\boldsymbol{t}_{n(E)}(\boldsymbol{u}^G(\boldsymbol{x}_E,\boldsymbol{\xi}_F,\boldsymbol{e}_k;\omega))dS(\boldsymbol{x}_E) + \frac{1}{2}\delta_{EF}\delta_{ik} \tag{2.41}$$

$$\tag{2.42}$$

with δ_{ij} the Kronecker symbol: ($\delta_{ii}=1$ and $\delta_{ij}=0$ with $i\neq j$).

Since the Green's function is singular in the point where the force is applied, attention has to be paid to the numerical approximation of the terms of auto-influence or the diagonal terms of $[\boldsymbol{U}^g(\omega)]$ and $[\boldsymbol{T}^g(\omega)]$. Only the Cauchy principle value of the diagonal elements of $[\boldsymbol{T}^g(\omega)]$ exists. It is difficult to approximate these terms using a classical numerical integration scheme. A regularization method is therefore used [8].

The first advantage of using the boundary element method is that only the bounded boundary Γ has to be meshed. Only a small number of degrees of freedom is obtained, compared to a finite element method that meshes (a part of) the soil domain. The second advantage is that the whole soil domain Ω_s is taken into account. The method accounts for the radiation conditions when Ω_s is unbounded. The most important difficulty is the computation of the Green's functions. In this work, the Green's functions of a horizontally layered half space are used. The second difficulty is that the matrices (2.40) and (2.41) are fully populated, complex and non-symmetric, compared to a finite element method that results in banded, symmetrical matrices.

2.1.5 The soil impedance

To compute $\boldsymbol{K}_s(\omega)$, integrals of the following form must be evaluated:

$$[\boldsymbol{K}_s(\omega)]_{mn} = \int_{\Sigma_{bs}} \boldsymbol{u}_d(\boldsymbol{\Psi}_m)^\intercal(\boldsymbol{x},\omega)\boldsymbol{t}_s(\boldsymbol{u}_d(\boldsymbol{\Psi}_n))(\boldsymbol{x},\omega)dS \tag{2.43}$$

The trace of the displacements $\boldsymbol{u}_d(\boldsymbol{\Psi}_m)(\boldsymbol{x},\omega)$ on the interface Σ_{bs} is the displacement field $\boldsymbol{\Psi}_m(\boldsymbol{x})$. The stresses $\boldsymbol{t}_s(\boldsymbol{u}_d(\boldsymbol{\Psi}_n))(\boldsymbol{x},\omega)$ are computed using a direct boundary element method,

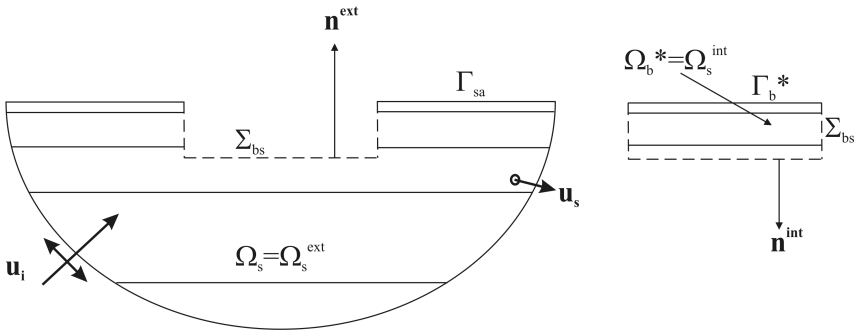

Figure 4: The normal vectors $\boldsymbol{n}^{int}$ and $\boldsymbol{n}^{ext}$.

based on equation (2.34). The bounded boundary Γ of the soil domain Ω_s consists of the soil-structure interface Σ_{bs}, the free soil surface Γ_{sa} and the boundary Γ_∞ for an unbounded domain. The contribution of the boundary Γ_∞ disappears when the radiation conditions are satisfied. The contribution of the boundary Γ_{sa} disappears too when the stresses $\boldsymbol{t}_n(\boldsymbol{u}^G(\boldsymbol{x},\boldsymbol{\xi},\boldsymbol{e}_k;\omega))$ verify the free surface boundary condition on this boundary. The boundary Γ thus can be restricted to only the interface Σ_{bs}. Discretising equation 2.34 using boundary elements allows the computation of $\boldsymbol{t}_s(\boldsymbol{u}_d(\boldsymbol{\Psi}_n))(\boldsymbol{x},\omega)$ in the centres of gravity of the boundary elements. The elements of $\boldsymbol{K}_s(\omega)$ then are computed using a trapezoidal integration scheme.

2.1.6 The forces induced by the incident field

To compute $\boldsymbol{F}_{s1}(\omega)$, integrals of the following form must be evaluated:

$$[\boldsymbol{F}_{s1}(\omega)]_m = -\int_{\Sigma_{bs}} \boldsymbol{u}_d(\boldsymbol{\Psi}_m)^\intercal(\boldsymbol{x},\omega)\boldsymbol{t}_s(\boldsymbol{u}_i+\boldsymbol{u}_{d0})(\boldsymbol{x},\omega)dS \tag{2.44}$$

The trace of the displacements $\boldsymbol{u}_d(\boldsymbol{\Psi}_m)(\boldsymbol{x},\omega)$ on the interface Σ_{bs} is again the displacement field $\boldsymbol{\Psi}_m(\boldsymbol{x})$. The stresses $\boldsymbol{t}_s(\boldsymbol{u}_i+\boldsymbol{u}_{d0})(\boldsymbol{x},\omega)$ are computed using a direct boundary element method formulated for the total field $(\boldsymbol{u}_i+\boldsymbol{u}_{d0})(\boldsymbol{x},\omega)$.

First, the dynamic representation theorem is written for the locally diffracted field on the exterior soil domain. The boundary of the exterior soil domain Γ_1 consists of the soil-structure interface Σ_{bs}, the free soil surface Γ_{sa} and of Γ_∞ for unbounded domains.

$$\int_{\Gamma_1} \boldsymbol{t}_{\boldsymbol{n}^{ext}}(\boldsymbol{u}_{d0})(\boldsymbol{x})\cdot\boldsymbol{u}^G(\boldsymbol{x},\boldsymbol{\xi},\boldsymbol{e}_k)dS - \oint_{\Gamma_1} \boldsymbol{t}_{\boldsymbol{n}^{ext}}(\boldsymbol{u}^G(\boldsymbol{x},\boldsymbol{\xi},\boldsymbol{e}_k))\cdot\boldsymbol{u}_{d0}(\boldsymbol{x})dS = \frac{1}{2}\boldsymbol{u}_{d0}(\boldsymbol{\xi})\cdot\boldsymbol{e}_k \tag{2.45}$$

The contribution of the boundary Γ_∞ disappears when the radiation conditions are satisfied. The contribution of the boundary Γ_{sa} disappears too when the stresses $\boldsymbol{t}_{\boldsymbol{n}^{ext}}(\boldsymbol{u}_{d0})(\boldsymbol{x})$ and $\boldsymbol{t}_{\boldsymbol{n}^{ext}}(\boldsymbol{u}^G(\boldsymbol{x},\boldsymbol{\xi},\boldsymbol{e}_k))$ verify the free surface boundary condition on this boundary.

Then, the dynamic representation theorem is written for the incident field on the interior domain. The boundary of the interior soil domain Γ_2 consists of the soil-structure interface Σ_{bs} and of the free soil surface of the excavated part of the soil Γ_b^*.

$$\int_{\Gamma_2} \boldsymbol{t}_{\boldsymbol{n}^{int}}(\boldsymbol{u}_i)(\boldsymbol{x})\cdot\boldsymbol{u}^G(\boldsymbol{x},\boldsymbol{\xi},\boldsymbol{e}_k)dS - \oint_{\Gamma_2} \boldsymbol{t}_{\boldsymbol{n}^{int}}(\boldsymbol{u}^G(\boldsymbol{x},\boldsymbol{\xi},\boldsymbol{e}_k))\cdot\boldsymbol{u}_i(\boldsymbol{x})dS = \frac{1}{2}\boldsymbol{u}_i(\boldsymbol{\xi})\cdot\boldsymbol{e}_k \tag{2.46}$$

The contribution of the boundary Γ_b^* disappears when the stresses $\boldsymbol{t}_{\boldsymbol{n}^{int}}(\boldsymbol{u}_i)(\boldsymbol{x})$ and $\boldsymbol{t}_{\boldsymbol{n}^{int}}(\boldsymbol{u}^G(\boldsymbol{x},\boldsymbol{\xi},\boldsymbol{e}_k))$ verify the free surface boundary conditions on this boundary.

The boundaries Γ_1 and Γ_2 thus can be restricted to only the soil-structure interface Σ_{bs}.

The difference between the two equations leads to:

$$\begin{aligned}\int_{\Sigma_{bs}} &(\boldsymbol{t}_{\boldsymbol{n}^{ext}}(\boldsymbol{u}_{d0})(\boldsymbol{x}) - \boldsymbol{t}_{\boldsymbol{n}^{int}}(\boldsymbol{u}_i)(\boldsymbol{x})) \cdot \boldsymbol{u}^G(\boldsymbol{x},\boldsymbol{\xi},\boldsymbol{e}_k)dS \\ &- \oint_{\Sigma_{bs}} [\boldsymbol{t}_{\boldsymbol{n}^{ext}}(\boldsymbol{u}^G(\boldsymbol{x},\boldsymbol{\xi},\boldsymbol{e}_k)) \cdot \boldsymbol{u}_{d0}(\boldsymbol{x}) - \boldsymbol{t}_{\boldsymbol{n}^{int}}(\boldsymbol{u}^G(\boldsymbol{x},\boldsymbol{\xi},\boldsymbol{e}_k)) \cdot \boldsymbol{u}_i(\boldsymbol{x})]dS \\ &= \frac{1}{2}(\boldsymbol{u}_{d0}(\boldsymbol{\xi}) - \boldsymbol{u}_i(\boldsymbol{\xi})) \cdot \boldsymbol{e}_k\end{aligned} \tag{2.47}$$

The normals $\boldsymbol{n}^{int}$ and $\boldsymbol{n}^{ext}$ are oppositely pointed:

$$\begin{aligned}\int_{\Sigma_{bs}} &\boldsymbol{t}_{\boldsymbol{n}^{ext}}(\boldsymbol{u}_{d0}(\boldsymbol{x}) + \boldsymbol{u}_i(\boldsymbol{x})) \cdot \boldsymbol{u}^G(\boldsymbol{x},\boldsymbol{\xi},\boldsymbol{e}_k)dS - \oint_{\Sigma_{bs}} \boldsymbol{t}_{\boldsymbol{n}^{ext}}(\boldsymbol{u}^G(\boldsymbol{x},\boldsymbol{\xi},\boldsymbol{e}_k)) \cdot (\boldsymbol{u}_{d0}(\boldsymbol{x}) + \boldsymbol{u}_i(\boldsymbol{x}))dS \\ &= \frac{1}{2}((\boldsymbol{u}_{d0}(\boldsymbol{\xi}) - \boldsymbol{u}_i(\boldsymbol{\xi})) \cdot \boldsymbol{e}_k\end{aligned} \tag{2.48}$$

Given,

$$\boldsymbol{u}_t(\boldsymbol{x}) = \boldsymbol{u}_{d0}(\boldsymbol{x}) + \boldsymbol{u}_i(\boldsymbol{x}) \tag{2.49}$$

$$\boldsymbol{u}_{d0}(\boldsymbol{x}) - \boldsymbol{u}_i(\boldsymbol{x}) = \boldsymbol{u}_t(\boldsymbol{x}) - \boldsymbol{u}_i(\boldsymbol{x}) - \boldsymbol{u}_i(\boldsymbol{x}) = \boldsymbol{u}_t(\boldsymbol{x}) - 2\boldsymbol{u}_i(\boldsymbol{x}) \tag{2.50}$$

then:

$$\begin{aligned}\int_{\Sigma_{bs}} &\boldsymbol{t}_{\boldsymbol{n}^{ext}}(\boldsymbol{u}_t(\boldsymbol{x})) \cdot \boldsymbol{u}^G(\boldsymbol{x},\boldsymbol{\xi},\boldsymbol{e}_k)dS - \oint_{\Sigma_{bs}} \boldsymbol{t}_{\boldsymbol{n}^{ext}}(\boldsymbol{u}^G(\boldsymbol{x},\boldsymbol{\xi},\boldsymbol{e}_k)) \cdot \boldsymbol{u}_t(\boldsymbol{x})dS \\ &= \frac{1}{2}((\boldsymbol{u}_t(\boldsymbol{\xi}) - 2\boldsymbol{u}_i(\boldsymbol{\xi})) \cdot \boldsymbol{e}_k\end{aligned} \tag{2.51}$$

Since $\boldsymbol{u}_t(\boldsymbol{x}) = \boldsymbol{u}_{d0}(\boldsymbol{x}) + \boldsymbol{u}_i(\boldsymbol{x}) = 0$ on Σ_{bs}:

$$\int_{\Sigma_{bs}} \boldsymbol{t}_{\boldsymbol{n}^{ext}}(\boldsymbol{u}_t(\boldsymbol{x})) \cdot \boldsymbol{u}^G(\boldsymbol{x},\boldsymbol{\xi},\boldsymbol{e}_k)dS = -\boldsymbol{u}_i(\boldsymbol{\xi}) \cdot \boldsymbol{e}_k \tag{2.52}$$

Discretising the above equation by means of boundary elements allows the computation of $\boldsymbol{t}_{\boldsymbol{n}^{ext}}(\boldsymbol{u}_t(\boldsymbol{x}))$ in the centres of gravity of the boundary elements for an incident field known in these centres of gravity. The elements of $\boldsymbol{F}_{s1}(\omega)$ then are computed using a trapezoidal integration scheme.

2.2 The periodic soil-structure interaction problem

2.2.1 The Floquet Transformation

The physical model is assumed to be periodic in one direction $\boldsymbol{e}_2$, with a periodicity length L. Following [10, 12, 17], a Floquet transformation is used to restrict the model to a single bounded generic cell. The spatial coordinate along the periodic direction is transformed to the domain of the wavenumber κ.

Definition *(The Floquet Transformation)* Let $f(\boldsymbol{x})$ be a function defined on a periodic domain Ω with values in $\mathbb{C}$, L being the geometrical period in the direction $\boldsymbol{e}_2$. Let $\tilde{\Omega}$ be the generic cell.

$$\tilde{\Omega} = \{\boldsymbol{x} \in \Omega | \frac{-L}{2} \leq \boldsymbol{x} \cdot \boldsymbol{e}_2 \leq \frac{L}{2}\} \tag{2.53}$$

The Floquet transform $\tilde{f}(\tilde{\boldsymbol{x}}, \kappa)$ of the function $f(\boldsymbol{x})$ is complex valued and is a function of the spatial coordinate on the generic cell $\tilde{\boldsymbol{x}}$ and of the wavenumber κ.

$$\tilde{\Omega} \times]\frac{-\pi}{L}, \frac{\pi}{L}[\rightarrow \mathbb{C} : \tilde{f}(\tilde{\boldsymbol{x}}, \kappa) = \sum_{n=-\infty}^{+\infty} f(\tilde{\boldsymbol{x}} + nL\boldsymbol{e}_2) e^{in\kappa L} \tag{2.54}$$

The Floquet inverse transform is defined as:

$$f(\boldsymbol{x}) = \frac{L}{2\pi} \int_{\frac{-\pi}{L}}^{\frac{\pi}{L}} \tilde{f}(\tilde{\boldsymbol{x}}, \kappa) e^{-in\kappa L} d\kappa \qquad \text{with } \boldsymbol{x} = \tilde{\boldsymbol{x}} + nL\boldsymbol{e}_2 \tag{2.55}$$

The transformed function $\tilde{f}(\tilde{\boldsymbol{x}}, \kappa)$ is periodic of the second kind.

Definition *(Periodicity of the second kind)* A complex valued function $\tilde{f}$ defined on a periodic domain Ω is periodic of the second kind with a period L in the direction $\boldsymbol{e}_2$ and wavenumber κ if for all $\boldsymbol{x} \in \Omega$:

$$\tilde{f}(\tilde{x} + L\boldsymbol{e}_2, \kappa) = e^{-i\kappa L} \tilde{f}(\boldsymbol{x}, \kappa) \tag{2.56}$$

Proof

$$\tilde{f}(\tilde{\boldsymbol{x}} + L\boldsymbol{e}_2, \kappa) =^{?} e^{-i\kappa L} \tilde{f}(\tilde{\boldsymbol{x}}, \kappa)$$

$$\Leftrightarrow \frac{L}{2\pi} \int_{\frac{-\pi}{L}}^{\frac{\pi}{L}} \tilde{f}(\tilde{\boldsymbol{x}} + L\boldsymbol{e}_2, \kappa) e^{-in\kappa L} d\kappa =^{?} \frac{L}{2\pi} \int_{\frac{-\pi}{L}}^{\frac{\pi}{L}} e^{-i\kappa L} \tilde{f}(\tilde{\boldsymbol{x}}, \kappa) e^{-in\kappa L} d\kappa$$

$$\Leftrightarrow f(\tilde{\boldsymbol{x}} + L\boldsymbol{e}_2 + nL\boldsymbol{e}_2) =^{!} f(\tilde{\boldsymbol{x}} + (n+1)L\boldsymbol{e}_2)$$

2.2.2 Soil-structure interaction in the frequency-wavenumber domain

The Floquet transformation is used to restrict the soil-structure interaction problem to a single generic cell $\tilde{\Omega}$. The domains Ω_b and Ω_s are restricted to the domains $\tilde{\Omega}_b$ and $\tilde{\Omega}_s$, respectively; the boundaries Γ_{sa}, Γ_{ba}, $\Gamma_{b\sigma}$ and the interface Σ_{bs} being restricted to $\tilde{\Gamma}_{sa}$, $\tilde{\Gamma}_{ba}$, $\tilde{\Gamma}_{b\sigma}$ and the interface $\tilde{\Sigma}_{bs}$. The spatial coordinate along the periodic direction of the structure is transformed to the wavenumber κ. All displacement fields $\boldsymbol{u}(\boldsymbol{x}, \omega)$ and all traction fields $\boldsymbol{t}(\boldsymbol{x}, \omega)$ defined on the periodic domain Ω are transformed to $\tilde{\boldsymbol{u}}(\tilde{\boldsymbol{x}}, \kappa, \omega)$ and $\tilde{\boldsymbol{t}}(\tilde{\boldsymbol{x}}, \kappa, \omega)$ defined on the generic cell $\tilde{\Omega}$.

The operator in the spatial-frequency domain is the total system of governing equations and boundary conditions. This operator is periodic of the first kind.

Definition *(Periodic operator of the first kind)* The operator $\mathcal{A}$ with domain $D(\mathcal{A})$ is periodic of the first kind with periodicity length L in direction $\boldsymbol{e}_2$ if:

$$\forall \boldsymbol{u} \in D(\mathcal{A}), \forall \boldsymbol{x} \in \mathbb{R} : \mathcal{A}(\boldsymbol{x} + L\boldsymbol{e}_2)\boldsymbol{u} = \mathcal{A}(\boldsymbol{x})\boldsymbol{u}$$

The periodicity of the first kind of $\mathcal{A}$ allows a computation in the wavenumber - frequency domain on a single generic cell, with a restriction of the operator domain to fields periodic of the second kind. Afterwards, the Floquet inverse transformation is used to obtain the fields in the spatial-frequency domain [17].

2.2.3 Domain decomposition in the frequency-wavenumber domain

A similar decomposition as in section 2.1 is used.

The displacements on the interface $\tilde{\Sigma}_{bs}$ are decomposed on a basis of modes $\tilde{\boldsymbol{\Psi}}_m(\tilde{\boldsymbol{x}}, \kappa)$. These fields are now complex valued, functions of the wavenumber κ and have to be chosen periodic of the second kind.

$$\tilde{\boldsymbol{u}}_b(\tilde{\boldsymbol{x}}, \kappa, \omega)\Big|_{\tilde{\Sigma}_{bs}} = \tilde{\boldsymbol{u}}_s(\tilde{\boldsymbol{x}}, \kappa, \omega)\Big|_{\tilde{\Sigma}_{bs}} = \sum_m c_m(\kappa, \omega)\tilde{\boldsymbol{\Psi}}_m(\tilde{\boldsymbol{x}}, \kappa) \tag{2.57}$$

The displacement fields $\tilde{\boldsymbol{u}}_b(\tilde{\boldsymbol{x}}, \kappa, \omega)$ and $\tilde{\boldsymbol{u}}_d(\tilde{\boldsymbol{x}}, \kappa, \omega)$ can be expanded as:

$$\tilde{\boldsymbol{u}}_d(\tilde{\boldsymbol{x}}, \kappa, \omega) = \sum_m c_m(\kappa, \omega)\tilde{\boldsymbol{u}}_d(\tilde{\boldsymbol{\Psi}}_m)(\tilde{\boldsymbol{x}}, \kappa, \omega) + \tilde{\boldsymbol{u}}_{d0}(\tilde{\boldsymbol{x}}, \kappa, \omega) \text{ in } \tilde{\Omega}_s \tag{2.58}$$

$$\text{where } \tilde{\boldsymbol{u}}_d(\tilde{\boldsymbol{\Psi}}_m)(\tilde{\boldsymbol{x}}, \kappa)\Big|_{\tilde{\Sigma}_{bs}} = \tilde{\boldsymbol{\Psi}}_m(\tilde{\boldsymbol{x}}, \kappa); \tilde{\boldsymbol{u}}_i(\tilde{\boldsymbol{x}}, \kappa, \omega) + \tilde{\boldsymbol{u}}_{d0}(\tilde{\boldsymbol{x}}, \kappa, \omega)\Big|_{\tilde{\Sigma}_{bs}} = 0$$

$$\tilde{\boldsymbol{u}}_b(\tilde{\boldsymbol{x}}, \kappa, \omega) = \sum_m c_m(\kappa, \omega)\tilde{\boldsymbol{u}}_b(\tilde{\boldsymbol{\Psi}}_m)(\tilde{\boldsymbol{x}}, \kappa) + \sum_i c_i(\kappa, \omega)\tilde{\boldsymbol{\Phi}}_i(\tilde{\boldsymbol{x}}, \kappa) \text{ in } \tilde{\Omega}_b \tag{2.59}$$

$$\text{where } \tilde{\boldsymbol{u}}_b(\tilde{\boldsymbol{\Psi}}_m)(\tilde{\boldsymbol{x}}, \kappa)\Big|_{\tilde{\Sigma}_{bs}} = \tilde{\boldsymbol{\Psi}}_m(\tilde{\boldsymbol{x}}, \kappa); \tilde{\boldsymbol{\Phi}}_i(\tilde{\boldsymbol{x}}, \kappa)\Big|_{\tilde{\Sigma}_{bs}} = 0$$

2.2.4 Variational formulation in the frequency-wavenumber domain

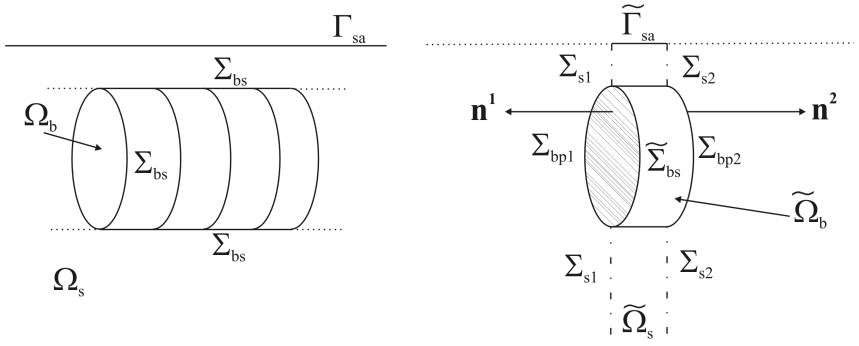

Figure 5: A very long periodic structure and the restriction to a single generic cell, introducing new interfaces.

The equilibrium of the structure is again expressed in a variational form. First, the equilibrium equation of the structure, transformed to the wavenumber domain and verified by a solution $\tilde{\boldsymbol{u}}_b(\kappa)$, is multiplied with a virtual field $\tilde{\boldsymbol{v}}_b(\kappa)$ and integrated over the domain $\tilde{\Omega}_b$.

$$\int_{\tilde{\Omega}_b} div\tilde{\boldsymbol{\sigma}}(\tilde{\boldsymbol{u}}_b(\kappa, \omega)) \cdot \overline{\tilde{\boldsymbol{v}}_b(\kappa)} d\Omega = -\omega^2 \int_{\tilde{\Omega}_b} \rho\tilde{\boldsymbol{u}}_b(\kappa, \omega) \cdot \overline{\tilde{\boldsymbol{v}}_b(\kappa)} d\Omega \tag{2.60}$$

Gauss' theorem is applied and yields:

$$\int_{\tilde{\Omega}_b} \tilde{\boldsymbol{\sigma}}(\tilde{\boldsymbol{u}}_b)(\kappa,\omega) : \overline{\tilde{\boldsymbol{\epsilon}}(\tilde{\boldsymbol{v}}_b(\kappa))} d\Omega - \omega^2 \int_{\tilde{\Omega}_b} \rho \tilde{\boldsymbol{u}}_b(\kappa,\omega) \cdot \overline{\tilde{\boldsymbol{v}}_b(\kappa)} d\Omega = \int_{\partial\tilde{\Omega}_b} \tilde{\boldsymbol{t}}_b(\tilde{\boldsymbol{u}}_b)(\kappa,\omega) \cdot \overline{\tilde{\boldsymbol{v}}_b(\kappa)} dS \quad (2.61)$$

The boundary $\partial\tilde{\Omega}_b$ of the domain $\tilde{\Omega}_b$ now consists of $\tilde{\Gamma}_{ba} \cup \tilde{\Gamma}_{b\sigma} \cup \tilde{\Sigma}_{bs} \cup \Sigma_{bp1} \cup \Sigma_{bp2}$. The presence of new periodic boundaries Σ_{bp1} and Σ_{bp2} is explained in figure 5. For an embedded structure, this figure illustrates the presence of new boundaries Σ_{bp1}, Σ_{bp2}, Σ_{sp1} and Σ_{sp2} due to the restriction of the infinite periodic domain to a single generic cell.

Because of the choice of the complex conjugate in equation (2.60), the integrals over these two periodic boundaries annihilate each other.

Indeed, due to the periodicity properties of the field $\tilde{\boldsymbol{u}}_b$, the stress tensor $\tilde{\boldsymbol{\sigma}}(\tilde{\boldsymbol{u}}_b)$ is periodic of the second kind too:

$$\tilde{\boldsymbol{\sigma}}(\tilde{\boldsymbol{u}}_b)(\tilde{\boldsymbol{x}}_2,\kappa,\omega) = e^{-i\kappa L} \tilde{\boldsymbol{\sigma}}(\tilde{\boldsymbol{u}}_b)(\tilde{\boldsymbol{x}}_1,\kappa,\omega) \text{ with } \tilde{\boldsymbol{x}}_1 \in \Sigma_{bp1} \text{ and } \tilde{\boldsymbol{x}}_2 \in \Sigma_{bp2}. \quad (2.62)$$

Cauchy's principle then yields:

$$\tilde{\boldsymbol{t}}_{\boldsymbol{n}^1}(\tilde{\boldsymbol{u}}_b)(\tilde{\boldsymbol{x}}_1,\kappa,\omega) = \tilde{\boldsymbol{\sigma}}(\tilde{\boldsymbol{u}}_b)(\tilde{\boldsymbol{x}}_1,\kappa,\omega)\boldsymbol{n}^1 \quad (2.63)$$

$$\tilde{\boldsymbol{t}}_{\boldsymbol{n}^2}(\tilde{\boldsymbol{u}}_b)(\tilde{\boldsymbol{x}}_2,\kappa,\omega) = \tilde{\boldsymbol{\sigma}}(\tilde{\boldsymbol{u}}_b)(\tilde{\boldsymbol{x}}_2,\kappa,\omega)\boldsymbol{n}^2 \quad (2.64)$$

The normal vectors $\boldsymbol{n}^1$ and $\boldsymbol{n}^2$, as defined in figure 5, are oppositely pointed:

$$\begin{aligned}
\tilde{\boldsymbol{t}}_{\boldsymbol{n}^2}(\tilde{\boldsymbol{u}}_b)(\tilde{\boldsymbol{x}}_2,\kappa,\omega) &= \tilde{\boldsymbol{\sigma}}(\tilde{\boldsymbol{u}}_b)(\tilde{\boldsymbol{x}}_2,\kappa,\omega)\boldsymbol{n}^2 && (2.65)\\
&= e^{-i\kappa L} \tilde{\boldsymbol{\sigma}}(\tilde{\boldsymbol{u}}_b)(\tilde{\boldsymbol{x}}_1,\kappa,\omega)\boldsymbol{n}^2 && (2.66)\\
&= -e^{-i\kappa L} \tilde{\boldsymbol{\sigma}}(\tilde{\boldsymbol{u}}_b)(\tilde{\boldsymbol{x}}_1,\kappa,\omega)\boldsymbol{n}^1 && (2.67)\\
&= -e^{-i\kappa L} \tilde{\boldsymbol{t}}_{\boldsymbol{n}^1}(\tilde{\boldsymbol{u}}_b)(\tilde{\boldsymbol{x}}_1,\kappa,\omega) && (2.68)
\end{aligned}$$

The periodic interfaces Σ_{bp1} and Σ_{bp2} thus disappear from the equations:

$$\int_{\Sigma_{bp1}\cup\Sigma_{bp2}} \tilde{\boldsymbol{t}}_b(\tilde{\boldsymbol{u}}_b) \cdot \overline{\tilde{\boldsymbol{v}}_b} dS = \int_{\Sigma_{bp1}} [\tilde{\boldsymbol{t}}_b(\tilde{\boldsymbol{u}}_b) \cdot \overline{\tilde{\boldsymbol{v}}_b} + (-e^{-i\kappa L}) \tilde{\boldsymbol{t}}_b(\tilde{\boldsymbol{u}}_b) \cdot e^{i\kappa L} \overline{\tilde{\boldsymbol{v}}_b}] dS = 0$$

A standard Galerkin procedure then yields the system of equations describing the soil-structure interaction in the wavenumber-frequency domain,

$$\left[\boldsymbol{K}_s(\kappa,\omega) - \omega^2 \boldsymbol{M}_b(\kappa) + \boldsymbol{K}_b(\kappa)\right] \begin{bmatrix} \boldsymbol{c}_M(\kappa,\omega) \\ \boldsymbol{c}_I(\kappa,\omega) \end{bmatrix} = \begin{bmatrix} \boldsymbol{F}_{s1}(\kappa,\omega) \\ \boldsymbol{F}_{s2}(\kappa,\omega) \end{bmatrix} + \begin{bmatrix} \boldsymbol{F}_{b1}(\kappa,\omega) \\ \boldsymbol{F}_{b2}(\kappa,\omega) \end{bmatrix} \quad (2.69)$$

with:

$$\boldsymbol{K}_b(\kappa) = \begin{bmatrix} \overline{\tilde{\boldsymbol{u}}_b(\tilde{\boldsymbol{\Psi}})^\intercal(\kappa)} \boldsymbol{K}_b^{FEM} \tilde{\boldsymbol{u}}_b(\tilde{\boldsymbol{\Psi}})(\kappa) & \overline{\tilde{\boldsymbol{u}}_b(\tilde{\boldsymbol{\Psi}})^\intercal(\kappa)} \boldsymbol{K}_b^{FEM} \tilde{\boldsymbol{\Phi}}(\kappa) \\ \overline{\tilde{\boldsymbol{\Phi}}^\intercal(\kappa)} \boldsymbol{K}_b^{FEM} \tilde{\boldsymbol{u}}_b(\tilde{\boldsymbol{\Psi}})(\kappa) & \overline{\tilde{\boldsymbol{\Phi}}^\intercal(\kappa)} \boldsymbol{K}_b^{FEM} \tilde{\boldsymbol{\Phi}}(\kappa) \end{bmatrix} \quad (2.70)$$

$$\boldsymbol{M}_b(\kappa) = \begin{bmatrix} \overline{\tilde{\boldsymbol{u}}_b(\tilde{\boldsymbol{\Psi}})^\intercal(\kappa)} \boldsymbol{M}_b^{FEM} \tilde{\boldsymbol{u}}_b(\tilde{\boldsymbol{\Psi}})(\kappa) & \overline{\tilde{\boldsymbol{u}}_b(\tilde{\boldsymbol{\Psi}})^\intercal(\kappa)} \boldsymbol{M}_b^{FEM} \tilde{\boldsymbol{\Phi}}(\kappa) \\ \overline{\tilde{\boldsymbol{\Phi}}^\intercal(\kappa)} \boldsymbol{M}_b^{FEM} \tilde{\boldsymbol{u}}_b(\tilde{\boldsymbol{\Psi}})(\kappa) & \overline{\tilde{\boldsymbol{\Phi}}^\intercal(\kappa)} \boldsymbol{M}_b^{FEM} \tilde{\boldsymbol{\Phi}}(\kappa) \end{bmatrix} \quad (2.71)$$

$$\begin{bmatrix} \boldsymbol{F}_{s1}(\kappa,\omega) \\ \boldsymbol{F}_{s2}(\kappa,\omega) \end{bmatrix} = \begin{bmatrix} -\int_{\tilde{\Sigma}_{bs}} \overline{\tilde{\boldsymbol{u}}_b(\tilde{\boldsymbol{\Psi}})^\intercal(\kappa)} \tilde{\boldsymbol{t}}_s(\tilde{\boldsymbol{u}}_i + \tilde{\boldsymbol{u}}_{d0})(\kappa,\omega) dS \\ -\int_{\tilde{\Sigma}_{bs}} \overline{\tilde{\boldsymbol{\Phi}}^\intercal(\kappa)} \tilde{\boldsymbol{t}}_s(\tilde{\boldsymbol{u}}_i + \tilde{\boldsymbol{u}}_{d0})(\kappa,\omega) dS \end{bmatrix} = \begin{bmatrix} -\int_{\tilde{\Sigma}_{bs}} \overline{\tilde{\boldsymbol{u}}_d(\tilde{\boldsymbol{\Psi}})^\intercal(\kappa)} \tilde{\boldsymbol{t}}_s(\tilde{\boldsymbol{u}}_i + \tilde{\boldsymbol{u}}_{d0})(\kappa,\omega) dS \\ 0 \end{bmatrix} \tag{2.72}$$

$$\boldsymbol{K}_s(\kappa,\omega) = \begin{bmatrix} \int_{\tilde{\Sigma}_{bs}} \overline{\tilde{\boldsymbol{u}}_d(\tilde{\boldsymbol{\Psi}})^\intercal(\kappa)} \tilde{\boldsymbol{t}}_s(\tilde{\boldsymbol{u}}_d(\tilde{\boldsymbol{\Psi}}))(\kappa,\omega) dS & 0 \\ \int_{\tilde{\Sigma}_{bs}} \overline{\tilde{\boldsymbol{\Phi}}^\intercal(\kappa)} \tilde{\boldsymbol{t}}_s(\tilde{\boldsymbol{u}}_d(\tilde{\boldsymbol{\Psi}}))(\kappa,\omega) dS & 0 \end{bmatrix} = \begin{bmatrix} \int_{\tilde{\Sigma}_{bs}} \overline{\tilde{\boldsymbol{u}}_d(\tilde{\boldsymbol{\Psi}})^\intercal(\kappa)} \tilde{\boldsymbol{t}}_s(\tilde{\boldsymbol{u}}_d(\tilde{\boldsymbol{\Psi}}))(\kappa,\omega) dS & 0 \\ 0 & 0 \end{bmatrix} \tag{2.73}$$

$$\begin{bmatrix} \boldsymbol{F}_{b1}(\kappa,\omega) \\ \boldsymbol{F}_{b2}(\kappa,\omega) \end{bmatrix} = \begin{bmatrix} \int_{\tilde{\Sigma}_{b\sigma}} \overline{\tilde{\boldsymbol{u}}_b(\tilde{\boldsymbol{\Psi}})^\intercal(\kappa)} \tilde{\boldsymbol{f}}_b(\kappa,\omega) dS \\ \int_{\tilde{\Sigma}_{b\sigma}} \overline{\tilde{\boldsymbol{\Phi}}^\intercal(\kappa)} \tilde{\boldsymbol{f}}_b(\kappa,\omega) dS \end{bmatrix} \tag{2.74}$$

Hysteretic damping is introduced in the system, leading to the generalized impedance of the periodic structure:

$$\boldsymbol{Z}_b(\omega,\kappa) = (1 - 2i\beta)\boldsymbol{K}_b(\kappa) - \omega^2 \boldsymbol{M}_b(\kappa) \tag{2.75}$$

2.2.5 The periodic boundary element method

A direct boundary element method is again used to approximate the stresses $\tilde{\boldsymbol{t}}_s(\tilde{\boldsymbol{u}}_d(\tilde{\boldsymbol{\Psi}}))(\kappa,\omega)$ and $\tilde{\boldsymbol{t}}_s(\tilde{\boldsymbol{u}}_i + \tilde{\boldsymbol{u}}_{d0})(\kappa,\omega)$ in the expressions for $\boldsymbol{K}_s(\kappa,\omega)$ and $\boldsymbol{F}_{s1}(\kappa,\omega)$, respectively. The method uses direct boundary integral equations and is based on the reciprocity theorem as presented in section 2.1.4 .

$$\int_{\tilde{\Gamma}} [\tilde{\boldsymbol{t}}_n(\tilde{\boldsymbol{u}}) \cdot \tilde{\boldsymbol{v}} - \tilde{\boldsymbol{t}}_n(\tilde{\boldsymbol{v}}) \cdot \tilde{\boldsymbol{u}}] dS = 0 \tag{2.76}$$

The same difficulty as in the variational formulation of the problem arises. The boundary of the generic cell $\tilde{\Gamma}$ now consists of $\tilde{\Sigma}_{bs} \cup \Sigma_{sp1} \cup \Sigma_{sp2} \cup \tilde{\Gamma}_\infty \cup \tilde{\Gamma}_{sa}$. The appearance of the two periodic boundaries Σ_{sp1} and Σ_{sp2} can again be understood from figure 5.

A solution cannot consist of using the complex conjugate of the fields $\tilde{\boldsymbol{v}}$ and $\tilde{\boldsymbol{t}}_n(\tilde{\boldsymbol{v}})$ in the reciprocity theorem, since this theorem then does not hold.

The solution developed consists of not choosing the fields $\tilde{\boldsymbol{v}}$ equal to the Green's function (cfr. section 2.1.4), but of constructing Green-Floquet functions.

Definition *(The Green-Floquet function)* Let $\boldsymbol{u}^G(\boldsymbol{x},\boldsymbol{y},\boldsymbol{e}_k;\omega)$ be the Green's function, corresponding to the displacement in the point $\boldsymbol{x}$ generated by a point force $\boldsymbol{e}_k$ at point $\boldsymbol{y}$. The Green-Floquet fundamental solution $\tilde{\boldsymbol{u}}^{GF}(\tilde{\boldsymbol{x}},\tilde{\boldsymbol{y}},\boldsymbol{e}_k;\kappa,\omega)$ is defined as the infinite sum of Green's functions at point $\tilde{\boldsymbol{x}}$ for sources periodically located in space, with a phase shift $i\kappa L$ between two adjacent locations:

$$\tilde{\boldsymbol{u}}^{GF}(\tilde{\boldsymbol{x}},\tilde{\boldsymbol{y}},\boldsymbol{e}_k;\kappa,\omega) = \sum_{n=-\infty}^{n=+\infty} e^{in\kappa L} \boldsymbol{u}^G(\tilde{\boldsymbol{x}},\tilde{\boldsymbol{y}} + nL\boldsymbol{e}_2,\boldsymbol{e}_k;\omega) \tag{2.77}$$

The Green-Floquet fundamental solution is periodic of the second kind with respect to $\tilde{\boldsymbol{x}}$ and $\tilde{\boldsymbol{y}}$ with a period L in the direction $\boldsymbol{e}_2$ and for wavenumbers κ and $-\kappa$ respectively.

$$\tilde{\boldsymbol{u}}^{GF}(\tilde{\boldsymbol{x}},\tilde{\boldsymbol{y}}+L\boldsymbol{e}_2,\boldsymbol{e}_k;\kappa,\omega)=e^{-i\kappa L}\tilde{\boldsymbol{u}}^{GF}(\tilde{\boldsymbol{x}},\tilde{\boldsymbol{y}},\boldsymbol{e}_k;\kappa,\omega)$$
$$\tilde{\boldsymbol{u}}^{GF}(\tilde{\boldsymbol{x}}+L\boldsymbol{e}_2,\tilde{\boldsymbol{y}},\boldsymbol{e}_k;\kappa,\omega)=e^{i\kappa L}\tilde{\boldsymbol{u}}^{GF}(\tilde{\boldsymbol{x}},\tilde{\boldsymbol{y}},\boldsymbol{e}_k;\kappa,\omega)$$

With this Green-Floquet fundamental solution, the following direct boundary integral equation on the generic cell is obtained [17]:

$$\begin{aligned}\int_{\Sigma_{bs}}\tilde{\boldsymbol{t}}_n(\tilde{\boldsymbol{u}})(\tilde{\boldsymbol{x}},\kappa,\omega)\cdot\tilde{\boldsymbol{u}}^{GF}(\tilde{\boldsymbol{x}},\tilde{\boldsymbol{\xi}},\boldsymbol{e}_k;\kappa,\omega)dS\\ -\oint_{\Sigma_{bs}}\tilde{\boldsymbol{t}}_n(\tilde{\boldsymbol{u}}^{GF}(\tilde{\boldsymbol{x}},\tilde{\boldsymbol{\xi}},\boldsymbol{e}_k;\kappa,\omega))\cdot\tilde{\boldsymbol{u}}(\tilde{\boldsymbol{x}},\kappa,\omega)dS=\frac{1}{2}\tilde{\boldsymbol{u}}(\tilde{\boldsymbol{\xi}},\kappa,\omega)\cdot\boldsymbol{e}_k\end{aligned}\tag{2.78}$$

Only the soil-structure interface Σ_{bs} appears in this equation. The contribution of the boundary $\tilde{\Sigma}_\infty$ disappears from the equation when the radiation conditions are satisfied. The contribution of the boundary $\tilde{\Sigma}_{sa}$ disappears too when the stresses $\tilde{\boldsymbol{t}}_n(\tilde{\boldsymbol{u}}^g(\boldsymbol{x},\boldsymbol{\xi},\boldsymbol{e}_k;\omega))$ verify the free surface boundary condition on the boundary Σ_{sa} of the periodic domain Ω_s. The contributions of the two interfaces Σ_{s1} and Σ_{s2} disappear from the equations due to the derived periodicity properties and due to Cauchy's principle.

Equation (2.78) is discretised using boundary elements. Only the interface Σ_{bs} has to be meshed. A collocation method is elaborated and leads to the following system of equations,

$$[\tilde{\boldsymbol{U}}^{GF}(\kappa,\omega)]\tilde{\boldsymbol{t}}(\kappa,\omega)=[\tilde{\boldsymbol{T}}^{GF}(\kappa,\omega)]\tilde{\boldsymbol{u}}(\kappa,\omega)\tag{2.79}$$

with:

$$\tilde{\boldsymbol{t}}(\kappa,\omega)=(\tilde{t}_{11}(\kappa,\omega),\tilde{t}_{12}(\kappa,\omega),...,\tilde{t}_{Ei}(\kappa,\omega),...,\tilde{t}_{N_e3}(\kappa,\omega))^\intercal\tag{2.80}$$
$$[\tilde{\boldsymbol{U}}^{GF}(\kappa,\omega)]_{EiFk}=\int_E\boldsymbol{e}_i\cdot\tilde{\boldsymbol{u}}^{GF}(\tilde{\boldsymbol{x}}_E,\tilde{\boldsymbol{\xi}}_F,\boldsymbol{e}_k;\kappa,\omega)dS(\tilde{\boldsymbol{x}}_E)\tag{2.81}$$
$$[\tilde{\boldsymbol{T}}^{GF}(\kappa,\omega)]_{EiFk}=\oint_E\boldsymbol{e}_i\cdot\tilde{\boldsymbol{t}}_{n(E)}(\tilde{\boldsymbol{u}}^{GF}(\tilde{\boldsymbol{x}}_E,\tilde{\boldsymbol{\xi}}_F,\boldsymbol{e}_k;\kappa,\omega))dS(\tilde{\boldsymbol{x}}_E)+\frac{1}{2}\delta_{EF}\delta_{ik}\tag{2.82}$$
$$\tag{2.83}$$

As far as the numerical implementation is concerned, the Green-Floquet function is approximated by a finite sum in equations (2.81) and (2.82):

$$[\tilde{\boldsymbol{U}}^{GF}(\kappa,\omega)]_{EiFk}=\int_E\boldsymbol{e}_i\cdot\tilde{\boldsymbol{u}}^{GF}(\tilde{\boldsymbol{x}}_E,\tilde{\boldsymbol{\xi}}_F,\boldsymbol{e}_k;\kappa,\omega)dS(\tilde{\boldsymbol{x}}_E)\tag{2.84}$$
$$\simeq\int_E\boldsymbol{e}_i\cdot\sum_{n=-N_c}^{+N_c}e^{in\kappa L}\boldsymbol{u}^G(\tilde{\boldsymbol{x}}_E,\tilde{\boldsymbol{\xi}}_F+nL\boldsymbol{e}_2,\boldsymbol{e}_k;\omega)dS(\tilde{\boldsymbol{x}}_E)\tag{2.85}$$
$$=\sum_{n=-N_c}^{+N_c}e^{in\kappa L}\Big(\int_E\boldsymbol{e}_i\cdot\boldsymbol{u}^G(\tilde{\boldsymbol{x}}_E,\tilde{\boldsymbol{\xi}}_F+nL\boldsymbol{e}_2,\boldsymbol{e}_k;\omega)dS(\tilde{\boldsymbol{x}}_E)\Big)\tag{2.86}$$

The integrals in these equations are numerically approximated using Gauss integration:

$$[\tilde{\boldsymbol{U}}^{GF}(\kappa,\omega)]_{EiFk} \simeq \sum_{n=-N_c}^{+N_c} e^{in\kappa L}\Big(\sum_{q=1}^{N_q} w_{Eq}\boldsymbol{u}^G(\tilde{\boldsymbol{x}}_E,\tilde{\boldsymbol{\xi}}_F+nL\boldsymbol{e}_2,\boldsymbol{e}_k;\omega)\cdot\boldsymbol{e}_i\Big) \tag{2.87}$$

leading to:

$$[\tilde{\boldsymbol{U}}^{GF}(\kappa,\omega)] = \sum_{n=-N_c}^{+N_c} e^{in\kappa L}[\tilde{\boldsymbol{U}}^{G}(\omega)]_n \tag{2.88}$$

with:

$$\Big[[\boldsymbol{U}^G(\omega)]_n\Big]_{EiFk} = \sum_{q=1}^{N_q} w_{Eq}\boldsymbol{u}^G(\tilde{\boldsymbol{x}}_E,\tilde{\boldsymbol{\xi}}_F+nL\boldsymbol{e}_2,\boldsymbol{e}_k;\omega)\cdot\boldsymbol{e}_i \tag{2.89}$$

$[\tilde{\boldsymbol{U}}^{G}(\omega)]_0$ is the 3D BEM term. The matrices $[\tilde{\boldsymbol{U}}^{G}(\omega)]_{n\neq 0}$ are computed translating the sources $\tilde{\boldsymbol{\xi}}_F$ by $nL\boldsymbol{e}_2$. Where n is large enough, the distance between the source $\tilde{\boldsymbol{\xi}}_F+nL\boldsymbol{e}_2$ and the receiver $\tilde{\boldsymbol{x}}_E$ is large too. The Green's function $\boldsymbol{u}^G(\tilde{\boldsymbol{x}}_E,\tilde{\boldsymbol{\xi}}_F+nL\boldsymbol{e}_2,\boldsymbol{e}_k;\omega)$ then has a smooth shape over the element E, requiring few Gauss points in the computation of the sum (2.89).

The major advantage of using the Green-Floquet fundamental solution is that the periodic boundary conditions on the periodic interfaces are implicitly accounted for. These boundaries do not need to be discretized as would have been the case when the standard Green's functions are used. The second advantage, compared to a translation invariant solution, is that the Green-Floquet functions have the same singularities as the original Green's functions and that the same integration techniques can be used.

The method is elaborated in a similar way as in sections 2.1.5 and 2.1.6 to compute $\boldsymbol{K}_s$ and $\boldsymbol{F}_{s1}$.

2.2.6 The kinematic basis for the structure

The kinematic basis for the structure has to be determined in such way that the fields $\tilde{\boldsymbol{\Psi}}_m(\tilde{\boldsymbol{x}},\kappa)$, $\tilde{\boldsymbol{u}}_b(\tilde{\boldsymbol{\Psi}}_m)(\tilde{\boldsymbol{x}},\kappa)$ and $\tilde{\boldsymbol{\Phi}}_i(\tilde{\boldsymbol{x}},\kappa)$ are complex valued and periodic of the second kind. For the field $\tilde{\boldsymbol{\Psi}}_m(\tilde{\boldsymbol{x}},\kappa)$, this condition yields for example,

$$\tilde{\boldsymbol{\Psi}}_m(\tilde{\boldsymbol{x}}+L\boldsymbol{e}_2,\kappa) = e^{-i\kappa L}\tilde{\boldsymbol{\Psi}}_m(\tilde{\boldsymbol{x}},\kappa) \tag{2.90}$$

with L the period in the direction $\boldsymbol{e}_2$ and $\tilde{\boldsymbol{x}}$ belonging to Σ_{bp1}.

Assuming that the modes $\boldsymbol{\varphi}_m(\tilde{\boldsymbol{x}})$ can be build satisfying the boundary conditions in the strictly periodic case ($\kappa=0$),

$$\boldsymbol{\varphi}_m(\tilde{\boldsymbol{x}}+L\boldsymbol{e}_2) = \boldsymbol{\varphi}_m(\tilde{\boldsymbol{x}}), \forall\tilde{\boldsymbol{x}}\in\tilde{\Omega}_b|\tilde{\boldsymbol{x}}\cdot\boldsymbol{e}_2 = -\frac{L}{2} \tag{2.91}$$

the displacement fields $\tilde{\boldsymbol{u}}_b(\tilde{\boldsymbol{\Psi}}_m)(\tilde{\boldsymbol{x}},\kappa)$ for non vanishing wavenumber κ can easily be built as follows:

$$\tilde{\boldsymbol{u}}_b(\tilde{\boldsymbol{\Psi}}_m)(\tilde{\boldsymbol{x}},\kappa) = e^{-i\kappa\boldsymbol{e}_2\cdot\tilde{\boldsymbol{x}}}\boldsymbol{\varphi}_m(\tilde{\boldsymbol{x}}) \tag{2.92}$$

These displacement fields $\tilde{\boldsymbol{u}}_b(\tilde{\boldsymbol{\Psi}}_m)(\tilde{\boldsymbol{x}},\kappa)$ are periodic of the second kind:

$$\begin{aligned}\tilde{\boldsymbol{u}}_b(\tilde{\boldsymbol{\Psi}}_m)(\tilde{\boldsymbol{x}}+L\boldsymbol{e}_2,\kappa) &= e^{-i\kappa\boldsymbol{e}_2\cdot(\tilde{\boldsymbol{x}}+L\boldsymbol{e}_2)}\boldsymbol{\varphi}_m(\tilde{\boldsymbol{x}}+L\boldsymbol{e}_2)\\ &= e^{-i\kappa\boldsymbol{e}_2\cdot\tilde{\boldsymbol{x}}}e^{-i\kappa L}\boldsymbol{\varphi}_m(\tilde{\boldsymbol{x}})\\ &= e^{-i\kappa L}\tilde{\boldsymbol{u}}_b(\tilde{\boldsymbol{\Psi}}_m)(\tilde{\boldsymbol{x}},\kappa)\end{aligned}$$

The fields $\tilde{\boldsymbol{\Psi}}_m(\tilde{\boldsymbol{x}},\kappa)$ are the traces of the corresponding fields $\tilde{\boldsymbol{u}}_b(\tilde{\boldsymbol{\Psi}}_m)(\tilde{\boldsymbol{x}},\kappa)$ on the soil-structure interface Σ_{bs}. A similar method has been developed to determine the fields $\tilde{\boldsymbol{\Phi}}_i(\tilde{\boldsymbol{x}},\kappa)$.

In a finite element context, the term $e^{-i\kappa\boldsymbol{e}_2\cdot\tilde{\boldsymbol{x}}}$ can be interpolated at each node generating a diagonal matrix $\Lambda(\kappa)$. The wavenumber dependant modes then are obtained by multiplying the matrix $\boldsymbol{\varphi}_m(\tilde{\boldsymbol{x}})$,interpolating the strictly periodic modes, with $\Lambda(\kappa)$. The first order series expansion of $\Lambda(\kappa)$ for small wavenumbers shows that the value of the stiffness and the mass matrix of the structure varies quadraticly with respect to the wavenumber κ. This result shows that the structure is stiffer for higher wavenumbers. Moreover, unless hysteretic or viscous damping is introduced in the model, the stiffness matrix and the mass matrix of the structure remain real valued for small wavenumbers.

Not expanding $\Lambda(\kappa)$, it can be shown that the proposed method leads to matrices $\boldsymbol{M}_b(\kappa)$ and $\boldsymbol{K}_b(\kappa)$ that are Hermitian, due to the symmetry of the matrices $\boldsymbol{M}_b^{FEM}$ and $\boldsymbol{K}_b^{FEM}$.

2.2.7 The computation for the negative wavenumbers

The Floquet inverse transformation requires the knowledge of the transformed fields for positive and for negative wavenumbers. This section proposes a method to avoid the computation for negative wavenumbers, based on the symmetry of the problem.

The following notation will be used: let $\boldsymbol{x}(x_1,x_2,x_3)$ be a point of the periodic domain Ω. $\boldsymbol{s}(\boldsymbol{x})(x_1,-x_2,x_3)$ then is the point of Ω, at the symmetrical position of $\boldsymbol{x}$ with respect to the plane $x_2=0$.

The periodic domain Ω is assumed to be symmetrical with respect to the plane $x_2=0$. When the applied forces are symmetrical with respect to the plane $x_2=0$, then displacement fields $\boldsymbol{u}_s(\boldsymbol{x})$ and $\boldsymbol{u}_b(\boldsymbol{x})$ with the following symmetry properties are obtained:

$$\left.\begin{aligned}u_{\alpha1}(\boldsymbol{x}) &= u_{\alpha1}(\boldsymbol{s}(\boldsymbol{x}))\\ u_{\alpha2}(\boldsymbol{x}) &= -u_{\alpha2}(\boldsymbol{s}(\boldsymbol{x}))\\ u_{\alpha3}(\boldsymbol{x}) &= u_{\alpha3}(\boldsymbol{s}(\boldsymbol{x}))\end{aligned}\right\} \qquad \boldsymbol{u}_\alpha(\boldsymbol{x}) = \boldsymbol{s}(\boldsymbol{u}_\alpha(\boldsymbol{s}(\boldsymbol{x}))), \forall \boldsymbol{x}\in\Omega, \alpha = b,s$$

The following property can be derived for the Floquet transform of the symmetrical components of the displacement fields:

Lemma 3 (The Floquet transformation of a symmetrical function) *Let $u(\boldsymbol{x})$ be a function symmetrical with respect to the plane $x_2=0$,*

$$u(\boldsymbol{x}) = u(\boldsymbol{s}(\boldsymbol{x})), \forall \boldsymbol{x}\in\Omega$$

then:

$$\begin{aligned}\tilde{u}(\tilde{\boldsymbol{x}},-\kappa) &= \sum_n e^{-in\kappa L} u(\tilde{\boldsymbol{x}} + nL\boldsymbol{e}_2) \\ &= \sum_{n'} e^{+in'\kappa L} u(\boldsymbol{s}(\tilde{\boldsymbol{x}}) + n'L\boldsymbol{e}_2) \\ \tilde{u}(\tilde{\boldsymbol{x}},-\kappa) &= \tilde{u}(\boldsymbol{s}(\tilde{\boldsymbol{x}}),\kappa), \forall \tilde{\boldsymbol{x}} \in \tilde{\Omega}\end{aligned}$$

The following property can be derived for the Floquet transform of the antisymmetrical component of the displacement fields:

Lemma 4 (The Floquet transformation of an antisymmetrical function) *Let $u(\boldsymbol{x})$ be a function antisymmetrical with respect to the plane $x_2 = 0$,*

$$u(\boldsymbol{x}) = -u(\boldsymbol{s}(\boldsymbol{x})), \forall \boldsymbol{x} \in \Omega$$

then:

$$\begin{aligned}\tilde{u}(\tilde{\boldsymbol{x}},-\kappa) &= \sum_n e^{-in\kappa L} u(\tilde{\boldsymbol{x}} + nL\boldsymbol{e}_2) \\ &= \sum_{n'} e^{+in'\kappa L} (-u(\boldsymbol{s}(\tilde{\boldsymbol{x}}) + n'L\boldsymbol{e}_2)) \\ \tilde{u}(\tilde{\boldsymbol{x}},-\kappa) &= -\tilde{u}(\boldsymbol{s}(\tilde{\boldsymbol{x}}),\kappa), \forall \tilde{\boldsymbol{x}} \in \tilde{\Omega}\end{aligned}$$

The transformed fields $\tilde{\boldsymbol{u}}_s(\tilde{\boldsymbol{x}},\kappa)$ and $\tilde{\boldsymbol{u}}_b(\tilde{\boldsymbol{x}},\kappa)$ thus have the following properties:

$$\left.\begin{aligned}\tilde{u}_{\alpha 1}(\tilde{\boldsymbol{x}},-\kappa) &= \tilde{u}_{\alpha 1}(\boldsymbol{s}(\tilde{\boldsymbol{x}}),\kappa) \\ \tilde{u}_{\alpha 2}(\tilde{\boldsymbol{x}},-\kappa) &= -\tilde{u}_{\alpha 2}(\boldsymbol{s}(\tilde{\boldsymbol{x}}),\kappa) \\ \tilde{u}_{\alpha 3}(\tilde{\boldsymbol{x}},-\kappa) &= \tilde{u}_{\alpha 3}(\boldsymbol{s}(\tilde{\boldsymbol{x}}),\kappa)\end{aligned}\right\} \qquad \tilde{\boldsymbol{u}}_\alpha(\tilde{\boldsymbol{x}},-\kappa) = \boldsymbol{s}(\tilde{\boldsymbol{u}}_\alpha(\boldsymbol{s}(\tilde{\boldsymbol{x}}),\kappa)), \forall \tilde{\boldsymbol{x}} \in \tilde{\Omega}, \alpha = b, s \tag{2.93}$$

The generic cell $\tilde{\Omega}$ can be chosen symmetrically with respect to the plane $x_2 = 0$. The value for a negative wavenumber in a point $\tilde{\boldsymbol{x}}$ can then be computed from the value for the corresponding positive wavenumber in the corresponding point $\boldsymbol{s}(\tilde{\boldsymbol{x}})$.

The method holds for a structure, a soil, forces and a generic cell, all symmetrical with respect to the plane $x_2 = 0$. The method can be similarly written for antisymmetrical forces. The method thus holds for an arbitrary combination of forces, since every combination of forces can be decomposed in a sum of a symmetrical and of an antisymmetrical part.

2.2.8 The symmetry of the kinematical basis.

In section 2.2.6, the method used to compute the fields $\tilde{\boldsymbol{\Psi}}_m(\tilde{\boldsymbol{x}},\kappa)$, $\tilde{\boldsymbol{u}}_b(\tilde{\boldsymbol{\Psi}}_m)(\tilde{\boldsymbol{x}},\kappa)$ and $\tilde{\boldsymbol{\Phi}}_i(\tilde{\boldsymbol{x}},\kappa)$ has been explained. The fields $\tilde{\boldsymbol{\Psi}}_m(\tilde{\boldsymbol{x}},\kappa)$ and $\tilde{\boldsymbol{u}}_b(\tilde{\boldsymbol{\Psi}}_m)(\tilde{\boldsymbol{x}},\kappa)$ can be shown to have specific symmetrical properties due to the periodicity of the first kind of the fields $\boldsymbol{\varphi}_m(\tilde{\boldsymbol{x}})$:

$$\forall \tilde{\boldsymbol{x}} \in \tilde{\Omega}_b | \tilde{\boldsymbol{x}} \cdot \boldsymbol{e}_2 = \pm\frac{L}{2} : \tilde{\boldsymbol{u}}_b(\tilde{\boldsymbol{\Psi}}_m)(\tilde{\boldsymbol{x}},-\kappa) = e^{-i(-\kappa)\boldsymbol{e}_2\cdot\tilde{\boldsymbol{x}}}\boldsymbol{\varphi}_m(\tilde{\boldsymbol{x}}) \tag{2.94}$$

$$= e^{-i\kappa\boldsymbol{e}_2\cdot\boldsymbol{s}(\tilde{\boldsymbol{x}})}\boldsymbol{\varphi}_m(\boldsymbol{s}(\tilde{\boldsymbol{x}})) \tag{2.95}$$

$$= \tilde{\boldsymbol{u}}_b(\tilde{\boldsymbol{\Psi}}_m)(\boldsymbol{s}(\tilde{\boldsymbol{x}}),\kappa) \tag{2.96}$$

This last symmetry property is introduced in the symmetrical properties of the transformed fields $\tilde{\boldsymbol{u}}_b(\tilde{\boldsymbol{x}},\kappa)$ for symmetrical fields $\boldsymbol{u}_b(\boldsymbol{x})$ (2.93).

For the x_1-x_3-components of the displacements:

$\forall \tilde{\boldsymbol{x}} \in \tilde{\Omega}_b | \tilde{\boldsymbol{x}} \cdot \boldsymbol{e}_2 = \pm\frac{L}{2}, \beta = 1,3$:

$$0 = \tilde{u}_{b\beta}(\tilde{\boldsymbol{x}},-\kappa) - \tilde{u}_{b\beta}(\boldsymbol{s}(\tilde{\boldsymbol{x}}),\kappa) \tag{2.97}$$

$$= \sum_m c_m(-\kappa,\omega)\tilde{u}_{b\beta}(\tilde{\boldsymbol{\Psi}}_m)(\tilde{\boldsymbol{x}},-\kappa) - \sum_m c_m(\kappa,\omega)\tilde{u}_{b\beta}(\tilde{\boldsymbol{\Psi}}_m)(\boldsymbol{s}(\tilde{\boldsymbol{x}}),\kappa) \tag{2.98}$$

$$= \sum_m (c_m(-\kappa,\omega) - c_m(\kappa,\omega))\tilde{u}_{b\beta}(\tilde{\boldsymbol{\Psi}}_m)(\tilde{\boldsymbol{x}},-\kappa) \tag{2.99}$$

In order for the x_1-x_3-components of arbitrary displacement fields $\tilde{\boldsymbol{u}}_b(\tilde{\boldsymbol{\Psi}}_m)(\tilde{\boldsymbol{x}},\kappa)$ to satisfy equation (2.99), the only solution is that:

$$c_m(-\kappa,\omega) - c_m(\kappa,\omega) = 0 \Leftrightarrow c_m(-\kappa,\omega) = c_m(\kappa,\omega) \tag{2.100}$$

For the x_2-components of the displacements:

$\forall \tilde{\boldsymbol{x}} \in \tilde{\Omega}_b | \tilde{\boldsymbol{x}} \cdot \boldsymbol{e}_2 = \pm\frac{L}{2}$:

$$0 = \tilde{u}_{b2}(\tilde{\boldsymbol{x}},-\kappa) + \tilde{u}_{b2}(\boldsymbol{s}(\tilde{\boldsymbol{x}}),\kappa) \tag{2.101}$$

$$= \sum_m c_m(-\kappa,\omega)\tilde{u}_{b2}(\tilde{\boldsymbol{\Psi}}_m)(\tilde{\boldsymbol{x}},-\kappa) + \sum_m c_m(\kappa,\omega)\tilde{u}_{b2}(\tilde{\boldsymbol{\Psi}}_m)(\boldsymbol{s}(\tilde{\boldsymbol{x}}),\kappa) \tag{2.102}$$

$$= \sum_m (c_m(-\kappa,\omega) + c_m(\kappa,\omega))\tilde{u}_{b2}(\tilde{\boldsymbol{\Psi}}_m)(\tilde{\boldsymbol{x}},-\kappa) \tag{2.103}$$

In order for the x_2-components of arbitrary displacement fields $\tilde{\boldsymbol{u}}_b(\tilde{\boldsymbol{\Psi}}_m)(\tilde{\boldsymbol{x}},\kappa)$ to satisfy equation (2.103), the only solution is that:

$$c_m(-\kappa,\omega) + c_m(\kappa,\omega) = 0 \Leftrightarrow c_m(-\kappa,\omega) = -c_m(\kappa,\omega) \tag{2.104}$$

The conclusion from equations (2.100) and (2.104) is that the only way not to have all zero participation factors when the forces are applied symmetrically, is to have fields $\tilde{u}_b(\tilde{\boldsymbol{\Psi}}_m)(\tilde{\boldsymbol{x}},\kappa)$ with only displacements in the x_2-direction and fields $\tilde{u}_b(\tilde{\boldsymbol{\Psi}}_m)(\tilde{\boldsymbol{x}},\kappa)$ with displacements only in the x_1- and x_3-direction for points $\tilde{\boldsymbol{x}}$ on the periodic interfaces ($\forall \tilde{\boldsymbol{x}} \in \tilde{\Omega}_b | \tilde{\boldsymbol{x}} \cdot \boldsymbol{e}_2 = \pm\frac{L}{2}$). A similar reasoning holds for the fields $\tilde{\boldsymbol{\Phi}}_i(\tilde{\boldsymbol{x}},\kappa)$.

The fields $\tilde{\boldsymbol{\Psi}}_m(\tilde{\boldsymbol{x}},\kappa)$, $\tilde{\boldsymbol{u}}_b(\tilde{\boldsymbol{\Psi}}_m)(\tilde{\boldsymbol{x}},\kappa)$ and $\tilde{\boldsymbol{\Phi}}_i(\tilde{\boldsymbol{x}},\kappa)$ thus form an appropriate basis when the x_1-x_3-components are uncoupled form the x_2-component on the periodic interfaces.

The method proposed in section 2.2.6 results automatically in uncoupled fields. Indeed, when the generic cell is symmetric with respect to the plane $x_2 = 0$, then only dynamic eigenmodes $\boldsymbol{\varphi}_m(\tilde{\boldsymbol{x}})$ symmetrical or antisymmetrical with respect to the plane $x_2 = 0$ can be found. Two exceptions are the rigid body rotations around the x_1- and x_3-axes.

Symmetrical eigenmodes	Antisymmetrical eigenmodes
$\varphi_{m,x_1}(\boldsymbol{s}(\tilde{\boldsymbol{x}})) = \varphi_{m,x_1}(\tilde{\boldsymbol{x}})$	$\varphi_{m,x_1}(\boldsymbol{s}(\tilde{\boldsymbol{x}})) = -\varphi_{m,x_1}(\tilde{\boldsymbol{x}})$
$\varphi_{m,x_2}(\boldsymbol{s}(\tilde{\boldsymbol{x}})) = -\varphi_{m,x_2}(\tilde{\boldsymbol{x}})$	$\varphi_{m,x_2}(\boldsymbol{s}(\tilde{\boldsymbol{x}})) = \varphi_{m,x_2}(\tilde{\boldsymbol{x}})$
$\varphi_{m,x_3}(\boldsymbol{s}(\tilde{\boldsymbol{x}})) = \varphi_{m,x_3}(\tilde{\boldsymbol{x}})$	$\varphi_{m,x_3}(\boldsymbol{s}(\tilde{\boldsymbol{x}})) = -\varphi_{m,x_3}(\tilde{\boldsymbol{x}})$

A supplementary condition has been imposed on the eigenmodes $\boldsymbol{\varphi}_m(\tilde{\boldsymbol{x}})$, namely the periodicity of the first kind,

$$\boldsymbol{\varphi}_m(\tilde{\boldsymbol{x}} + L\boldsymbol{e}_2) = \boldsymbol{\varphi}_m(\tilde{\boldsymbol{x}}), \forall \tilde{\boldsymbol{x}} \in \tilde{\Omega}_b | \tilde{\boldsymbol{x}} \cdot \boldsymbol{e}_2 = -\frac{L}{2} \tag{2.105}$$

leading to:

Symmetrical eigenmodes	Antisymmetrical eigenmodes
$\varphi_{m,x_1}(\boldsymbol{s}(\tilde{\boldsymbol{x}})) = \varphi_{m,x_1}(\tilde{\boldsymbol{x}})$	$\varphi_{m,x_1}(\boldsymbol{s}(\tilde{\boldsymbol{x}})) = 0$
$\varphi_{m,x_2}(\boldsymbol{s}(\tilde{\boldsymbol{x}})) = 0$	$\varphi_{m,x_2}(\boldsymbol{s}(\tilde{\boldsymbol{x}})) = \varphi_{m,x_2}(\tilde{\boldsymbol{x}})$
$\varphi_{m,x_3}(\boldsymbol{s}(\tilde{\boldsymbol{x}})) = \varphi_{m,x_3}(\tilde{\boldsymbol{x}})$	$\varphi_{m,x_3}(\boldsymbol{s}(\tilde{\boldsymbol{x}})) = 0$

The rigid body rotations around the x_1- and x_3-axes cannot satisfy the periodicity conditions. Only four rigid body modes are found back satisfying these conditions.

The proposed method results in fields with only x_1-x_3-displacement components and fields with only a x_2-displacement component on the periodic interfaces.

Chapter 3

Optimisation of the periodic BEM implementation

The periodic boundary element method as discussed in chapter 2 is implemented in the program MISS, developed at Ecole Centrale de Paris [8, 9].

This chapter presents an important optimisation realized on the version of MISS used at Ecole Centrale in September 2002. The optimised release has been validated and is now used. The optimisations make part of the standard r6.3 release.

3.1 A description of the old implementation

The periodic BEM formulation has been presented in chapter 2. The elastodynamic representation theorem has been elaborated and a discretisation has lead to a system of equations with the following form:

$$[\tilde{\boldsymbol{U}}^{GF}(\kappa,\omega)]\tilde{\boldsymbol{t}}(\kappa,\omega) = [\tilde{\boldsymbol{T}}^{GF}(\kappa,\omega)]\tilde{\boldsymbol{u}}(\kappa,\omega) \tag{3.1}$$

The Green-Floquet fundamental solution has been approximated by a finite sum and integrals have been numerically approximated using Gauss points, leading to $[\tilde{\boldsymbol{U}}^{GF}(\kappa,\omega)]$:

$$[\tilde{\boldsymbol{U}}^{GF}(\kappa,\omega)] = \sum_{n=-N_c}^{+N_c} e^{in\kappa L}[\tilde{\boldsymbol{U}}^{G}(\omega)]_n \tag{3.2}$$

with:

$$\Big[[\boldsymbol{U}^{G}(\omega)]_n\Big]_{EiFk} = \sum_{q=1}^{N_q} w_{Eq}\boldsymbol{u}^{G}(\tilde{\boldsymbol{x}}_E, \tilde{\boldsymbol{\xi}}_F + nL\boldsymbol{e}_2, \boldsymbol{e}_k;\omega)\cdot\boldsymbol{e}_i \tag{3.3}$$

and a similar expression for $[\tilde{\boldsymbol{T}}^{GF}(\kappa,\omega)]$.

To compute each matrix $[\tilde{\boldsymbol{U}}^{GF}(\kappa,\omega)]$, the MISS program of September 2002 computed the whole sum (3.2) and a similar sum for each matrix $[\tilde{\boldsymbol{T}}^{GF}(\kappa,\omega)]$. For each wave number and for each frequency, all matrices $[\tilde{\boldsymbol{U}}^{G}(\omega)]_n$ and $[\tilde{\boldsymbol{T}}^{G}(\omega)]_n$ were recomputed. For each combination of matrices $[\tilde{\boldsymbol{U}}^{G}(\omega)]_n$ and $[\tilde{\boldsymbol{T}}^{G}(\omega)]_n$, all data regarding the computation of a Green's function were reread from disk.

The parameters NY and NY2. In chapter 2, it has been explained that, in equation (3.3), the distance between the source $\tilde{\boldsymbol{\xi}}_F + nL\boldsymbol{e}_2$ and the receiver $\tilde{\boldsymbol{x}}_E$ is large for large n. The Green's function $\boldsymbol{u}^G(\tilde{\boldsymbol{x}}_E, \tilde{\boldsymbol{\xi}}_F + nL\boldsymbol{e}_2, \boldsymbol{e}_k; \omega)$ then has a smooth shape over the element E requiring few Gauss points in the computation of the sum (3.3). In the MISS implementation, two parameters NY and $NY2$ are therefore introduced and the sum (3.2) is computed as follows,

$$[\tilde{\boldsymbol{U}}^{GF}(\kappa,\omega)] = \sum_{n_2=-(NY_2-1)}^{+(NY_2-1)} \sum_{n_1=-(NY-1)}^{+(NY-1)} e^{in'\kappa L}\Big(\sum_{q=1}^{N_q(n')} w_{Eq}(n')\boldsymbol{u}^G(\tilde{\boldsymbol{x}}_E, \tilde{\boldsymbol{\xi}}_F + n'L\boldsymbol{e}_2, \boldsymbol{e}_k; \omega)\cdot\boldsymbol{e}_i\Big) \tag{3.4}$$

with

$$n' = n_2(2NY-1) + n_1 \tag{3.5}$$

$$N_c = (2NY2-1)(2NY-1) \tag{3.6}$$

For $n_2 \neq 0$, very few Gauss points are used. For $n_2 = 0$, a fine distribution is used. The parameters NY and NY2 have to be chosen in such way that, given the frequency range of interest and the period L, the use of very few Gauss points is accurate enough for sources $\tilde{\boldsymbol{\xi}}_F + n'L\boldsymbol{e}_2$ located at a distance larger than $NYL\boldsymbol{e}_2$ from the generic cell.

The RFIC feature. MISS has a special feature to reduce the effect of spurious frequencies. Spurious frequencies are the resonances of excavated parts of the soil that have their influence on the solution of the boundary element method. The MISS feature is called RFIC and introduces a second set of boundary integral equations. In the implementation, all matrices $[\tilde{\boldsymbol{U}}^G(\omega)]_n$ in sum (3.2) become the sum of two matrices. The feature is theoretically explained in [3] and its effectiveness is shown in [20].

The discretized Green's function. The computation of the Green's function at different positions for forces at different positions is required. The Green's functions of a layered half space are used. They are computed numerically at discretized positions for forces at discretized positions in the layering. The Green's functions are then interpolated on these discretized data.

The computation of the displacements in certain points in the soil domain. To obtain the displacements in certain points in the soil domain, the representation theorem can be used, as implemented in MISS. The implementations to compute the soil stiffness, the forces induced by the incident field and the displacements in these points have a common routine to compute the matrices $[\tilde{\boldsymbol{U}}^{GF}(\kappa,\omega)]$ and $[\tilde{\boldsymbol{T}}^{GF}(\kappa,\omega)]$. Optimisation work on this routine thus optimises the three implementations.

3.2 Profiling of the old implementation

The performance of the periodic BEM implementation in MISS has been analysed on a SGI computer, using the IRIX built-in function Speedshop. A 'Usertime' experiment has been done, counting the time spent in the functions of the examined program itself and in functions that the operating system is performing for the program.

The MISS program has been evaluated computing a problem with a generic cell with 52 boundary elements, with the number of periodic source translations $\tilde{\boldsymbol{\xi}}_F + n'L\boldsymbol{e}_2$ being determined by the two parameters NY=15 and $NY2$=4 and using the RFIC feature requiring the computation of two combinations of matrices $[\tilde{\boldsymbol{U}}^G(\omega)]_n$ and $[\tilde{\boldsymbol{T}}^G(\omega)]_n$ in the sum (3.2) for each n, instead of one combination. MISS computed the soil stiffness matrix and the displacements in 1 point of the soil domain for one wave number and for one frequency. The computer was a SGI Octane with 512 MB Ram and one R10000/44 Mhz CPU. Speedshop listed the following output (shortened):

```
------------------------------------------------------------------------
SpeedShop profile listing generated Wed Oct 23 19:03:04 2002
------------------------------------------------------------------------
Function list, in descending order by exclusive time
------------------------------------------------------------------------
 [index]  excl.secs excl.%   cum.%  incl.secs incl.%    samples  procedure

    [14]    234.810  44.7%   44.7%    234.810  44.7%       7827  _read
    [17]     66.600  12.7%   57.4%    111.540  22.2%       3718  INTRPU
    [20]     66.270  12.6%   70.0%     66.270  12.6%       2209  memcpy
    [24]     27.960   5.3%   75.3%     27.960   5.3%        932  ASCTGV
...
    [15]      0.000   0.0%  100.0%    295.990  43.0%       7533  RESOU
...
    [16]      0.000   0.0%  100.0%    167.070  31.8%       5569  CONTR
    [5]       0.000   0.0%  100.0%    392.220  74.7%      13074  UTGSTR
```

The excl.secs column shows how much time, in seconds, MISS spent in the routine itself. The incl.secs column shows how much time, in seconds, it spent in the function and descendents of the function.

MISS spent 44% of the usertime in the operating system function _read. During this time MISS reads disk data. UTGSTR is the name of the routine that computes $[\tilde{\boldsymbol{U}}^{GF}(\kappa,\omega)]$ and $[\tilde{\boldsymbol{T}}^{GF}(\kappa,\omega)]$. MISS spent 74.7% of the usertime in this routine and in its descendants.

Optimisation should therefor try to reduce significantly the amount of data to be read from disk and optimisation should concentrate on the routine UTGSTR since it is in this routine and descendants that most time is spent.

3.3 Optimisation in two stages

The reason that the old implementation spends so much time in the 'UTGSTR' routine is of course that the whole sum (3.2) is recomputed completely for all matrices $[\tilde{\boldsymbol{U}}^{GF}(\kappa,\omega)]$ and $[\tilde{\boldsymbol{T}}^{GF}(\kappa,\omega)]$, rereading the discretized Green's function for each n' from disk. The computational effort can be reduced significantly, since the computation of the matrices $[\tilde{\boldsymbol{U}}^{GF}(\kappa,\omega)]$ and $[\tilde{\boldsymbol{T}}^{GF}(\kappa,\omega)]$ for all wave numbers κ requires only a single computation of the matrices $[\tilde{\boldsymbol{U}}^G(\omega)]_n$ and $[\tilde{\boldsymbol{T}}^G(\omega)]_n$.

First, the computation of the matrices $[\tilde{\boldsymbol{U}}^G(\omega)]_n$ and $[\tilde{\boldsymbol{T}}^G(\omega)]_n$ has been optimised. The discretized Green's functions necessary for their computation are no longer reread for each source translation n'. The optimized implementation reads the data only twice: once for the source positions $\tilde{\boldsymbol{\xi}}_F + n'L\boldsymbol{e}_2$ with $n_2 = 1$ and once for the source positions $\tilde{\boldsymbol{\xi}}_F + n'L\boldsymbol{e}_2$ with $n_2 \neq 1$.

In a second optimisation stage, the structure of the implementation has been changed. It now computes the matrices $[\tilde{\boldsymbol{U}}^G(\omega)]_n$ and $[\tilde{\boldsymbol{T}}^G(\omega)]_n$ only once per frequency, saves them in memory and rereads them for all matrices $[\tilde{\boldsymbol{U}}^{GF}(\kappa,\omega)]$ and $[\tilde{\boldsymbol{T}}^{GF}(\kappa,\omega)]$ to be computed.

An important consequence of the optimisations is that the optimised release takes a relatively large amount of memory to store all matrices $[\tilde{\boldsymbol{U}}^G(\omega)]_n$ and $[\tilde{\boldsymbol{T}}^G(\omega)]_n$. Given *neltot* the number of boundary elements and *ndim* the number of degrees of freedom, each matrix $[\tilde{\boldsymbol{U}}^G(\omega)]_n$ or $[\tilde{\boldsymbol{T}}^G(\omega)]_n$ takes the following amount of memory:

$$(neltot \times ndim) \times (neltot \times ndim) \times 2 \times 8 \text{ bytes}$$

$neltot \times ndim$ being the dimension of each squared matrix, the factor 2 appearing since for every matrix element a real and an imaginary part has to be stored and 8 bytes being the amount of memory necessary to save a single number in double precision. The total number of matrices to be saved is $2(2NY2-1)(2NY-1)$. Given a typical BEM mesh with 70 elements and 3 degrees of freedom in each centre of gravity of the elements and using a number of periodic sources determined by NY=15 and $NY2$=4, the necessary amount of memory is 270 MByte.

3.4 Optimisation results

The optimisations have been evaluated by comparing the effect on the computation of a typical problem. The test problem had a generic cell with 70 boundary elements and 3 degrees of freedom in each centre of gravity of the elements. The parameters NY and $NY2$ have been chosen 15 and 4 respectively and the RFIC feature has been used to reduce the effect of spurious frequencies. The soil stiffness matrix and the displacement components in one point in the soil domain have been computed for 1 frequency and for 36 wave numbers. The three versions have been tested on Orchis, a SGI Octane using 1 R10000 CPU at 195 Mhz and disposing of 512 MB Ram, and on Bacchus, a SGI Origin 2000 with 64 R10000 CPU's and disposing of 24 GB Ram running the MISS versions on 4 processors.

	Orchis	Bacchus
MISS 09/2002	?	42028s
MISS with disk reading optimisations only	3506s	1128s; 1428s
MISS after both optimisation stages	265s	200s; 210s; 165s

Table 3.1: A comparison of the three MISS releases. On Bacchus, the same experiment has been repeated two times and three times, for the first and the second optimisation stage, respectively.

The computation times are summarized in table 3.1, showing that the computational effort has been reduced by both optimisations on Bacchus with a factor of more than 200.

After the two optimisation stages, MISS computes the matrices $[\tilde{\boldsymbol{U}}^g(\omega)]_n$ and $[\tilde{\boldsymbol{T}}^g(\omega)]_n$ only once per frequency ω. The cost in computation time to sum these matrices to $[\tilde{\boldsymbol{U}}^{GF}(\kappa,\omega)]$ and

$[\tilde{\boldsymbol{T}}^{GF}(\kappa,\omega)]$ for every κ afterwards is very small. Summing the matrices $[\tilde{\boldsymbol{U}}^{g}(\omega)]_n$ and $[\tilde{\boldsymbol{T}}^{g}(\omega)]_n$ to the matrices $[\tilde{\boldsymbol{U}}^{GF}(\kappa,\omega)]$ and $[\tilde{\boldsymbol{T}}^{GF}(\kappa,\omega)]$ isn't faster on 4 Bacchus processors than on 1 Orchis processor. The 4 Bacchus processors are however faster in computing the set of matrices to be summed. This is why the difference in computation time between Orchis and Bacchus becomes so small after the two optimisation stages.

The question mark in the table indicates that the time needed by MISS 09/2002 on Orchis has not been measured. This release would have taken an amount of time significantly larger than the 42028s of Bacchus.

The new optimised version has been used afterwards to create animations. For these purposes, the displacements in the soil domain have to be computed in a large amount of points. For 54 points in the soil domain on the generic cell, a computation time of approximately 12 minutes has been found per frequency.

3.5 Conclusions and perspectives

The periodic method presented in chapter 2 to describe the soil-structure interaction of very long periodic structures is a very powerful method that reduces an enormous problem to a single generic cell.

The time demanding part in the method is the periodic BE-formulation. The implementation has been optimised in two stages. First the disk reading has significantly been reduced, then the computation of the sum has been optimised. The computation times have been reduced with a tremendous factor of more than 200.

Very moderate computation times have been obtained, both on the Bacchus supercomputer and on the Orchis workstation.

Chapter 4

Numerical model of the Cité Universitaire site in Paris

The numerical model presented in the previous chapter has been used to model a dynamic tunnel-soil interaction problem. In particular, a model of the Cité Universitaire site in Paris has been made. Measurements have been performed at the same site and will allow a validation of the model. The numerical model for this site has been developed previously by Prof. T.M. Al-Hussaini [3] and by Dr. Othman. This chapter briefly presents the site and its model and reports on the convergence analysis.

4.1 Introduction

Numerical computations of the ground vibration have been carried out for the Cité Universitaire site in Paris. This site is located on the RATP RER B line, between the metro stations Cité Universitaire and Gentilly. The metro tunnel is a masonry cut-and-cover tunnel at a shallow depth below the ground surface. Two tracks are running in the tunnel.

Figure 1 shows a plan view of the site, with the location of the metro tunnel. Figure 2 shows the metro tunnel at the station Cité Universitaire and figure 3 shows a typical cross section. Figure 4 shows one symmetrical half of the model of this cross section, as well as the modelled soil layering. It shows that the tunnel thickness is 0.6 m on the top and 1.5 m on the two sides. The top of the tunnel is 2.3 m below the ground surface. The masonry is modelled with a Young's modulus of 14 GPa, a Poisson ratio of 0.15, a density of 2400 kg/m^3 and a hysteretic damping ratio of 2%.

The tunnel is considered infinitely long with an invariant cross section. As discussed in chapter 2, the problem can be reduced to a single generic cell, shown in figure 5. The period has been taken equal to L=0.3 m. The tunnel has been modelled using finite elements. Isoparametric 8-node brick elements have been chosen. The element distribution is shown in figure 5.

The ballast, sleepers and track have not yet been modelled. Their influence on the dynamic behaviour is important only above 80 Hz [22].

The soil layering at the site has been determined from a Spectral Analysis of Surfacs Waves (SASW test) [19]. 2 layers are taken into account, on top of a homogeneous half space. 3 different

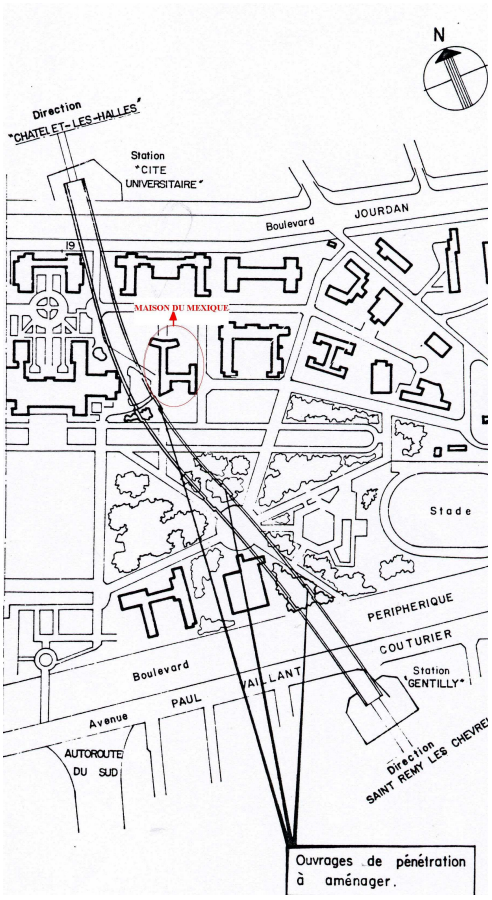

Figure 1: The plan of the test site.

Figure 2: The metro tunnel at the station Cité Universitaire.

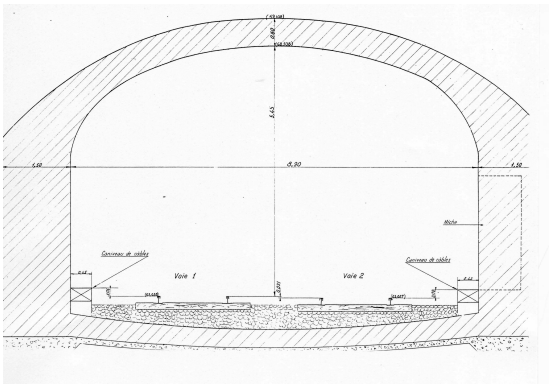

Figure 3: The cross section of the metro tunnel.

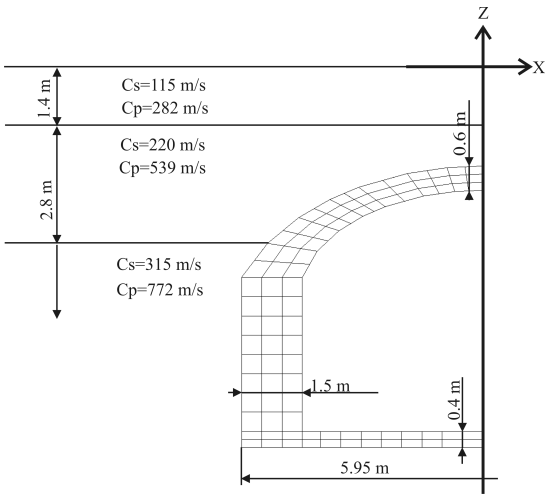

Figure 4: The model of the cross section of the tunnel and soil characteristics.

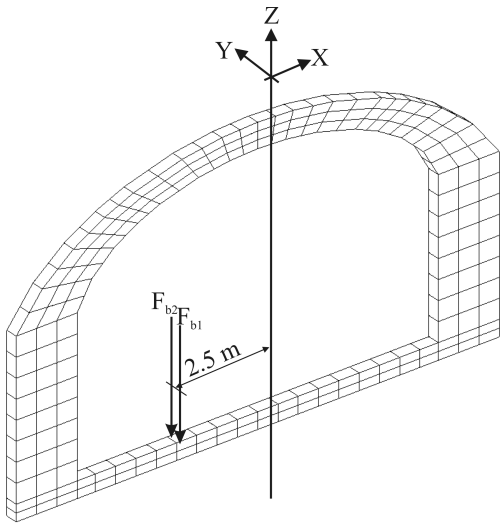

Figure 5: The single generic cell and the position of the applied forces.

materials are distinguished. The layering is summarized in table 4.1. A hysteretic damping ratio of 0.05 is assumed for all 3 materials.

Layer	Thickness [m]	C_s [m/s]	C_p [m/s]	ρ [kg/m^3]
1	1.4	115	282	1700
2	2.8	220	539	1700
3	∞	315	772	1700

Table 4.1: The soil stratigraphy.

4.2 The applied forces

The cases of a non-moving harmonic and of a transient excitation on the tunnel invert are considered. The force has been applied at a position with coordinates (-2.5,0,-8.25) in the frame of reference defined in figure 6.

The applied force is transformed to the wavenumber domain with the Floquet transformation leading to two equivalent forces appied on two nodes of the finite element model of the generic cell (figure 5). Their spectral content in the wavenumber domain is uniform and equal to 1/2.

4.3 The visualization model

To visualise the results, a visualization model will be used in the next chapters, as shown in figure 6. The generic cell is repeated 80 times in the positive y-direction. Three surfaces in the soil are meshed: the free surface S1, two horizontal surfaces S2 at the depth of the tunnel invert and a vertical surface S3 between the free surface and the tunnel top. Their displacements

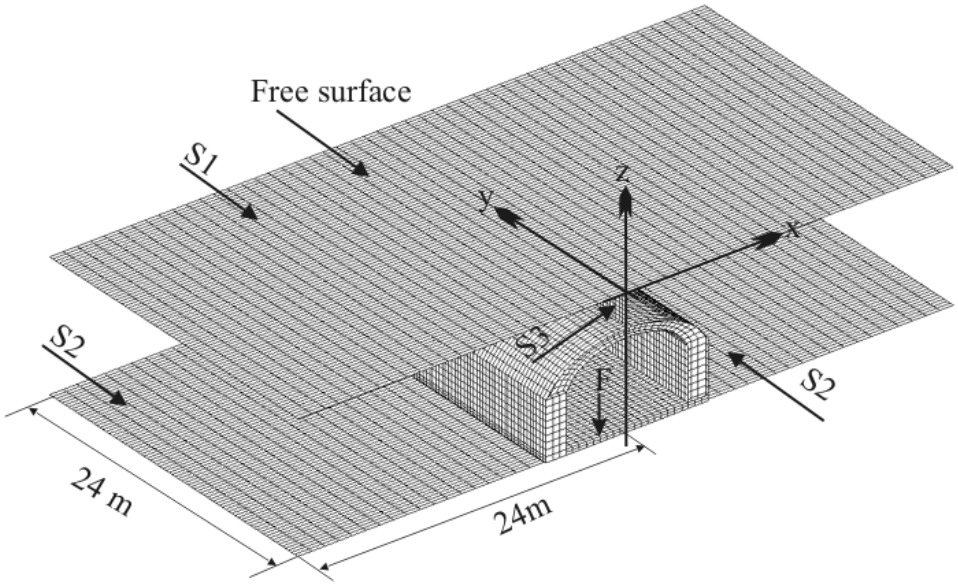

Figure 6: The tunnel, the non-moving force and the free surface.

on the generic cell are computed using the elastodynamic representation theorem. A Floquet inverse transformation leads to the displacements on the repeated cells. Colours are applied to the visualization model, relative to the vertical displacement component. The colours on the three soil surfaces are exagerated ten times versus the colours applied to the tunnel.

4.4 The convergence analysis

4.4.1 The reduced modal basis

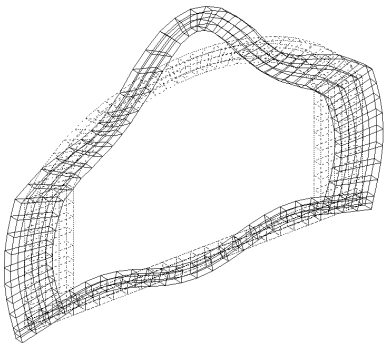

Figure 7: Mode 11 at 57.6 Hz (Only x-z displacements).

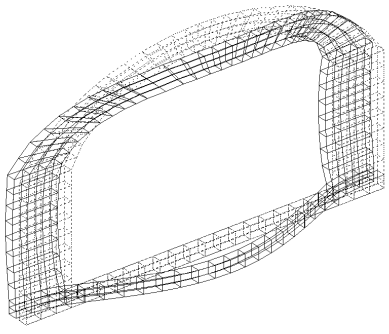

Figure 8: Mode 17 at 101.5 Hz (only y-displacements).

A kinematic basis for the tunnel has to be determined, consisting of modes $\tilde{\boldsymbol{u}}_b(\tilde{\boldsymbol{\Psi}}_m)(\tilde{\boldsymbol{x}},\kappa)$ and $\tilde{\boldsymbol{\Phi}}_i(\tilde{\boldsymbol{x}},\kappa)$. A basis of modes $\tilde{\boldsymbol{u}}_b(\tilde{\boldsymbol{\Psi}}_m)(\tilde{\boldsymbol{x}},\kappa)$ is sufficient. Including ballast, sleepers and rails in the model requires the usage of $\tilde{\boldsymbol{\Phi}}_i(\tilde{\boldsymbol{x}},\kappa)$ modes.

The modes $\tilde{\boldsymbol{u}}_b(\tilde{\boldsymbol{\Psi}}_m)(\tilde{\boldsymbol{x}},\kappa)$ are derived from the dynamic eigenmodes $\boldsymbol{\varphi}_m(\tilde{\boldsymbol{x}})$ of the generic tunnel

cell with free surface boundary conditions on Σ_{bs} and satisfying the supplementary periodicity constraints. Due to these constraints and the symmetry of the cell, displacements in the y-direction are uncoupled from displacements in the x-z-directions on the periodic interfaces. Only 4 rigid body modes $\boldsymbol{\varphi}_m(\tilde{\boldsymbol{x}})$ are found, instead of 6, since the rigid body rotations around x and z axes do not satisfy the periodicity conditions.

The eigenfrequencies of the modes are listed in table 4.2.

Mode	1	2	3	4	5	6	7	8	9	10
Freq. (Hz)	0	0	0	0	9.9	14.0	24.0	36.9	41.9	52.0
Mode	11	12	13	14	15	16	17	18	19	20
Freq. (Hz)	57.6	65.1	74.3	83.4	93.5	94.5	101.5	114.3	125.9	134.3
Mode	21	22	23	24	25	26	27	28	29	30
Freq. (Hz)	146.1	156.8	164.2	164.9	177.9	189.9	194.3	204.8	222.6	224.8

Table 4.2: The eigenfrequencies of the generic tunnel cell.

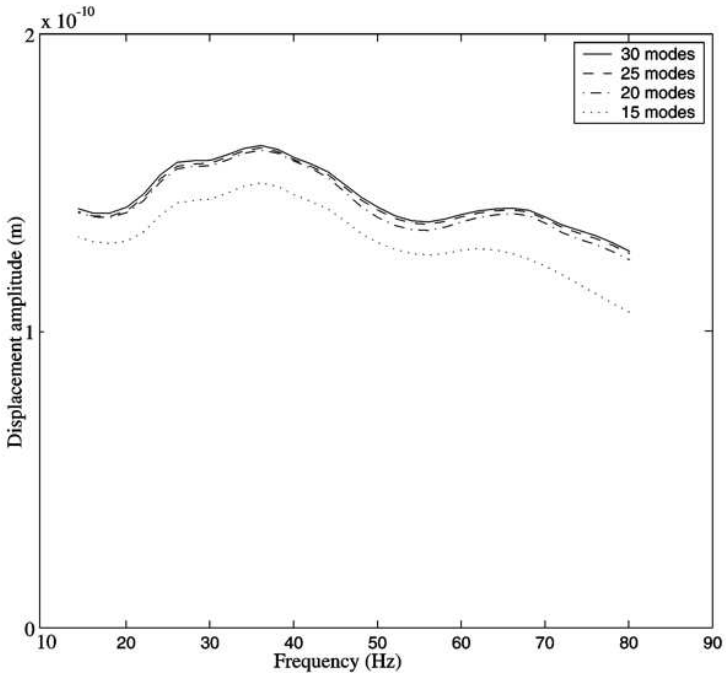

Figure 9: The amplitude of the vertical displacement in the tunnel point under the force, computed with different numbers of modes.

A convergence analysis has been carried out on the number of modes needed for the present study. The displacements in the frequency domain in the tunnel point under the force have been computed with 15, 20, 25 and 30 modes. From figure 9, it has been concluded that 25 modes are necessary for the convergence of the displacement amplitudes for frequencies up to 80 Hz. The frequency of the 25th mode is 177.9 Hz. All further computations have been made using 30 modes. The frequency of the 30th mode is 224.8 Hz. Modes 11 and 17 are shown in figures 7 and 8 respectively.

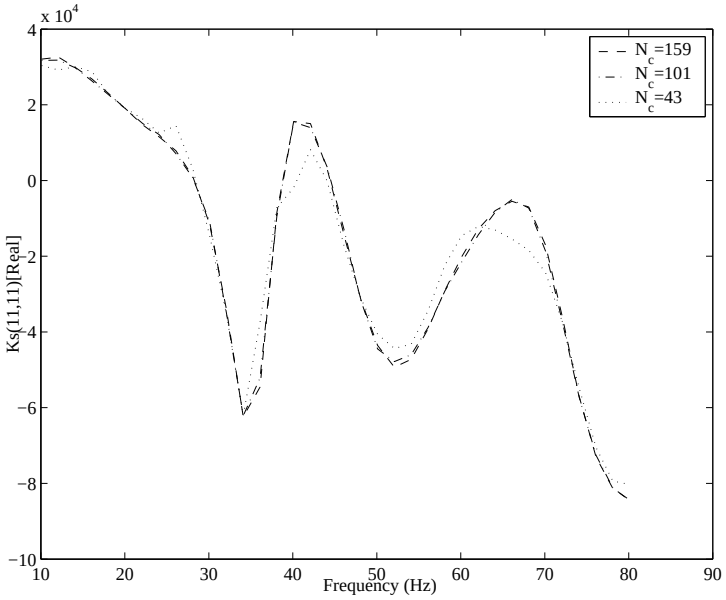

Figure 10: The real part of element (11,11) of the soil impedance matrix for p=0 s/m and for different numbers N_c.

4.4.2 The periodic boundary element method

The soil impedance is computed using a periodic boundary element method. The fundamental solution used is the Green-Floquet function, that is approximated in the implementation by a finite sum, the number of terms taken into account being determined by the parameters NY and $NY2$. Different elements of the soil impedance matrix have been computed in the slowness-frequency domain for different combinations of NY and $NY2$ and a convergence has been found. Figure 10 shows the real part of element (11,11) of the soil impedance in a frequency range from 0.1 Hz to 80.1 Hz and for a slowness p=0 s/m, computed with different numbers of periodic source locations determined by NY=160 and $NY2$=1 (N_c=159), NY=15 and $NY2$=4 (N_c=101) and NY=15 and $NY2$=2 (N_c=43). For the combination $NY2$=15 and NY=4, a convergence is observed and this combination has been used.

4.4.3 The sampling in the wavenumber-frequency domain

According to equation (2.54), a computation in a wavenumber range from $-\pi/L$ to π/L is necessary. For the low frequencies (up to 15 Hz), it has been observed, however, that a range in wavenumbers from -0.6 1/m to 0.6 1/m is sufficient, since, as shown on figure 11, the solution is descending rapidly with κ. A sampling of 0.015 1/m is used. For the higher frequencies (from 15 to 80 Hz), a range in slowness p (with $p = \kappa/\omega$) from -0.004 s/m to 0.004 s/m has appeared to be more suitable as shown on figure 12. A sampling of 0.0001 s/m is used.

Based on the symmetry of the generic cell, a solution has been developed to avoid the computation of the negative wave numbers/slowness. The system of equations (2.69) in chapter 2 is solved for the positive wavenumbers only (or only for the positive slowness). The inverse Floquet transformation (2.54) is computed afterwards accounting for the symmetry. A simple trapezoidal integration scheme is used.

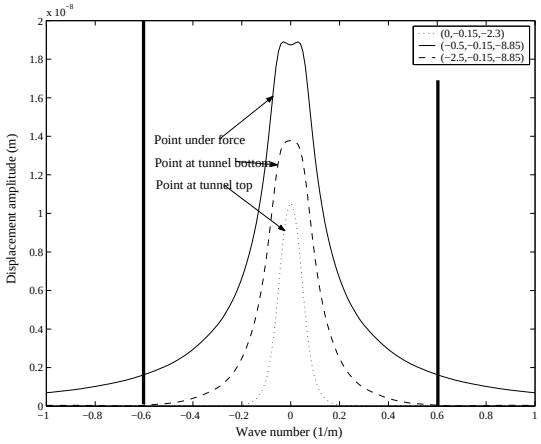

Figure 11: The amplitude of the vertical displacement in the wavenumber domain for f=5 Hz for different tunnel points.

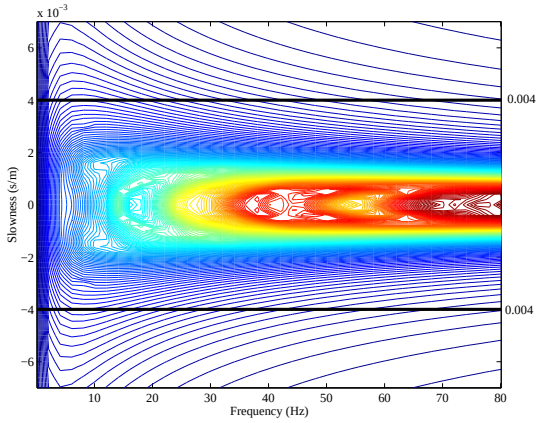

Figure 12: The amplitude of the vertical velocity in the slowness-frequency domain in the tunnel point under the force.

4.5 The generalized impedance of the tunnel and of the soil

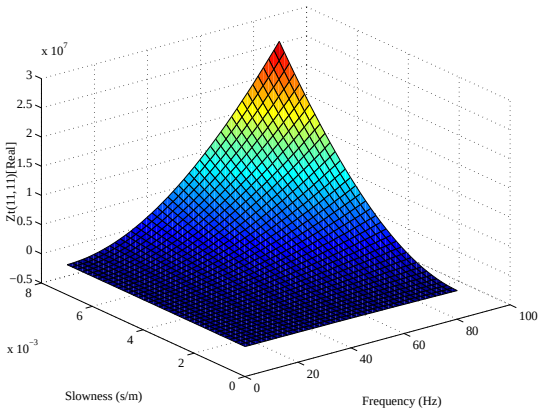

Figure 13: The real part of the element (11,11) of the generalized tunnel impedance matrix.

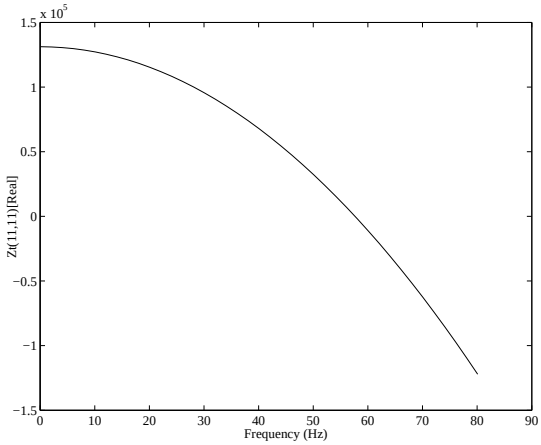

Figure 14: The real part of element (11,11) of the generalized tunnel impedance matrix for slowness p=0 s/m.

Figure 13 shows the real part of the element (11,11) of the generalized tunnel impedance matrix in a slowness range from 0 to 0.007 s/m and in a frequency range from 0.1 to 80.1 Hz. The real part of the impedance increases with the wavenumber approximately as κ^2. Indeed, in chapter 2, it has been found that the tunnel stiffness matrix varies quadratically with respect to the wavenumber κ. Moreover, for small wavenumbers, it has been found that the tunnel stiffness remains real valued, as does the tunnel mass matrix. Introducing hysteretical damping as proposed in chapter 2, proportional to the tunnel stiffness matrix $\boldsymbol{K}_b(\kappa)$, thus leads to an imaginary part of the generalized tunnel impedance, varying quadratically with the wavenumber too. This result shows that, the higher the wavenumber, the stiffer the tunnel and the higher the hysteretic damping. For small values of the slowness p, the inertial term is dominant: the real part of the impedance becomes negative and decreases with the frequency as ω^2 (figure 14).

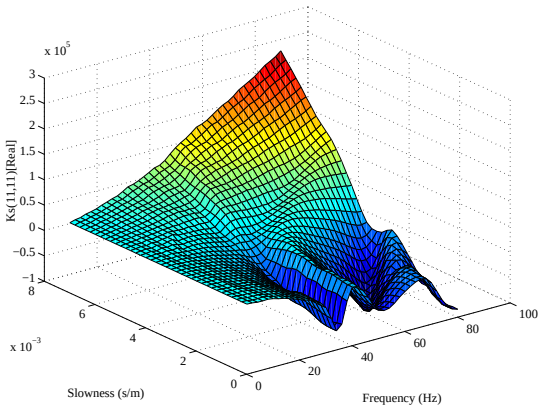

Figure 15: The real part of the element (11,11) of the soil impedance matrix.

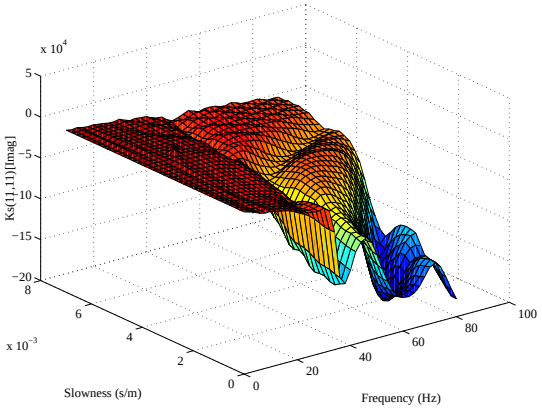

Figure 16: The imaginary part of element (11,11) of the soil impedance matrix.

Figures 15 and 16 show the real and the imaginary part of the element (11,11) of the soil impedance matrix in a slowness range from 0 to 0.007 s/m and in a frequency range from 0.1 to 80.1 Hz.

The shape of the soil impedance is less regular than the shape of the generalized tunnel impedance. As for the tunnel, the soil is stiffer as κ increases. The inertial effect can also be observed for low slowness.

Due to the unboundedness of the soil domain, accounting for the radiation conditions, an important imaginary part is found for the soil impedance, introducing damping in the system. This damping almost disappears at large slowness. Indeed, for larger the slowness, the component of the wave propagation in the direction of the tunnel is more impotant. For larger slowness, less propagation away from the tunnel thus is observed and less energy is radiated away.

Chapter 5

Impulse loads on a tunnel invert: response in the free field

The previous chapter described the modelled site, its numerical approximations and reported on the convergence analysis for the numerical model. This chapter computes the harmonic and transient response for a point force on the tunnel invert. The response in the free field and in tunnel points is animated and based on these animations, the results are investigated.

5.1 The transfer functions in the spatial-frequency domain

To investigate the transfer functions for a force on the tunnel invert, the response of the tunnel has been computed for harmonic loads at different frequencies. The transfer functions for the

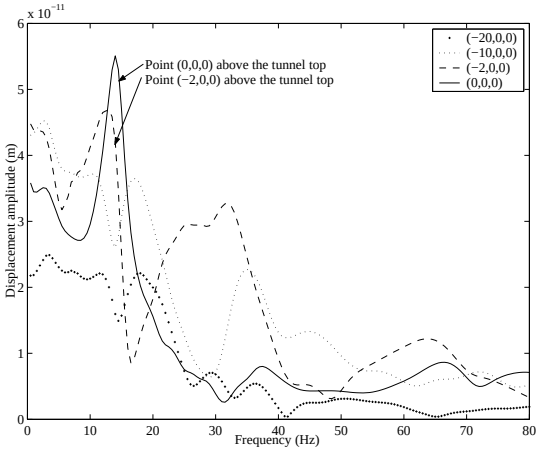

Figure 1: The amplitude of the vertical displacement in points at the free surface.

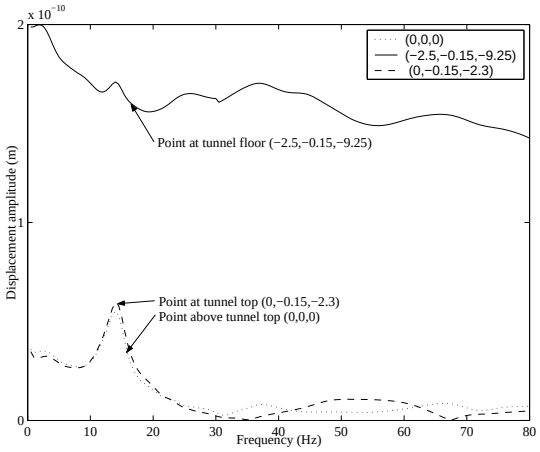

Figure 2: The amplitude of the vertical displacement of tunnel points and points at the free surface.

displacements at the points on the free surface (0,0,0), (-8,0,0), (-16,0,0) and (-24,0,0) are shown in figure 1. The transfer functions for the displacements at the tunnel points (-2.5,-0.15,-8.25) and (0,-0.15,-2.3) and at the point on the free surface (0,0,0) are shown in figure 2.

In figures 1 and 2, at low frequencies, an important peak is found at 12-18 Hz for points at the free surface close to the tunnel and for the points at the tunnel top. The peak does not appear for points further away from the tunnel.

At high frequencies, it is observed that the displacement amplitude for free surface points and for points at the tunnel top is much smaller than the amplitude found at the low frequencies. Figure 2, however, shows that the displacement amplitude in the point under the force at high frequencies is only slightly smaller than the amplitude at low frequencies.

5.2 The response on harmonic loads on the tunnel invert

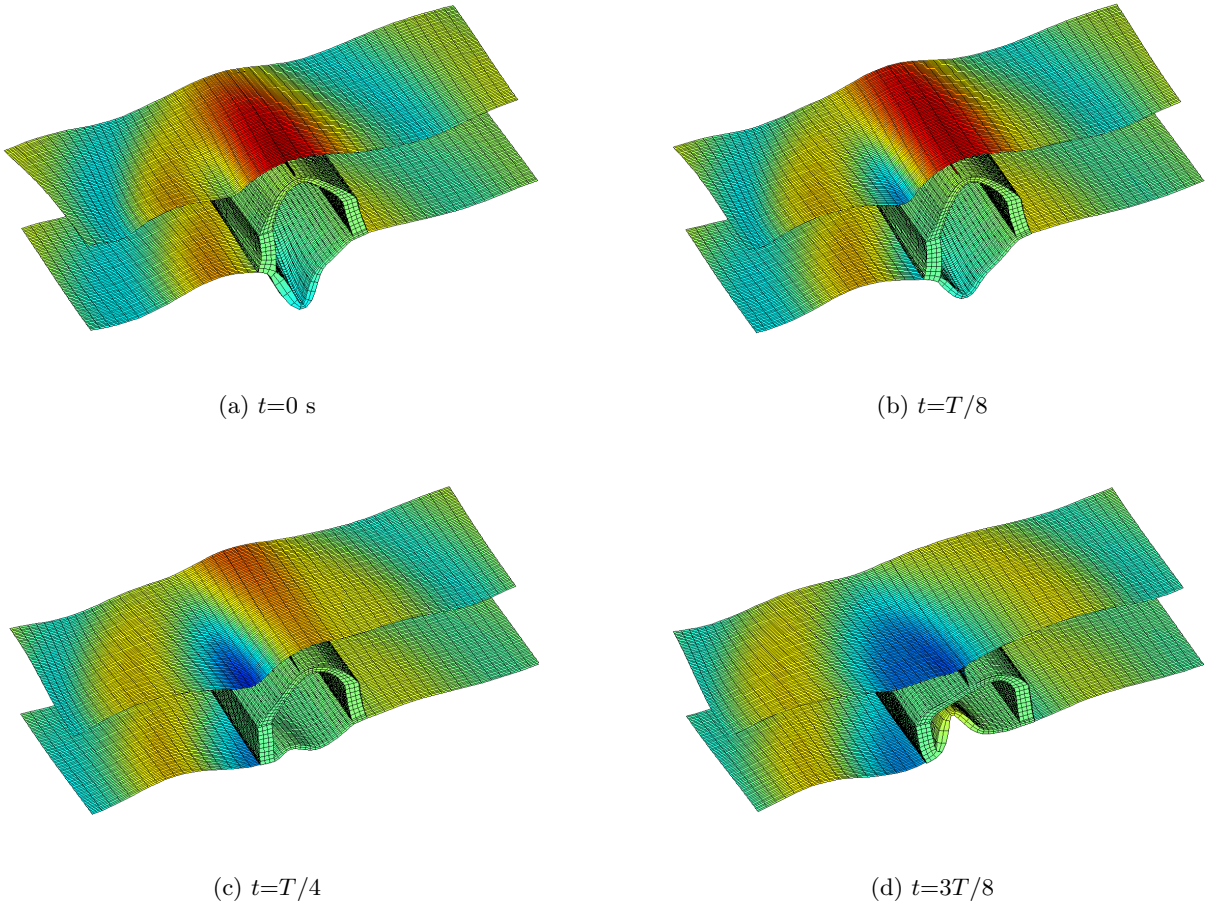

(a) t=0 s (b) t=T/8

(c) t=T/4 (d) t=3T/8

Figure 3: The harmonic response of the tunnel and the free field at 14 Hz at the time steps t=0 s, t=T/8, t=T/4 and t=3T/8 respectively, with the period T=1/14 s.

The transfer functions in the frequency domain are further investigated animating the harmonic response of the tunnel and the free field at different frequencies on the visualisation model, as presented in chapter 4. First, the low frequency response is investigated. Figure 3 shows the harmonic response at 14 Hz at the time steps t=0 s, t=T/8, t=T/4 and t=3T/8 respectively, with the period T=1/14 s.

The figure shows that the soil above the tunnel moves in phase with the tunnel roof. The soil above the tunnel can be considered to be an equivalent mass, the tunnel being an equivalent spring. The peak at 14 Hz then corresponds to the resonance peak of this mass-spring system. The peak is damped due to the radiation of waves away from the tunnel.

Figure 4 shows the harmonic response at 80 Hz at the timesteps t=0 s, t=$T/8$, t=$T/4$ and t=$3T/8$ respectively, with the period T=1/80 s. At high frequencies, an important propagation of the displacements is observed. The displacements propagate along the plates of the tunnel in the direction of the tunnel axis and perpendicular to the tunnel axis. Wave propagation in the tunnel invert also appears but the waves are strongly reflected by the tunnel walls, as can be observed from figure 5.

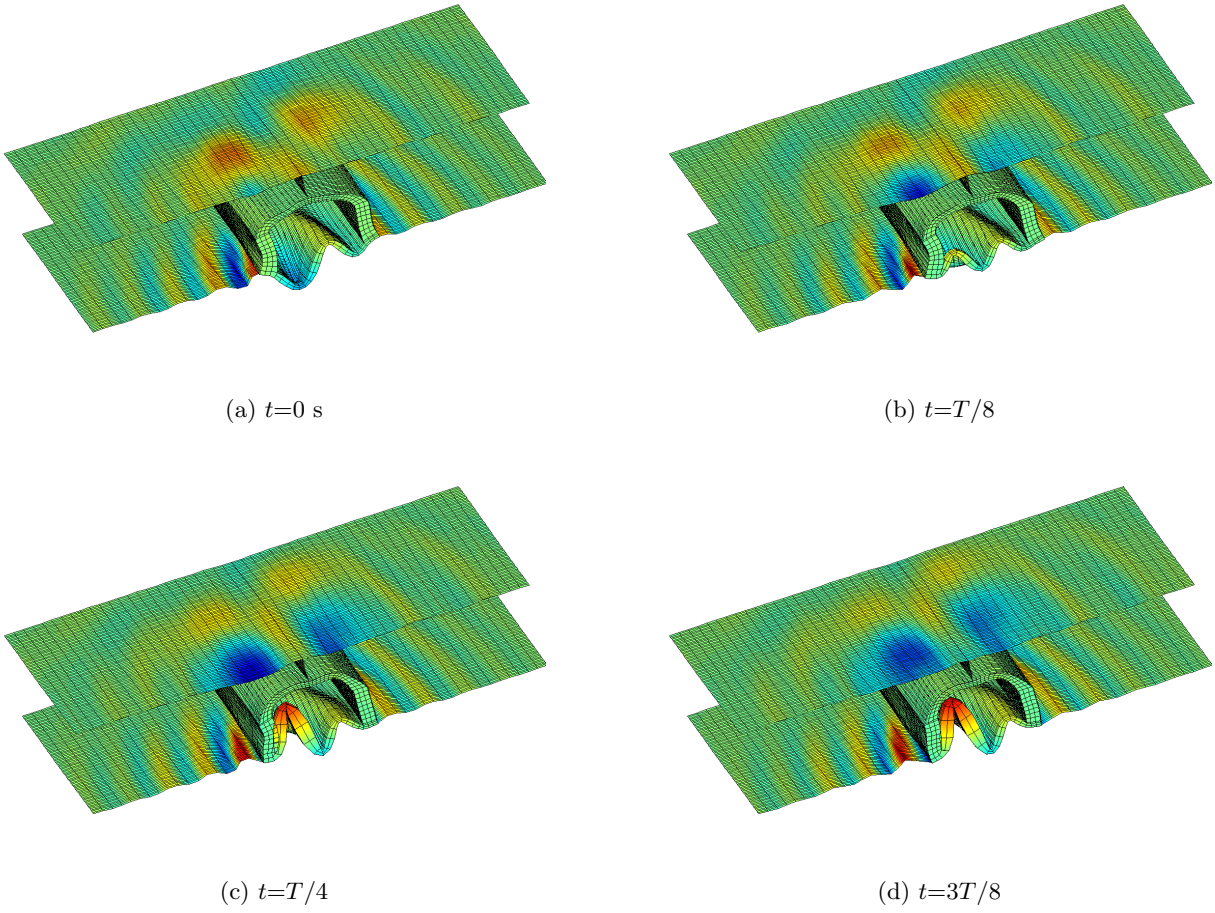

(a) t=0 s (b) t=$T/8$

(c) t=$T/4$ (d) t=$3T/8$

Figure 4: The harmonic response of the tunnel and the free field at 80 Hz at the timesteps t=0 s, t=$T/8$, t=$T/4$ and t=$3T/8$ respectively, with the period T=1/80 s.

In the soil, propagation is observed too, along and perpendicular to the tunnel axis. At the free surface above the tunnel, high phase velocities are observed in the direction along the tunnel axis. The propagation perpendicular to the tunnel shows much lower phase velocities, leading to an elliptical wave front on the free surface, as visible on figure 4.

Figure 6 shows the evolution of the phase of the vertical displacement at the free surface along

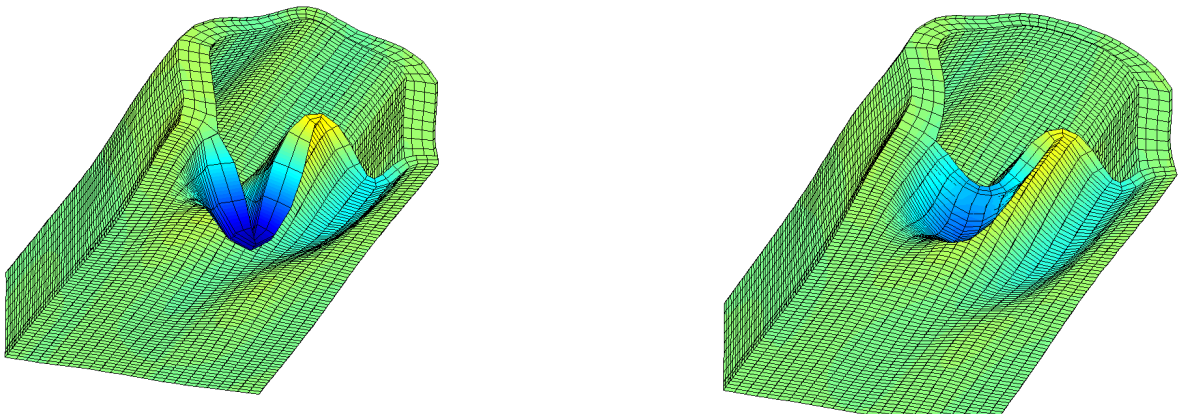

(a) t=0 s (b) t=$T/8$

Figure 5: The harmonic response of the tunnel at 80 Hz at the timesteps t=0 s and t=$T/8$ with T=1/80 s.

a line x=-4 m in the direction of the positive y-axis, at 80 Hz. A wavelength of 24 m can be estimated, corresponding to a phase speed of 1920 m/s in the direction of the tunnel. Similarly, the propagation speed of the vertical displacements perpendicular to the tunnel axis can be estimated to be approximately 650 m/s for a sinusoidal force at 80 Hz.

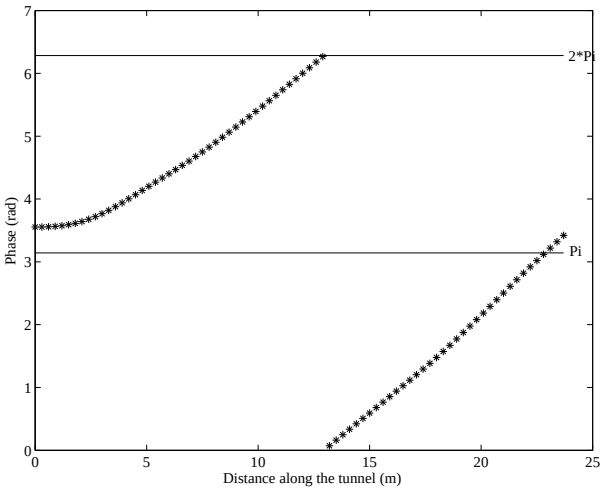

Figure 6: The phase of the vertical displacement at the free surface along a line in the y-direction at x=-4 m at 80 Hz.

5.3 The transfer functions in the slowness-frequency domain

The transfer functions in the slowness-frequency domain are investigated in order to explain the high phase velocities observed in the previous section at the higher frequencies at the free surface. The dispersion curves of different free plates, curved plates and of an infinite soil layer on an infinite plate will be computed and compared to the slowness-frequency response of the tunnel.

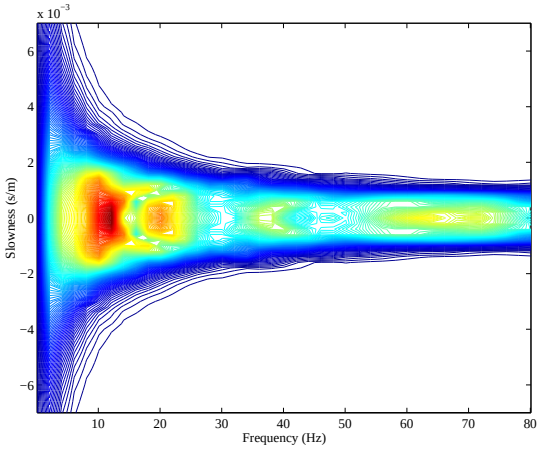

Figure 7: The amplitude of the vertical velocity in a point at the tunnel roof in the frequency-slowness domain.

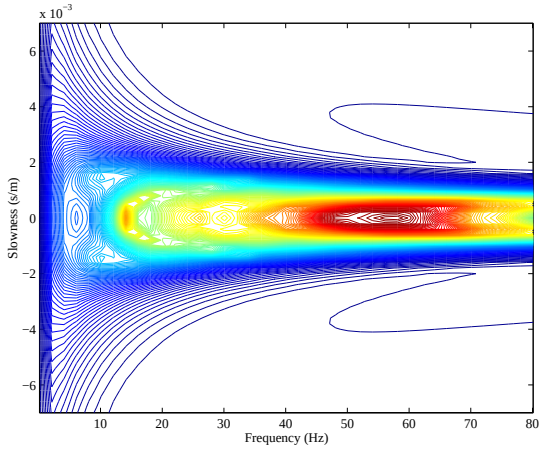

Figure 8: The amplitude of the vertical velocity in a point at the tunnel invert in the frequency-slowness domain.

This response is shown in figure 7 for a point on the tunnel roof and in figure 8 for a point on the tunnel floor, in a slowness range from -0.007 s/m to 0.007 s/m and in a frequency range form 0.1 Hz to 80.1 Hz. As discussed in chapter 2, the response is found in a slightly narrowing slowness band at high frequencies.

5.3.1 A first simplified model: an infinite plate

First, a comparison is made with the dispersion curve of an infinite free plate.

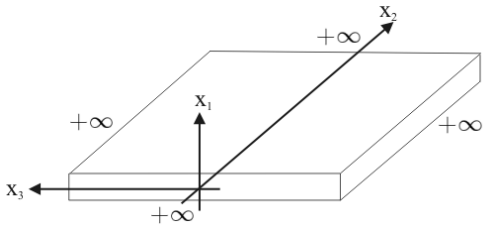

Figure 9: The model of an infinite plate.

The infinite plate and its axes are shown in figure 9.

The dynamic eigenmodes of the plate are determined. Following Bonnet-Ben Dhia [15], they are the solutions of the homogeneous equations (no source terms), periodic in time and bounded in space.

The dynamic plate equation is found in [1] and in [16]:

$$\frac{\partial^4 u_1}{\partial^4 x_2} + 2\frac{\partial^4 u_1}{\partial^2 x_2 \partial^2 x_3} + \frac{\partial^4 u_1}{\partial^4 x_3} + \frac{\rho h}{D}\frac{\partial^2 u_1}{\partial^2 t} = \frac{q}{D} \text{ with } D \equiv \frac{Eh^3}{12(1-\nu^2)} \tag{5.1}$$

The source term q is the vertical force applied on the plate. This force q are zero (homogeneous equation); the following solution is proposed:

$$u_1 = Re(u_1(x_3)e^{i\kappa x_2}e^{i\omega t})$$

This solution is periodic in time.

An invariance in the direction x_3 is assumed. The plate equation then yields:

$$(i\kappa)^4 + \frac{\rho h}{D}(i\omega)^2 = 0 \tag{5.2}$$

When solved for κ, this equation has four solutions. After eliminating the non-bounded solutions, the following two solutions are retained:

$$\kappa = \pm i\sqrt[4]{\frac{\omega^2 \rho h}{D}} \tag{5.3}$$

$$c = \frac{\omega}{\kappa} = \sqrt{\omega}\sqrt[4]{\frac{D}{\rho h}} \tag{5.4}$$

Dispersion is found. Indeed the phase speed c depends on the frequency (equation (5.4)). The higher the frequency, the larger the phase speed.

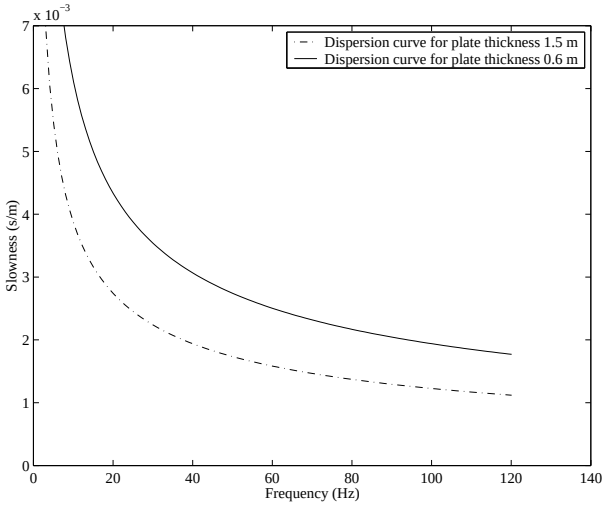

Figure 10: The dispersion curves for a plate with thickness 0.6 m and for a plate with thickness 1.5 m. Ths slowness (the inverse of the phase speed determined by the dispersion relation (5.4) is shown in function of the frequency.

Figure 10 shows the dispersion curves for a plate with the characteristics of the tunnel roof at the centre of the tunnel (thickness 0.6 m) and with those of the tunnel roof plate near the tunnel wall (thickness 1.5 m). At 80 Hz, phase speeds of 462 m/s and 729 m/s are found, corresponding to slowness of 0.0021 s/m and 0.0014 s/m respectively. These speeds thus are too small to explain the fast propagation along the tunnel.

5.3.2 The influence of the plate curvature

The tunnel at the Cité Universitaire site has a roof that has been modelled as an elliptically curved plate. The longitudinal bending mode of the roof plate is stiffened by the curvature, increasing the phase speeds found in the previous paragraph. The influence, however, is very small. Doyle [16] derives that the curvature causes terms $\sim \frac{9}{4R^4}$ that have to be evaluated against $\frac{\omega^2 \rho h}{D}$. For the roof plate at the Cité Universitaire site with a radius $R \approx 7.25$ m:

$$\frac{\omega^2 \rho h}{D} = 3.2 \text{ m}^{-2} >> \frac{9}{4R^4} = 8.2e^{-4} \text{ m}^{-2} \tag{5.5}$$

At the lowest frequencies, the curvature thus is important. But it cannot explain the fast propagation along the tunnel at the high frequencies. The influence of the curvature at these frequencies is negligibly small. Indeed the curvature is much greater then the wavelength.

5.3.3 A second simplified model: an infinite soil layer on an infinite plate

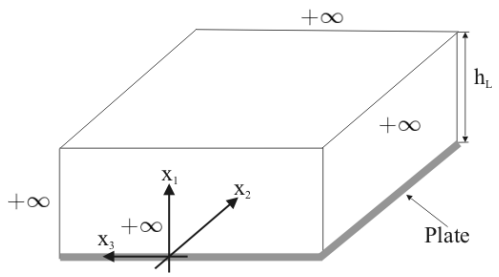

Figure 11: The model of an infinite layer on an infinite plate.

A simple free plate model could not explain the high phase velocities at the free surface. The soil layer above the tunnel roof plate must be taken into account. The dispersion curves in the slowness-frequency domain of an infinite soil layer on an infinite plate are therefore computed.

The infinite system and its axes are shown in figure 11. The problem is simplified supposing an invariance in the x_3-direction. The displacements in the x_1-x_2-directions then uncouple from the displacements in the x_3-direction and only P-SV waves can then be considered for the x_1-x_2-components (when the boundary conditions don't couple the displacements again) [15].

The following form for the displacements in the soil can be proposed:

$$\tilde{\boldsymbol{u}}_s(\boldsymbol{x}, t) = Re(\boldsymbol{u}_s(\boldsymbol{x}) e^{i\omega t}) \tag{5.6}$$

A classical Hemholtz decomposition, accounting for the invariance in the x_3-direction, then leads to:

$$u_{s1} = \frac{\partial \varphi(x_1, x_2)}{\partial x_1} + \frac{\partial \psi(x_1, x_2)}{\partial x_2} \tag{5.7}$$

$$u_{s2} = \frac{\partial \varphi(x_1, x_2)}{\partial x_2} - \frac{\partial \psi(x_1, x_2)}{\partial x_1} \tag{5.8}$$

Assuming,

$$\boldsymbol{u}_s(x_1, x_2) = \hat{\boldsymbol{u}}_s(x_1)e^{i\kappa x_2} \tag{5.9}$$

the following form is found for the potentials:

$$\varphi(x_1, x_2) = \hat{\varphi}(x_1)e^{i\kappa x_2} \tag{5.10}$$

$$\psi(x_1, x_2) = \hat{\psi}(x_1)e^{i\kappa x_2} \tag{5.11}$$

with:

$$\hat{u}_{s1}(x_1, x_2) = \frac{\partial\hat{\varphi}(x_1)}{\partial x_1} + (i\kappa)\hat{\psi}(x_1) \tag{5.12}$$

$$\hat{u}_{s2}(x_1, x_2) = (i\kappa)\hat{\varphi}(x_1) - \frac{\partial\hat{\psi}(x_1)}{\partial x_1} \tag{5.13}$$

The governing equations are the Navier equations:

$$\Delta\varphi(x_1, x_2) + \frac{\omega^2}{c_p^2}\varphi(x_1, x_2) = 0 \tag{5.14}$$

$$\Delta\psi(x_1, x_2) + \frac{\omega^2}{c_s^2}\psi(x_1, x_2) = 0 \tag{5.15}$$

Introducing equations (5.10) and (5.11) leads to the following form of the solutions:

$$\hat{\varphi}(x_1) = A_p e^{ik_{1p}x_1} + A'_s e^{-ik_{1p}x_1} \tag{5.16}$$

$$\hat{\varphi}(x_1) = A_s e^{ik_{1s}x_1} + A'_s e^{-ik_{1s}x_1} \tag{5.17}$$

with:

$$k_{1p} = \sqrt{\frac{\omega^2}{c_p^2} - \kappa^2} \tag{5.18}$$

$$k_{1s} = \sqrt{\frac{\omega^2}{c_s^2} - \kappa^2} \tag{5.19}$$

The boundary conditions to be imposed are:

- The free surface boundary conditions at $x_1 = h_L$:

$$\sigma(\boldsymbol{u}_s) \cdot \boldsymbol{e}_1\Big|_{x_1=h_L} = 0 \tag{5.20}$$

  For the x_1-x_2-components, with equation (5.9) and with $\sigma_{ij}(\boldsymbol{u}) = \lambda(div\boldsymbol{u})\delta_{ij} + 2\mu\epsilon_{ij}(\boldsymbol{u})$, these conditions yield:

$$\begin{cases} \left\{(\lambda(\frac{\partial\hat{u}_{s1}}{\partial x_1} + (i\kappa)\hat{u}_{s2}) + 2\mu\frac{\partial\hat{u}_{s1}}{\partial x_1})e^{i\kappa x_2}\right\}\Big|_{x_1=h_L} = 0 \\ \left\{\mu((i\kappa)\hat{u}_{s1} + \frac{\partial\hat{u}_{s2}}{\partial x_1})e^{i\kappa x_2}\right\}\Big|_{x_1=h_L} = 0 \end{cases} \tag{5.21}$$

  Equations (5.12) and (5.13), and afterwards equations (5.16) and (5.17) are introduced in equations (5.21), leading to two equations.

- The soil displacements at $x_1 = 0$ are introduced as the displacements u_{pl1} in the plate equation (continuity). The normal soil traction at $x_1 = 0$ then must be equal to the force q in the plate equation (equilibrium):

$$\begin{cases} u_{pl1} = u_{s1}\Big|_{x_1=0} \\ q = (\sigma(\boldsymbol{u}_s) \cdot \boldsymbol{e}_1)_1\Big|_{x_1=0} \end{cases} \tag{5.22}$$

  And with equation (5.9):

$$\begin{cases} u_{pl1} = \hat{u}_{s1} e^{i\kappa x_2}\Big|_{x_1=0} \\ q = \left\{(\lambda(\frac{\partial \hat{u}_{s1}}{\partial x_1} + (i\kappa)\hat{u}_{s2}) + 2\mu\frac{\partial \hat{u}_{s1}}{\partial x_1})e^{i\kappa x_2}\right\}\Big|_{x_1=0} \end{cases} \tag{5.23}$$

  These equations are introduced in the plate equation (5.1). Afterwards introducing equations (5.12) and (5.13), and finally equations (5.16) and (5.17) leads to one equation.

- Only plate bending is taken into account. The plate displacements in the x_2-direction are very small with respect to the displacements in the x_2-direction at $x_1 = 0$. For simplification, the plate displacements in the x_2-direction are supposed to be vanishing at $x_1 = 0$. Continuity then imposes vanishing x_2-displacements on the soil layer at $x_1 = 0$:

$$u_{s2}\Big|_{x_1=0} = 0 \tag{5.24}$$

  And with equation (5.9):

$$\hat{u}_{s2} e^{i\kappa x_2}\Big|_{x_1=0} = 0 \tag{5.25}$$

  Afterwards introducing equation (5.13), and finally equations (5.16) and (5.17) in this equation leads to one equation.

These four boundary conditions can be elaborated to a system of four homogeneous equations in four variables A_p, A'_p, A_s and A'_s, having a non-vanishing solution only when the determinant of the system matrix is vanishing. Only certain combinations of frequency and wavenumber make the determinant vanishing and these combinations are the dispersion curves of the infinite soil layer on an infinite plate system.

The dispersion curves are computed for a soil layer with the average characteristics of the two soil layers above the tunnel on top of a plate having the characteristics of the tunnel roof. They are shown in figure 14 in a slowness range from -0.0018 s/m to 0.0018 s/m and in a frequency range from 20 to 120 Hz.

Figure 12 shows the response of the tunnel in the same slowness and frequency ranges in a point at the tunnel roof for a force on the tunnel floor. To excite the phenomenon of the fast propagation more, the force can be applied on the tunnel roof, leading to a response shown in figure 13.

In figure 15, the dispersion curves have been plotted on top of the tunnel response for the force on the roof. The maxima of this response are found in the vicinity of the dispersion curves. At the higher frequencies, the dispersion curves have a smaller radius of curvature. Indeed, for increasing

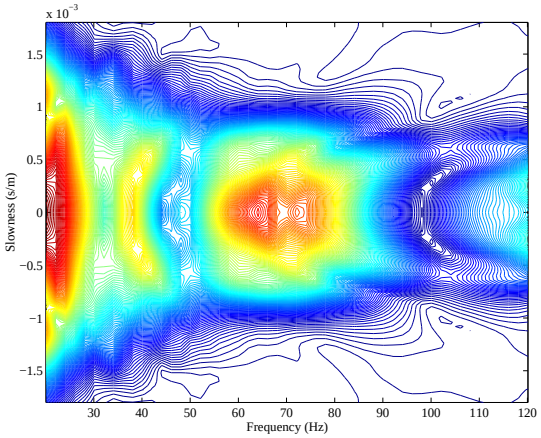

Figure 12: The amplitude of the vertical velocity in a point at the tunnel roof for a force applied at the tunnel invert in the frequency-slowness domain.

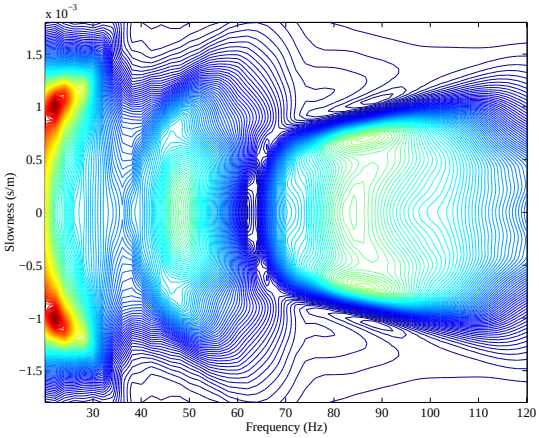

Figure 13: The amplitude of the vertical velocity in a point at the tunnel roof for a force applied at the tunnel roof in the frequency-slowness domain.

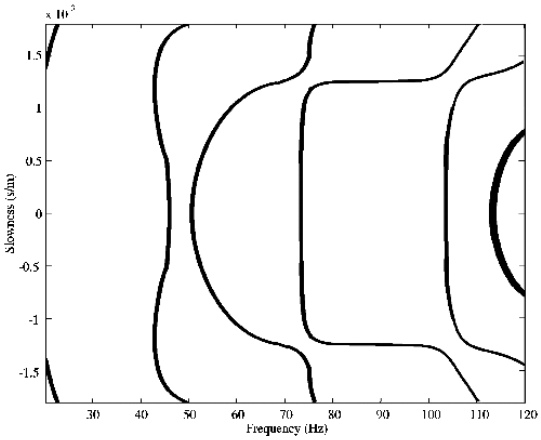

Figure 14: The dispersion curves of the infinite soil layer on an infinite plate model in the frequency-slowness domain.

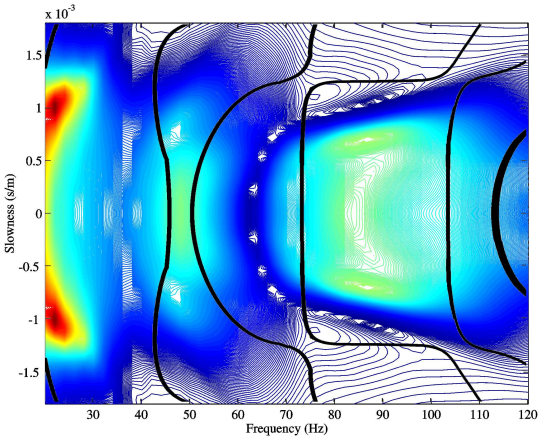

Figure 15: The dispersion curves of an infinite soil layer on infinite plate system on top of the amplitude of the vertical velocity in a point at the tunnel roof for a force applied at the tunnel roof in the frequency-slowness domain. (more contours than in figure 13 are shown.)

frequencies, the tunnel response is found in a narrowing slowness range. The dispersion curves determined by the simplified model thus explain the content in the frequency-slowness domain of the vertical displacement component in the soil above the tunnel roof at higher frequencies. With a reasonable agreement, the wave propagation in the tunnel roof-top layers system can be compared with the propagation in the simplified model of the infinite soil layer on an infinite plate.

Neither the model of a free plate, neither the model of the curved free plate was able to explain the fast propagation observed at the free surface avove the tunnel roof. The soil layer above the plate must be included in the simplified model for a reasonable ressemblance with the wave propagation above the tunnel roof. The high phase velocities along the tunnel can thus be attributed to guided waves inside the tunnel roof-top layers system.

5.3.4 A third simplified model: an infinite plate on an elastic half space

The analysis of the tunnel response in the slowness frequency domain can be finalized with a third simplified model. Similarly to the model of an infinite soil layer on top of an infinite plate, a model of an infinite plate on top of an elastic half space is made, serving as a simplified model for the tunnel bottom plate on top of the half space of the Cité Universitaire site.

The determinant of the system matrix of the simplified model is computed for the half space of the Cité Universitaire site and for a plate with the characteristics of the tunnel bottom plate. The modulus has been plotted in figure 17 in a slowness range from -0.005 s/m to 0.005 s/m and in a frequency range form 10.1 Hz to 100.1 Hz.

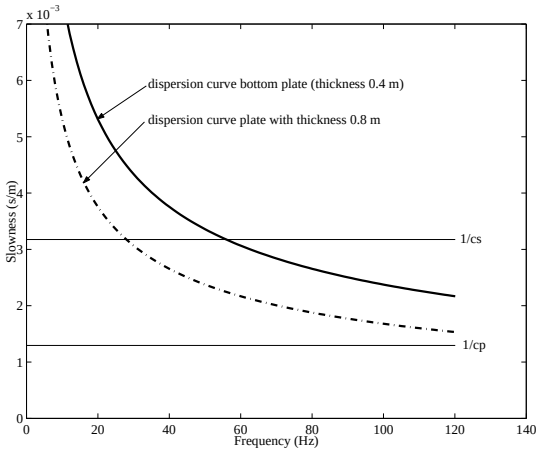

Figure 16: The dispersion curves of a free plate with the characteristics of the bottom plate of the tunnel; of a free plate with the double thickness of the tunnel bottom plate of the tunnel. c_p and c_s are the phase speeds of the third soil layer.

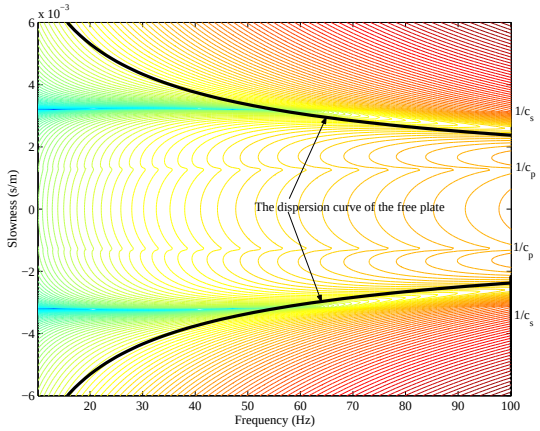

Figure 17: The modulus of the determinant divided by ω^2 of the infinite plate on elastic half space model versus slowness and frequency (for a plate with thickness 0.4 m). The colour scale is logaritmic.

It is difficult to distinguish dispersion curves (lines corresponding to a vanishing determinant). However, the zone wherein the determinant remains very small has clear features.

At high frequencies, this zone is limited by the dispersion curve of the free plate (figure 17). At

these frequencies the wavelength in the soil is small and the bending waves in the plate almost only feel the plate.

At low frequencies, the wavelength in the soil is larger and the waves in the plate feel the soil. The zone of the very small determinant has a limited extension above the line $1/c_R$ or $1/c_s$ in the slowness-frequency domain. The extension is lareger for lower frequencies.

The zone of the small determinant computed by the simplified model can be compared to the tunnel response computed by the 3D tunnel model (figures 7 and 8). The response shows the predicted features: at higher frequencies, the response is limited in a slightly narrowing slowness band. At lower frequencies, the contents broadens and is limited by a line between $1/c_R$ and the free plate dispersion curve.

It is difficult to make an accurate estimation of the stiffness of the plate for the computation with the simplified model. Figure 17 has been made using the characteristics of the bottom plate of the tunnel. This can be a good estimation at the high frequencies, since the animations show that the bottom plate then behaves rather independently from the tunnel walls. For the low frequencies, the bottom plate is stiffened by the tunnel walls and the tunnel roof. The effect is estimated in figure 16 where a dispersion curve of a stiffer plate is drawn.

5.4 The response on transient loads on the tunnel invert

5.4.1 The transient tunnel excitation

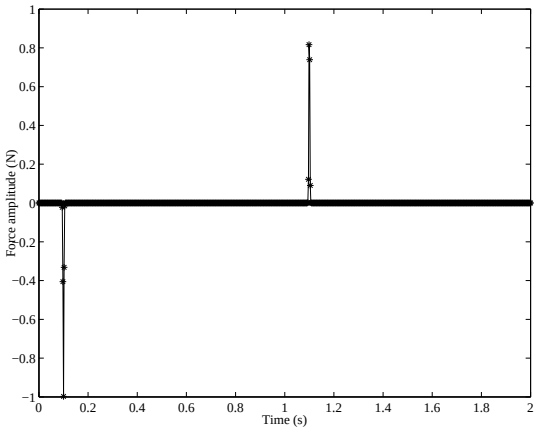

Figure 18: Time history of the applied Gaussian force (t_1=0.1 s, t_2=1.1 s and T=0.0025 s).

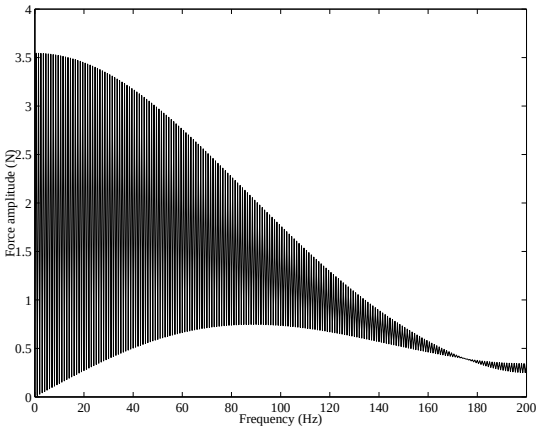

Figure 19: Frequency content of the applied Gaussian force.

In this section, the transient response of the tunnel and the free field is computed due to a hammer impact on the tunnel invert. The hammer is modelled in the time domain by means of a very narrow Gaussian function:

$$f(t) = -e^{-\frac{t^2}{T^2}} \text{ with } T\text{=}0.0025 \text{ s.} \tag{5.26}$$

Due to the limitations on the computation of Green's functions of a layered half space, the

3D tunnel-soil interaction model cannot compute the quasi-static response ($\omega = 0$ rad/s). The Fourier transform of a Gaussian function however is a Gaussian function and its static component is not vanishing. In order to overcome this problem, two hammer impacts are applied, the first impact in the negative z-direction (figure 18) (downwards) and the second, one second later, in the positive Z-direction (upwards). As a result, the static component of the load vanishes. However, this technique requires a finer sampling with respect to the frequency. Indeed, as can be observed from figure 19, the frequency content of the applied force oscillates heavily. The shift in the time domain $t_2 - t_1$ between the second and the first hammer impact introduces a factor $(e^{i\omega t_1} - e^{i\omega t_2})$ in the frequency domain. With $f(t)$ and $F(\omega)$ the time history and the frequency content of a single downwards Gaussian hammer impact:

$$f(t) \leftrightarrow F(\omega) \tag{5.27}$$

$$f(t - t_1) - f(t - t_2) \leftrightarrow F(\omega)(e^{i\omega t_1} - e^{i\omega t_2}) \tag{5.28}$$

The fast Fourier transform algorithm is used to compute the transformations between the time and the frequency domain. A time window of 2 seconds is chosen. The step in the frequency domain is 0.5 Hz and the frequency range goes up to 200 Hz. A step in the time domain of 0.0025 s is used. Figures 18 and 19 show the time history and the frequency content of the applied force.

5.4.2 The transient tunnel response

The response on the first hammer impact, the downwards Gaussian force, has been animated on the visualization model.

Figure 20 shows the response at the timesteps t=0.1 s, t=0.116 s, t=0.136 s and t=0.0156 s, respectively.

Figure 20a shows the hammer impact on the tunnel invert (t=0.1 s). Figure 20b is shortly after the impact (t=0.116 s). At the free surface, downwards displacements can be observed close to the tunnel. However, small upwards displacements are observed on the whole free ground surface further away from the tunnel. Figure 20c and 20d are more time after the impact (t=0.136 s and t=0.156 s). A bigger front of vertical downwards displacements propagates away from the tunnel, immediately followed by a front of vertical upwards displacements.

In order to investigate the propagation perpendicular to the tunnel, seismograms have been made of the horizontal and vertical displacement components at the free surface on the line y=0 (figure 6 in chapter 4). These seismograms are shown in figures 21 and 22.

Comparison with the response on single forces in the stratigrapy

Five different types of waves can be identified on these seismograms. All waves are emitted by the tunnel and are propagating in a layered half space. Thus, this wave field can be compared to waves induced by single forces at different depths in the stratigraphy. The same Gaussian forces are applied at 0 m, 3 m and 9 m, corresponding respectively to the free surface, the depth of the tunnel roof and the depth of the tunnel invert. The transfer functions in the slowness-frequency domain are given in figures 23, 25 and 27. The seismograms with the vertical response at the free surface are shown in figures 24, 26 and 28.

First the response at a Gaussian force, applied at the free surface, is investigated. Waves (1) and (2) in the seismogram are classical refracted waves in the layers on top of the underlying half

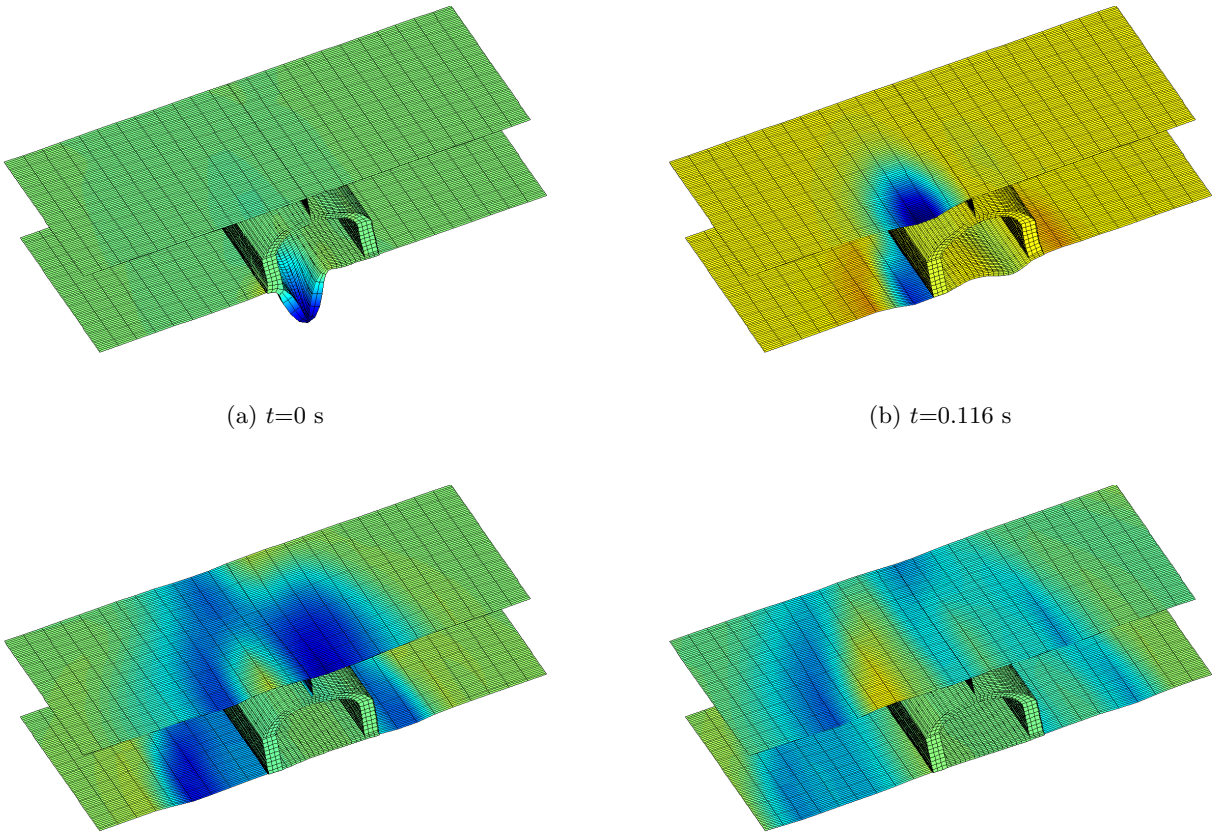

(a) t=0 s

(b) t=0.116 s

(c) t=0.136 s

(d) t=0.156 s

Figure 20: The response of the tunnel and the free field on the downwards Gaussian hammer impact at the timesteps t=0.1 s, t=0.116 s, t=0.136 s and t=0.0156 s, respectively.

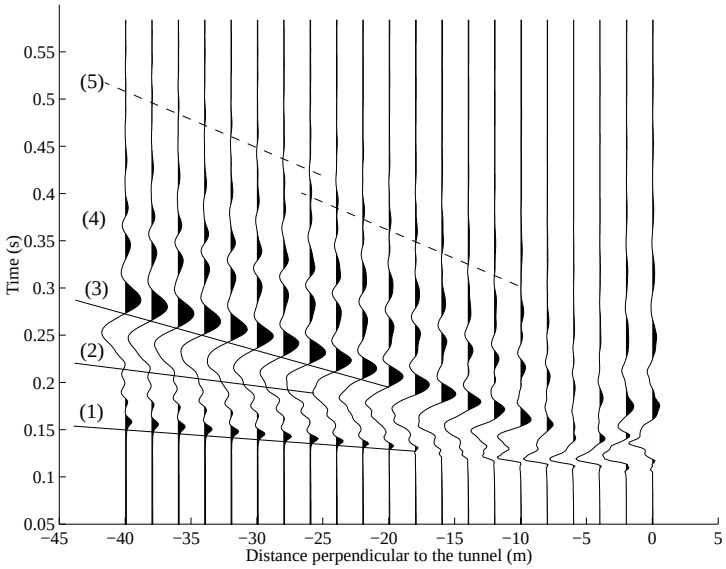

Figure 21: The seismogram of the vertical displacements for points on a line y=0 at the free surface for the Gaussian transient force applied at the tunnel invert.

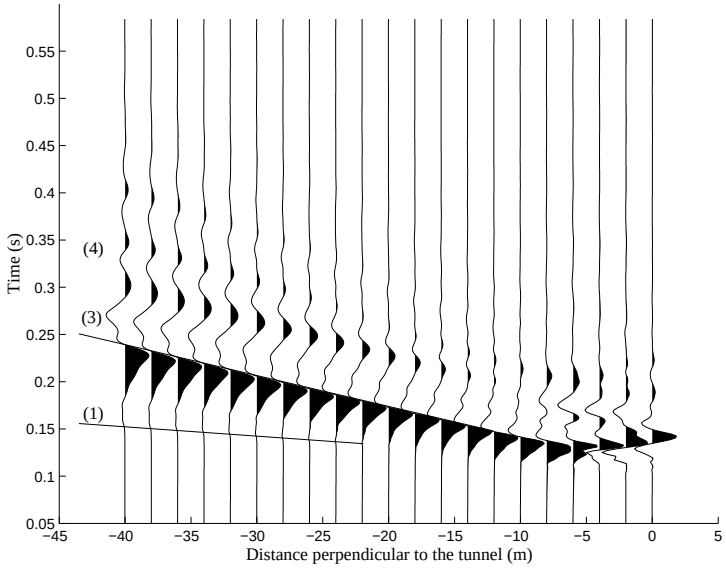

Figure 22: The seismogram of the horizontal displacements for points on a line y=0 at the free surface for the Gaussian transient force applied at the tunnel invert.

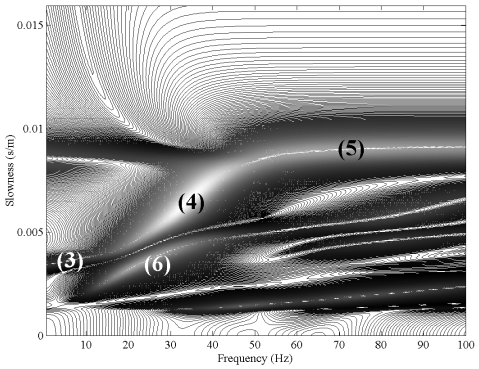

Figure 23: The amplitude of the vertical displacement in the $\omega - p$ domain for a vertical Dirac impulse applied at a depth of 0 m.

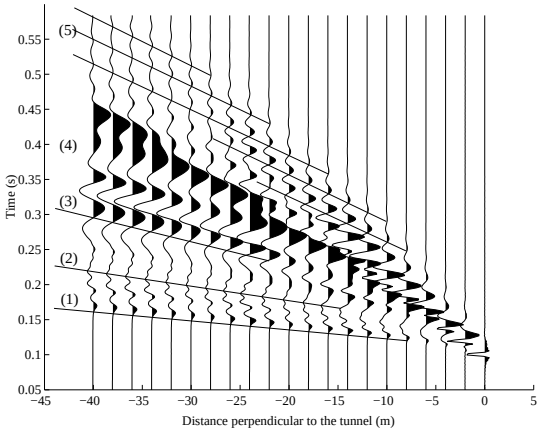

Figure 24: The seismogram of the vertical displacements for points on a line y=0 at the free surface for the Gaussian transient force applied at a depth of 0 m.

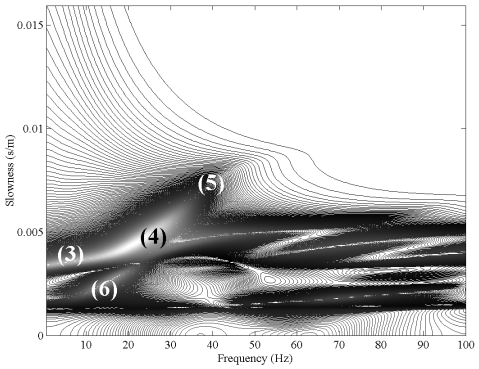

Figure 25: The amplitude of the vertical displacement in the $\omega - p$ domain for a vertical Dirac impulse applied at a depth of 3 m.

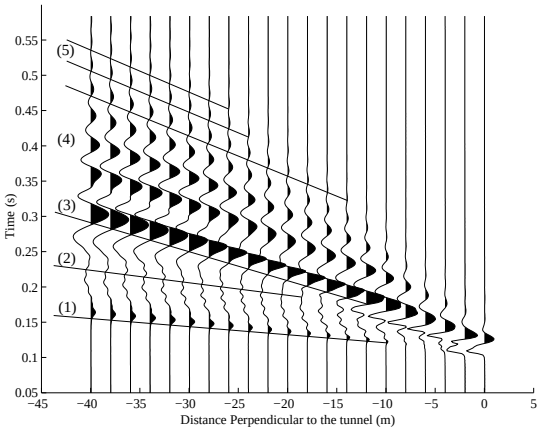

Figure 26: The seismogram of the vertical displacements for points on a line y=0 at the free surface for the Gaussian transient force applied at a depth of 3 m.

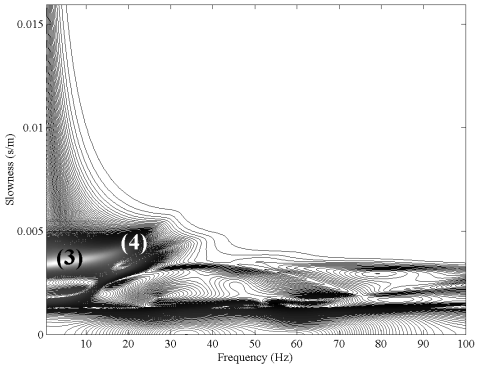

Figure 27: The amplitude of the vertical displacement in the $\omega - p$ domain for a vertical Dirac impulse applied at a depth of 9 m.

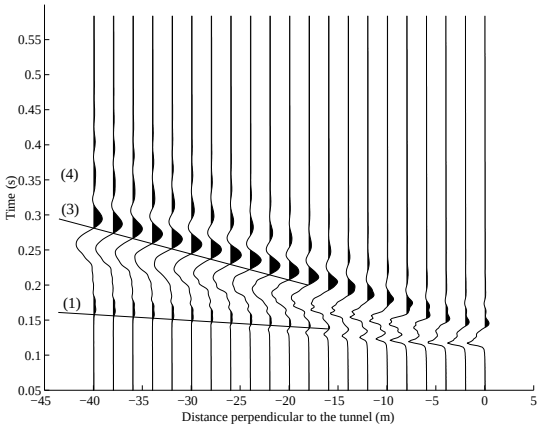

Figure 28: The seismogram of the vertical displacements for points on a line y=0 at the free surface for the Gaussian transient force applied at a depth of 9 m.

space, propagating at the P-wave speed of the half space and of the second layer respectively. Waves emitted at the free surface and arriving at the interface between the first layer and the second layer at the critical angle of incidence, cause refracted waves that propagate along the interface at the speed of the underlying second layer. They emit waves propagating upwards at the critical angle. Similar waves exist at the interface between the second layer and the half space. These waves result in the observation at the free surface of waves (1) and (2) [2].

Waves (3) correspond to the Rayleigh waves of the half space at low frequencies. Waves (5) correspond to the Rayleigh waves of the first layer at high frequencies.

Two important peaks (4) and (6) in the $\omega - p$ domain cause highly dispersive waves (4) in the seismogram. Waves (4) are the Rayleigh waves of the layering between the Rayleigh wave of the first layer (5) and the Rayleigh wave of the half space (3).

The response on a Gaussian force, applied at a depth of 3 m, can be examined similarly. Figure 25 shows that the force at a depth of 3 m can hardly excite the high-frequent Rayleigh wave of the first layer. The refracted waves (1) and (2), as well as the Rayleigh waves (3) and (4) are clearly observed in the seismogram.

Finally, the response on a Gaussian force, applied at a depth of 9 m is investigated. The low-frequent Rayleigh wave of the half space (3) remains the most important peak in the $\omega - p$ domain. Rayleigh wave (4) can hardly be observed. Only refracted wave (1) is found.

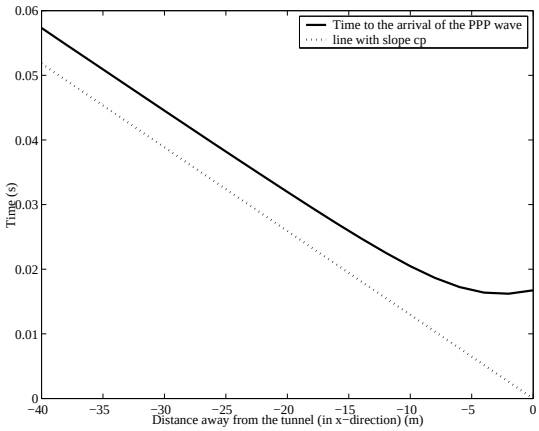

Figure 29: The time to the arrival at the free surface of a refracted P-wave created at t=0 s at the point (-2.5,0,-8.25).

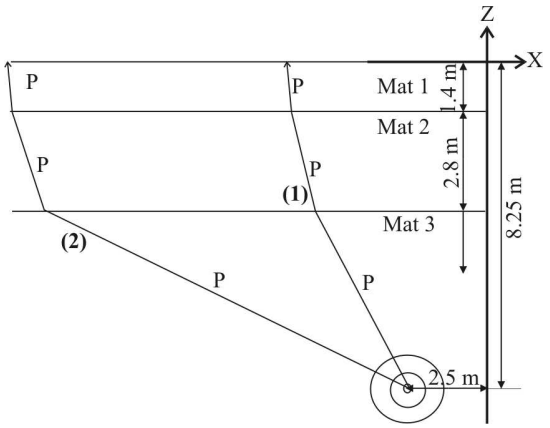

Figure 30: Two refracted P-waves created by a source at the point (-2.5,0,-8.25); (the reflected waves and the created SV waves have been omitted).

The curvature of the waves in the seismograms

The waves in the seismogram of figure 28 for the force at a depth of 9 m, as well as the waves in the seismogram of figure 21 of the 3D tunnel model have a significant curvature for points at the free surface in the vicinity of the single force or of the tunnel. The reason is explained in figures 29 and 30. Figure 29 shows the time to the arrival at the free surface of a refracted P-wave created at t=0 s at the point (-2.5;0;-8.25). For the points at the free surface close to the source, it is understood from figure 30, that it is mostly the vertical distance to the free surface that determines the time to the arrival of this wave. For points at the free surface, in the

vicinity of the source, the distance to the source is almost constant which causes a small slope of the curve in figure 29 for these points.

For points further away from the source, the important distance becomes rather the horizontal distance. At each interface, the P-wave is refracted more vertically to the free surface. The only way for this wave to reach points far away from the source thus is to stay a long distance in the third layer and then to refract to the surface. The curve in figure 29 thus has a slope equal to the P-wave speed of the third layer for points further away. The transition from the small slope to the slope $C_p(3)$ for the far points thus causes the effect of curvature.

Conclusion: the propagation perpendicular to the tunnel

It can now be understood that the tunnel bottom plate excites the Rayleigh wave of the half space at low frequencies ((3) in seismogram 21) and generates body waves in the fast half space ((1) in the seismogram). The upper parts of the tunnel walls and the tunnel roof generate refracted waves in the layering ((1) and (2) in the seismogram). This upper part of the tunnel still contributes to Rayleigh waves of the half space at low frequencies, but it is only this part that can excite the dispersive Rayleigh waves (4) at medium frequencies and the high frequency Rayleigh waves of the first layer (5).

5.5 Conclusion and further development

In this chapter, the 3D model describing tunnel-soil interaction has been analysed. The model has been used to compute response in the tunnel and in the free field due to harmonic and transient loads on the tunnel invert.

Animations of the results have been used to make interpretations about the tunnel-soil interaction.

It has been shown that the tunnel and the soil response in the vicinity of the tunnel are strongly affected by the free surface and the layering. In particular, a low frequency resonance of the soil mass above the tunnel has been identified. Moreover, the computed results have shown a high anisotropy of wave propagation along the tunnel and perpendicular to it. High phase velocities along the tunnel have been attributed with a reasonable agreement to guided waves inside the tunnel roof-top layers system. It has also been shown that the wave-field radiated at some distance from the tunnel is mainly governed by refracted waves and generalized Rayleigh waves of the layered medium. The high frequency filtering induced by the source embedding has been shown to be governed by the depth of the tunnel roof and not by the depth of the tunnel invert. As a conclusion, the wave-field induced by a point force applied at the bottom of the tunnel cannot be approximated by an equivalent force in the soil at the corresponding depth since an additional force at the roof depth seems to be needed to mimic the coupled numerical solution.

Within the frame of the Convurt project, a similar model is made of a site on the Bakerloo and Jubilee lines in London. This tunnel is a deep bored tunnel. The layer above the tunnel roof plate is approximately 24 m thick, much more than the 2.1 m for the tunnel considered in this work. A comparison of the results of the two models will be possible. In particular, an analysis of the influence of the tunnel depth on the (fast) propagation in the direction of the tunnel will

be very interesting.

The periodic tunnel-soil interaction model used in this paragraph is the basic ingredient allowing a computation of more complex problems. Further research will include the track, the ballast and the sleepers in the model. The case of a moving load will be considered. And an excitation model will be introduced. Finally, the propagation of uncertainties in the model will be investigated by means of Monte Carlo simulations.

In the next chapter, the periodic tunnel model will be used to compute the transmission to a nearby building. The displacement field emitted by the tunnel will be considered to be an incident field for the building, again fully taking account of soil-structure interaction.

Chapter 6

Impulse loads on a tunnel invert: response in a nearby building

The Convurt project carried out measurements in particular sites where reradiated noise and vibrations transmitted from tunnel to adjacent structures cause disturbances. At the Cité Universitaire site in Paris, vibrations have been measured in the free field and in a nearby building, more particularly in the student residence "Maison du Mexique". In order to validate the numerical models, a 3D numerical prediction model describing the tunnel-soil and soil-building interaction have been made for this site. The approach is outlined in this chapter. Finally, results of the site model are compared to on site measurements.

6.1 The characteristics of the building

Figure 2 shows a plan view of the site, the location of the metro tunnel RER B as well as the "Maison du Mexique" between the metro stations of Cité Universitaire and Gentilly.

The "Maison du Mexique" is a 5-storey student dormitory. Figures 1 and 4 show the front view and the side view of the building. Figure 3 shows the ground floor.

In a first modelling stage, only the main central building is taken into account. The small transverse part seen on the side view is not included in the model, nor is the bigger transverse part seen on the plan.

The whole building is a reinforced concrete frame structure with two sets of eight columns 6.2 m from each other. In a first stage, only this structural frame is modelled. Later, the outer and inner walls and the stair cases will be included. These components significantly stiffen the building.

6.1.1 The location of the "Maison du Mexique" with respect to the tunnel

For the tunnel, a right-handed Cartesian frame of reference (x',y',z') is chosen, with the origin on the bottom plate of the tunnel, in the middle of the cross section and in the section wherein the hammer impact measurements were carried out. The reference frame of the tunnel is used as the global reference frame.

Figure 1: The front view of the "Maison du Mexique."

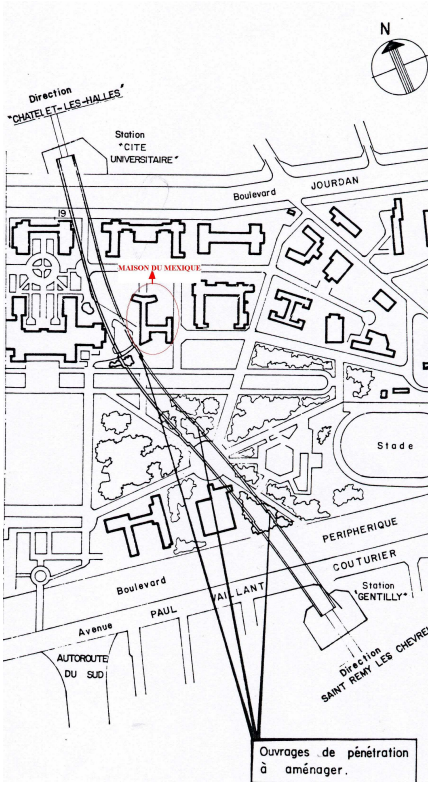

Figure 2: The plan of the test site.

Figure 3: The ground floor.

Figure 4: The side view of the "Maison du Mexique".

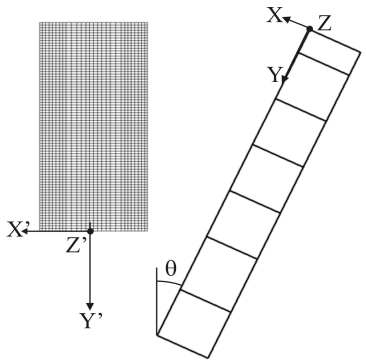

Figure 5: The position of the building with respect to the tunnel.

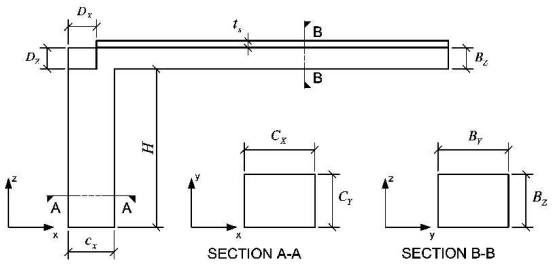

Figure 6: The beam-column connection.

The local right-handed Cartesian frame of reference of the building (x,y,z) has its origin in the lower right corner of the ground floor of the building.

Figure 5 shows the two frames of reference.

The origin of the reference frame of the building is assumed to have coordinates x'=23.49 m and y'=24.3 m in the global reference frame. The angle θ indicated on figure 5 is assumed to be 25.33°. These coordinates are approximations and should be determined more precisely for future modelling.

6.1.2 Material properties and geometrical characteristics of the building frame

As already mentioned, the building shape is a reinforced concrete frame structure. The centre-to-centre column distances vary around 6.2 m. The floor-to-ceiling height on each floor is equal to approximately 2.85 m.

The concrete is modelled with a Young modulus E of 33000 N/m^2, a Poisson ratio ν of 0.2 and a density ρ of 2500 kg/m^3 [13].

Figure 6 shows a typical beam-column connection. The dimensions of all beams and columns for all storeys are summarized in table 6.1. The slab thickness is assumed to be 13 cm.

Ceiling	C_x [m]	C_y [m]	B_y [m]	B_z [m]	D_x [m]	D_z [m]
-1	0.70	0.41	0.41	0.55	0.27	0.55
0	0.65	0.41	0.41		0.27	0.33
1	0.62	0.30	0.30	0.33	0.27	0.33
2	0.62	0.30	0.30	0.33	0.27	0.33
3	0.62	0.30	0.30	0.33	0.27	0.33
4	0.62	0.30	0.30	0.33	0.27	0.33
5	0.62	0.30	0.30	0.33	0.27	0.33

Table 6.1: Column and beam dimensions at all floors.

6.1.3 The constraint equations

A finite element model has been previously built by Christophe Coster at KULeuven [13], using the program ANSYS. At ECP, soil structure interaction is computed using the combined computer codes MISS and the Structural Dynamics Toolbox in Matlab; MISS being used for the BEM part of the problem, the SDT being used for the FEM part of the problem. The ANSYS model has been imported in the SDT in order to continue the model development in this Matlab-toolbox.

Using the SDT built-in function ans2sdt, the mesh of the structure has been easily imported. Eigenmodes computed by ANSYS can also easily be imported. However material properties, geometrical properties, element orientations and constraints are not imported.

The introduction of the material and geometrical properties and of the element orientations is relatively easy in the SDT; however the introduction of constraints is not.

In the ANSYS model, the beams were modelled using line elements, the plates were modelled using plane elements. To account for the thickness of the plates and the beams, the connection of the beams to the plates was not made using coincident nodes. Constraint equations were used relying the beam nodes to the nodes at the plate edges. The translational displacements of the nodes at the plate edges were computed from the translations and rotations of the underlying beam nodes based on the distance between the corresponding nodes. The rotations of the nodes at the plate edges were completely free. (ANSYS command CERIG with UXYZ option).

In the SDT however, this type of constraint equation is not possible (in an automatic way). In a first attempt, the constraint equations have been approximated by connecting the corresponding nodes using beam elements with a high, but penalized stiffness, using a rigid connection at the beam and a connection coupling only the translational degrees of freedom at the plate edge (SDT CELAS elements with 123 option). At higher frequencies, this however didn't give accurate results, because the penalized stiffness got too small at higher frequencies.

Therefor, another approach has been chosen and the SDT RIGID elements with 123456 option have been used: SDT then generates constraint equations based on the distance between corresponding nodes. These constraint equations, however, couple all 6 degrees of freedom and thus all 6 at the plate edges too.

As far as the implementation is concerned, the SDT generates a transformation matrix T relating all dofs $\boldsymbol{mdof}$ with the dofs $\boldsymbol{cdof}$, which are the free dofs after applying the constraint equations. The displacements defined on all dofs $\boldsymbol{u(mdof)}$ are related to the displacements on the free dofs $\boldsymbol{u(cdof)}$ as follows:

$$\boldsymbol{u(mdof)} = \boldsymbol{T} * \boldsymbol{u(cdof)}$$

The model mass matrix $\boldsymbol{m}$ and stiffness matrix $\boldsymbol{k}$, can be projected on this new basis:

$$\boldsymbol{m}_c = \boldsymbol{T}^\intercal * \boldsymbol{m} * \boldsymbol{T}$$
$$\boldsymbol{k}_c = \boldsymbol{T}^\intercal * \boldsymbol{k} * \boldsymbol{T}$$

All operations e.g. mode extraction are then performed on these projected mass and stiffness matrices [4].

6.1.4 The foundation of the building

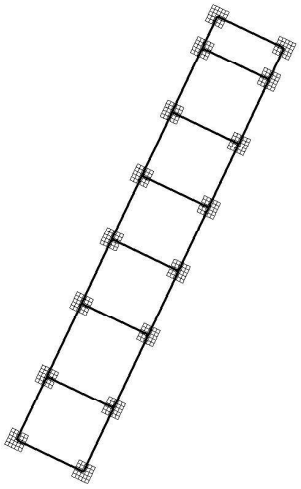

Figure 7: The chosen foundation.

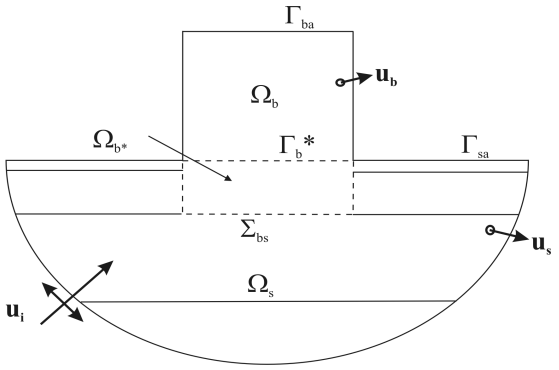

Figure 8: Model layout and notations.

A precise modelling of the foundation is necessary to obtain accurate results for the soil-structure interaction. At present, however, no information is available on the foundation of the building. A possible foundation therefore has been designed, consisting in putting individual squared plates under each column. The dimensions of the plates are determined by the bearing capacity of the soil. An ultimate limit state load on each column of 2173 kN can be estimated. Using the Mohr-Coulomb criterion, it has been concluded that a squared dimension of 1.5 m has a bearing capacity of 2243 kN and thus is a sufficient dimension (assumptions: freatic area is the free surface, dry soil weight=16 kN/m^3, saturated soil weight=20 kN/m^3, φ'=30°, c'=0 kN/m^2, safety factor of 2). A more precise computation is necessary using measured soil characteristics.

Those squared foundations are supposed to be rigid and massless, and are modelled by surface elements.

The individual foundations have been connected with beam elements, the properties of the beams being equal to the horizontal longitudinal beams at the ground floor. The beams have been coupled to the foundations only in the central point of each foundation plate. The 6 degrees of freedom have been coupled. The complete foundation is shown in figure 7.

The only modelled contact between the soil and the building consists of the rigid squared foundations plates.

6.2 The dynamic soil-structure interaction analysis

6.2.1 The kinematic basis

The displacements on Σ_{bs} are decomposed on a basis of modes $\boldsymbol{\Psi}_m(\boldsymbol{x})$, as proposed in chapter 2 . The model layout and notations are repeated in figure 8. The displacement fields $\boldsymbol{u}_b(\boldsymbol{x},\omega)$ and $\boldsymbol{u}_s(\boldsymbol{x},\omega)$ then can be expanded as:

$$\boldsymbol{u}_b(\boldsymbol{x},\omega)\Big|_{\Sigma_{bs}} = \boldsymbol{u}_s(\boldsymbol{x},\omega)\Big|_{\Sigma_{bs}} = \sum_m c_m(\omega)\boldsymbol{\Psi}_m(\boldsymbol{x}) \tag{6.1}$$

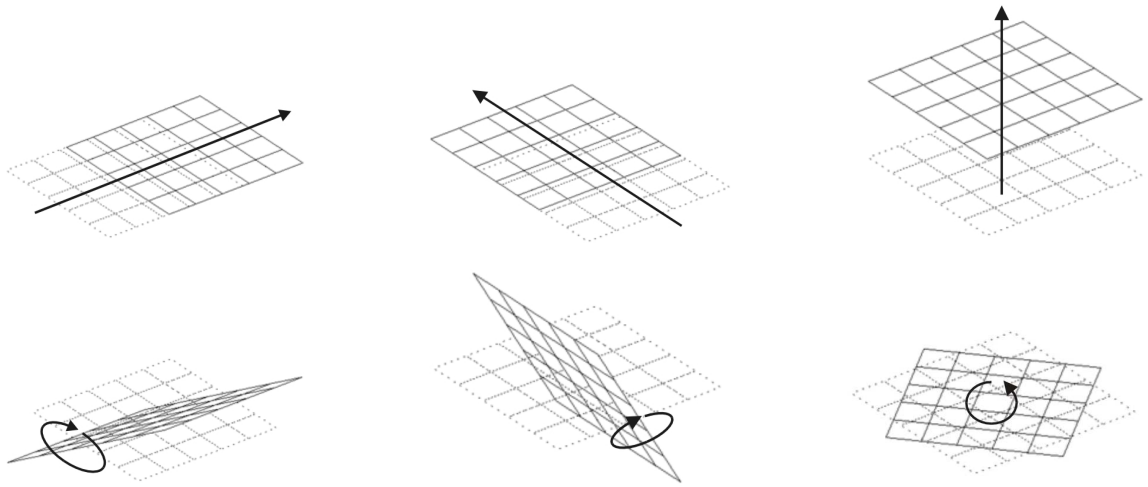

Figure 9: The 6 rigid body displacement modes of one rigid foundation plate.

$$\boldsymbol{u}_s(\boldsymbol{x},\omega) = \sum_m c_m(\omega)\boldsymbol{u}_d(\boldsymbol{\Psi}_m)(\boldsymbol{x},\omega) + \boldsymbol{u}_i(\boldsymbol{x},\omega) + \boldsymbol{u}_{d0}(\boldsymbol{x},\omega) \text{ in } \Omega_s \tag{6.2}$$

$$\text{where } \boldsymbol{u}_d(\boldsymbol{\Psi}_m)(\boldsymbol{x})\Big|_{\Sigma_{bs}} = \boldsymbol{\Psi}_m(\boldsymbol{x}); \boldsymbol{u}_i(\boldsymbol{x},\omega) + \boldsymbol{u}_{d0}(\boldsymbol{x},\omega)\Big|_{\Sigma_{bs}} = 0$$

$$\boldsymbol{u}_b(\boldsymbol{x},\omega) = \sum_m c_m(\omega)\boldsymbol{u}_b(\boldsymbol{\Psi}_m)(\boldsymbol{x}) + \sum_i c_i(\omega)\boldsymbol{\Phi}_i(\boldsymbol{x}) \text{ in } \Omega_b \tag{6.3}$$

$$\text{where } \boldsymbol{u}_b(\boldsymbol{\Psi}_m)(\boldsymbol{x})\Big|_{\Sigma_{bs}} = \boldsymbol{\Psi}_m(\boldsymbol{x}); \boldsymbol{\Phi}_i(\boldsymbol{x})\Big|_{\Sigma_{bs}} = 0$$

Since the interface Σ_{bs} consists only of the 16 foundation plates and since these foundation plates are assumed to be rigid, these modes $\boldsymbol{\Psi}_m(\boldsymbol{x})$ are chosen to be the individual rigid body modes of each of these plates, as shown on figure 9. This way, 16 times 6 modes are defined.

A set of modes $\boldsymbol{\Phi}_i(\boldsymbol{x})$ is added to the basis of modes $\boldsymbol{u}_b(\boldsymbol{\Psi}_m)(\boldsymbol{x})$. Their trace on the interface Σ_{bs} is vanishing, in order to satisfy the compatibility on the interface Σ_{bs}. The fields $\boldsymbol{\Phi}_i(\boldsymbol{x})$ are chosen to be the eigenmodes of the building resting on a rigid foundation with eigenfrequencies in the range of interest.

6.2.2 The variational formulation

The variational formulation of the problem is elaborated as in chapter 2.

The following system of equations is found:

$$(\boldsymbol{K}_s(\omega) - \omega^2\boldsymbol{M}_b + \boldsymbol{K}_b + \boldsymbol{C}_b)\begin{pmatrix}\boldsymbol{c}_M(\omega)\\ \boldsymbol{c}_I(\omega)\end{pmatrix} = \begin{bmatrix}\boldsymbol{F}_s(\omega)\\ 0\end{bmatrix} \tag{6.4}$$

The soil stiffness matrix $\boldsymbol{K_s(\omega)}$

$$\boldsymbol{K}_s(\omega) = \begin{bmatrix} \int_{\Sigma_{bs}} \boldsymbol{u}_d(\boldsymbol{\Psi})^\intercal \boldsymbol{t}_s(\boldsymbol{u}_d(\boldsymbol{\Psi}))(\omega) dS & 0 \\ 0 & 0 \end{bmatrix} \tag{6.5}$$

The soil stiffness matrix is computed by the MISS program.

The building mass matrix $\boldsymbol{M_b}$

$$\boldsymbol{M}_b = \begin{bmatrix} \boldsymbol{u}_b(\boldsymbol{\Psi})^\intercal \boldsymbol{M}_b^{FEM} \boldsymbol{u}_b(\boldsymbol{\Psi}) & \boldsymbol{u}_b(\boldsymbol{\Psi})^\intercal \boldsymbol{M}_b^{FEM} \boldsymbol{\Phi} \\ \boldsymbol{\Phi}^\intercal \boldsymbol{M}_b^{FEM} \boldsymbol{u}_b(\boldsymbol{\Psi}) & \boldsymbol{\Phi}^\intercal \boldsymbol{M}_b^{FEM} \boldsymbol{\Phi} \end{bmatrix} \tag{6.6}$$

The matrices $\boldsymbol{u}_b(\boldsymbol{\Psi})^\intercal \boldsymbol{M}_b^{FEM} \boldsymbol{u}_b(\boldsymbol{\Psi})$, $\boldsymbol{u}_b(\boldsymbol{\Psi})^\intercal \boldsymbol{M}_b^{FEM} \boldsymbol{\Phi}$ and $\boldsymbol{\Phi}^\intercal \boldsymbol{M}_b^{FEM} \boldsymbol{u}_b(\boldsymbol{\Psi})$ are real, fully populated matrices.

The matrix $\boldsymbol{\Phi}^\intercal \boldsymbol{M}_b^{FEM} \boldsymbol{\Phi}$ is the identity matrix, since dynamic eigenmodes are orthogonal, and since the SDT normalizes dynamic eigenmodes to the mass matrix.

The building stiffness matrix $\boldsymbol{K_b}$

$$\boldsymbol{K}_b = \begin{bmatrix} \boldsymbol{u}_b(\boldsymbol{\Psi})^\intercal \boldsymbol{K}_b^{FEM} \boldsymbol{u}_b(\boldsymbol{\Psi}) & \boldsymbol{u}_b(\boldsymbol{\Psi})^\intercal \boldsymbol{K}_b^{FEM} \boldsymbol{\Phi} \\ \boldsymbol{\Phi}^\intercal \boldsymbol{K}_b^{FEM} \boldsymbol{u}_b(\boldsymbol{\Psi}) & \boldsymbol{\Phi}^\intercal \boldsymbol{K}_b^{FEM} \boldsymbol{\Phi} \end{bmatrix} \tag{6.7}$$

The matrix $\boldsymbol{u}_b(\boldsymbol{\Psi})^\intercal \boldsymbol{K}_b^{FEM} \boldsymbol{u}_b(\boldsymbol{\Psi})$ is a real, fully populated matrix.

The matrix $\boldsymbol{u}_b(\boldsymbol{\Phi})^\intercal \boldsymbol{K}_b^{FEM} \boldsymbol{\Psi}$ is vanishing. Indeed, the matrix $\boldsymbol{K}_b^{FEM} \boldsymbol{\Psi}$ corresponds to the forces applied on the building when displacements $\boldsymbol{\Psi}$ are imposed on the interface Σ_{bs}. On this interface, the displacements $\boldsymbol{\Phi}$ are vanishing.

The matrix $\boldsymbol{u}_b(\boldsymbol{\Psi})^\intercal \boldsymbol{K}_b^{FEM} \boldsymbol{\Phi}$ vanishes too due to symmetry.

The matrix $\boldsymbol{\Phi}^\intercal \boldsymbol{K}_b^{FEM} \boldsymbol{\Phi}$ is a diagonal matrix with elements ω_j^2, ω_j being the pulsation of the j-th eigenmode.

The building damping matrix $\boldsymbol{C_b}$

$$\boldsymbol{C}_b = \begin{bmatrix} 0 & 0 \\ 0 & \boldsymbol{C}_{bI} \end{bmatrix} \tag{6.8}$$

It is assumed that the modes $\boldsymbol{u}_b(\boldsymbol{\Psi})$ are not damped.

Modal damping is imposed on the modes $\boldsymbol{\Phi}$. $\boldsymbol{C}_{bI}$ thus is an imaginary diagonal matrix with elements $-2i\xi\omega_j$, with ω_j the pulsation of the j-th eigenmode. ξ is chosen 2%.

The forces induced by the incident field $\boldsymbol{F_s(\omega)}$

The induced forces $\boldsymbol{F}_s(\omega)$ can be computed following the method outlined in chapter 2. For their computation, the knowledge of the incident field for the building in the centers of gravity of the boundary element mesh of the interface Σ_{bs} is necessary.

The incident field for the building is the field radiated by the tunnel. It is assumed that the field radiated by the tunnel when forces are applied on the tunnel invert, can be computed neglecting the influence of the field diffracted by the building.

As outlined in chapter 2, a formulation for the total field is used to compute $\boldsymbol{F}_s(\omega)$. This method, writes the representation theorem for the interior soil domain (the excavated part of the soil) and for the exterior soil domain (the soil with excavation). As shown in chapter 2, the contributions of all boundaries in the equations disappear, except from the contribution of the soil-structure interface. A numerical computation requires a mesh of the whole soil-structure interface. The method thus doesn't fully hold, since only the sixteen foundation plates are taken into account instead of the whole interface.

6.2.3 The numerical implementation

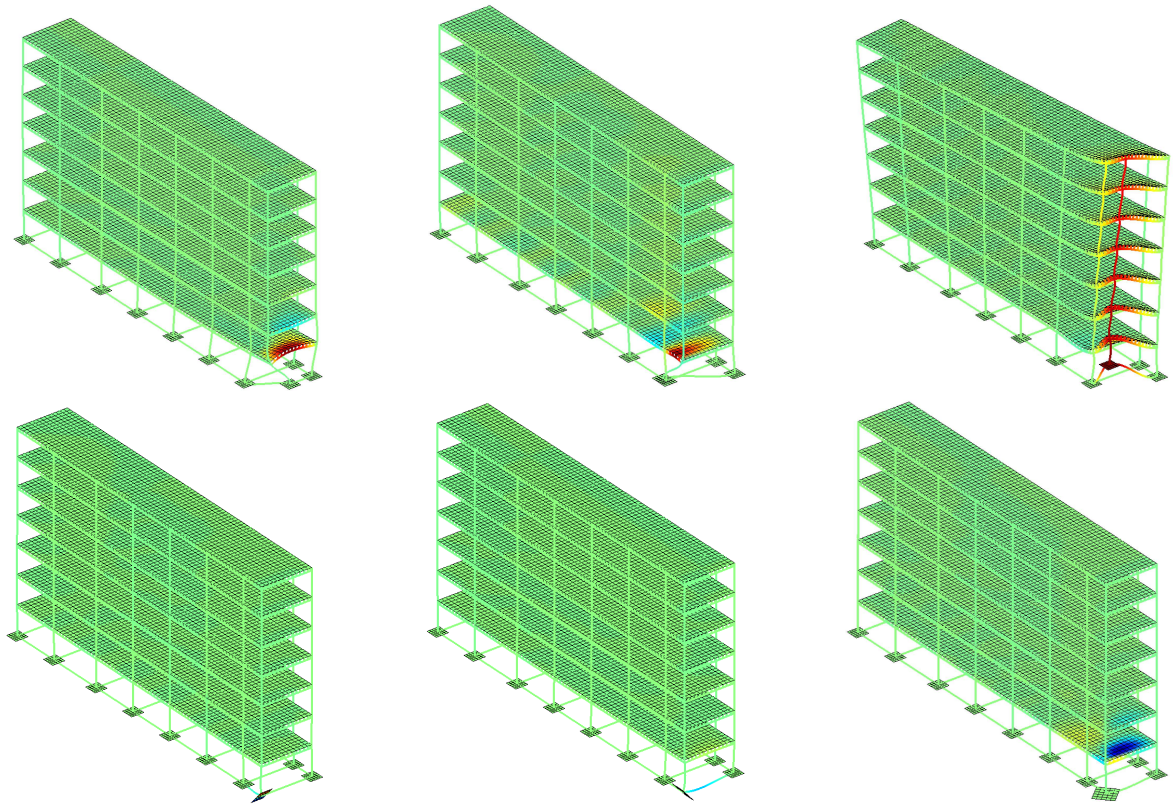

Figure 10: The 6 modes $\boldsymbol{u}_b(\boldsymbol{\Psi}_m)(\boldsymbol{x})$ corresponding to the 6 rigid body modes of the first foundation plate. The colors are relative to the vertical displacement component.

First, the kinematic basis of the building is computed. Following the previous paragraph, the computation of the fields $\boldsymbol{u}_b(\boldsymbol{\Psi}_m)(\boldsymbol{x})$ from the fields $\boldsymbol{\Psi}_m(\boldsymbol{x})$ is a classic, static FEM problem. The 6 $\boldsymbol{u}_b(\boldsymbol{\Psi}_m)(\boldsymbol{x})$ modes corresponding to the 6 rigid body modes of the first foundation plate $\boldsymbol{\Psi}_m(\boldsymbol{x})$ are shown in figure 10. Once computed, these fields $\boldsymbol{u}_b(\boldsymbol{\Psi}_m)(\boldsymbol{x})$ are normalized with respect to the mass matrix of the building.

Then, the set of modes $\boldsymbol{\Phi}_i(\boldsymbol{x})$ is added to the basis of modes $\boldsymbol{u}_b(\boldsymbol{\Psi}_m)(\boldsymbol{x})$. They are the dynamic eigenmodes resting on a fixed basis, in the frequency range of interest. Using the SDT

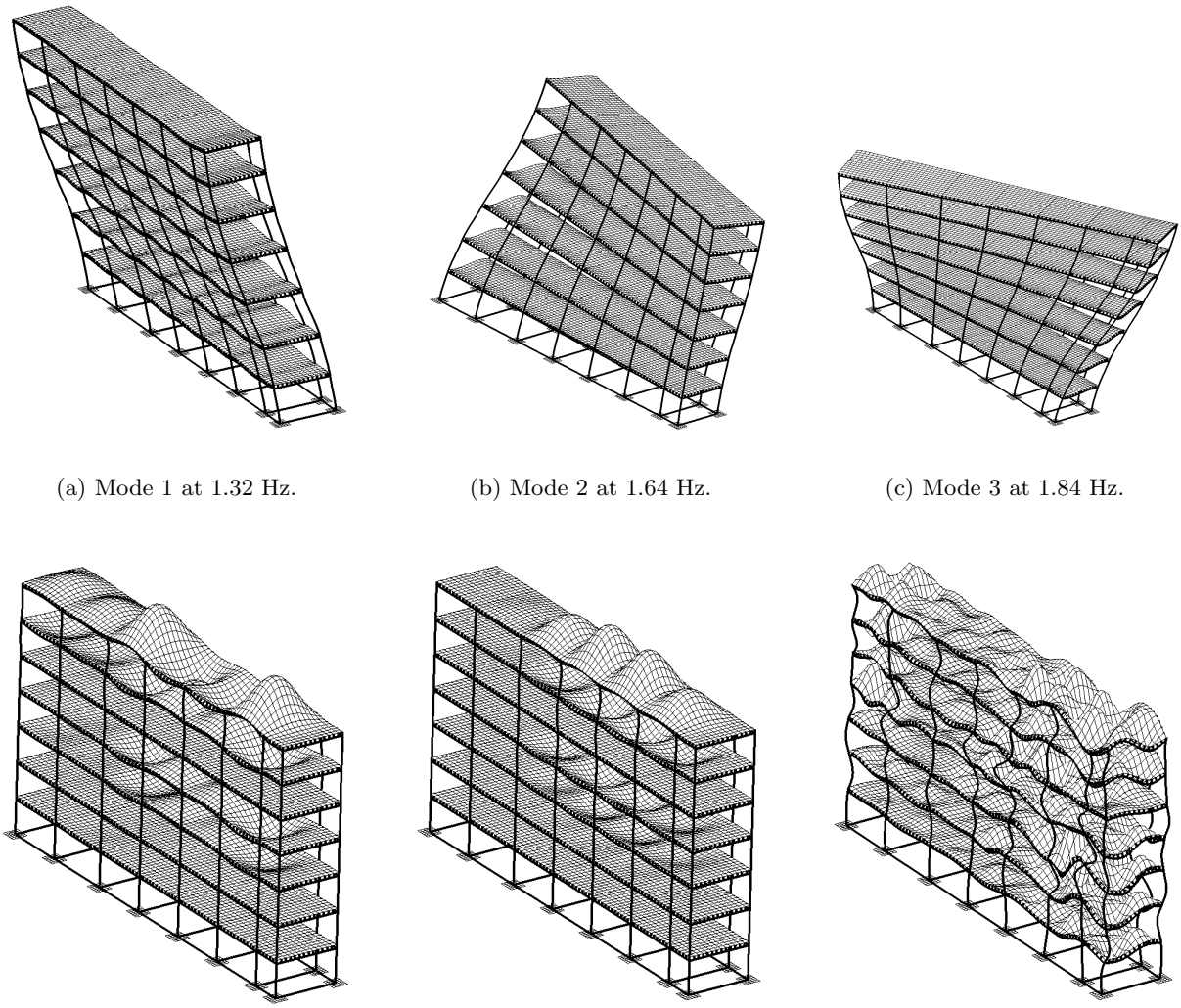

(a) Mode 1 at 1.32 Hz. (b) Mode 2 at 1.64 Hz. (c) Mode 3 at 1.84 Hz.

(d) Mode 35 at 14.85 Hz. (e) Mode 43 at 15.54 Hz. (f) Mode 535 at 83.25 Hz.

Figure 11: A few modes $\boldsymbol{\Phi}_i(\boldsymbol{x})$.

IRA/Sorensen solver, which is the appropriate method for large sparse matrices $\boldsymbol{K}_b^{FEM}$ and $\boldsymbol{M}_b^{FEM}$. A computation is performed for the 0-100 Hz range. In the 0-10 Hz range, modes of longitudinal bending (1-4th), of transverse bending (1-3th) and of torsion (1-3th) are found. From 10 to 100 Hz, higher order bending and torsion are found as well as a high density of plate bending modes. 750 modes are found in the 0-100 Hz range.

A more refined study of the eigenmodes in the range 0-12 Hz can be found in the work of Coster [13]. A few mode shapes on fixed basis are shown in figure 11. Figures 11a,11b and 11c show the first longitudinal bending, the first transversal bending, and the first torsion mode, respectively. Figures 11d, 11e and 11f show a few plate bending modes found at higher frequencies.

The next sections will study the building response in the 0-80 Hz range. The modal basis of 750 modes in the 0-100 Hz range thus might be too small to accurately model the highest frequencies.

To compute the forces $\boldsymbol{F}_s(\omega)$ induced by the incident field, the tunnel-soil-building interaction model is used to compute the displacement field radiated by the tunnel, in the centres of gravity of the elements of the building foundation. These centres of gravity do not have positions periodic with a periodicity length L in the direction $\boldsymbol{e}_2$. Therefore, the Floquet periodicity cannot be explicitly used and a separate computation is necessary for each centre of gravity.

A computation for the negative wavenumbers is necessary since the centres of gravity do not have positions symmetrical with respect to the x'-z'-plane.

The BEM mesh of the building foundation has 400 elements and the computation thus is very demanding in computer memory and computing time (MISS takes approximately 3 GB RAM and more than 60 minutes per frequency).

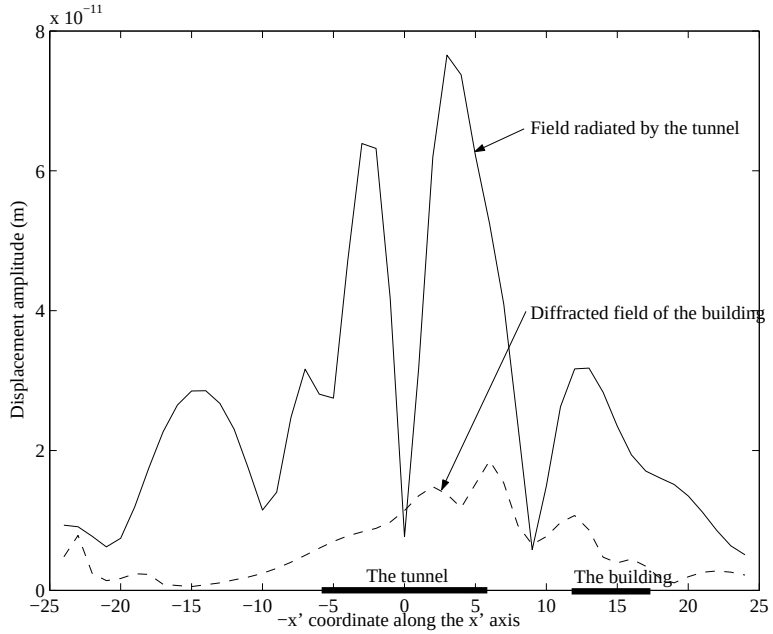

Figure 12: The amplitude of the vertical displacement component of the field radiated by the tunnel and of the field diffracted by the building at the free surface at 30 Hz.

The field radiated by the tunnel is computed neglecting the presence of the building. The foundation of the building, however, radiates a diffracted field, that consists of the locally diffracted

field and the radiated field. This field has been computed in the points of the free surface and compared to the field radiated by the tunnel (figure 12), leading to the conclusion that the latter is five times larger than the field diffracted by the building, confirming that the initial assumption is reasonable.

6.3 The building response on harmonic loads on the tunnel invert

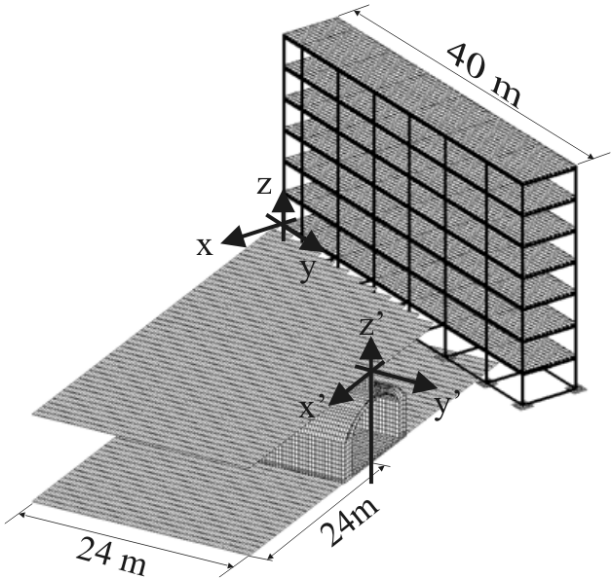

Figure 13: The visualisation model.

The harmonic response of the building on a force applied at a position (x',y',z')=(-2.5;0;-8.25) on the tunnel invert has been computed and animated. The visualization model is shown in figure 13. The same visualization surfaces for the soil are used as in chapter 5. On these surfaces, only the field radiated by the tunnel is shown. The model visualizes the beams, plates and foundation of the building. The constraints between the plates and the beams are visualized as beam elements too. The colours are relative to the vertical displacement component and all are equally scaled.

Figures 15 and 16 show the harmonic responses at 10 Hz and 20 Hz at the timesteps t=0 s, t=$T/8$, t=$T/4$ and t=$3T/8$, with T=1/10 s and T=1/20 s, respectively. At these low frequencies, the figures show that the longitudinal and transverse bending modes and the torsion modes of the building are excited.

The inclination of the building with respect to the tunnel axis causes the waves to arrive from the tunnel at the building at an important angle. This causes an important excitation of the torsion modes of the building at low frequencies with a maximum at 20 Hz as shown in figure 15.

As already mentioned, the only modelled contact between the building and the soil consists of the foundation of the building. The excavated part of the building thus can show large torsion or bending displacements without feeling any resistance from the surrounding soil. Their is no

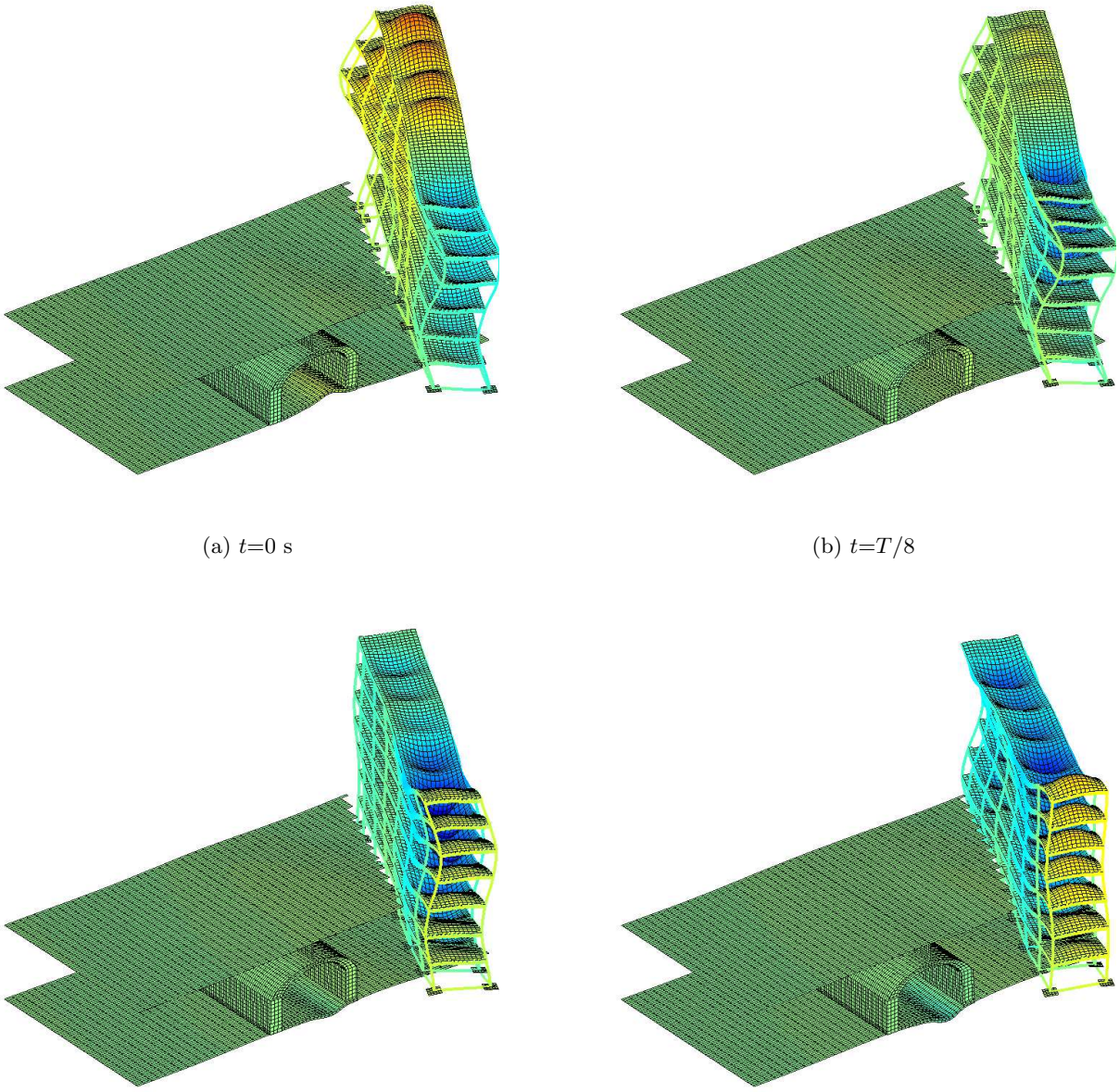

(a) t=0 s

(b) t=$T/8$

(c) t=$T/4$

(d) [t=$3T/8$

Figure 14: The harmonic response at 10 Hz at the timesteps t=0 s, t=$T/8$, t=$T/4$ and t=$3T/8$ with the period T=1/10 s.

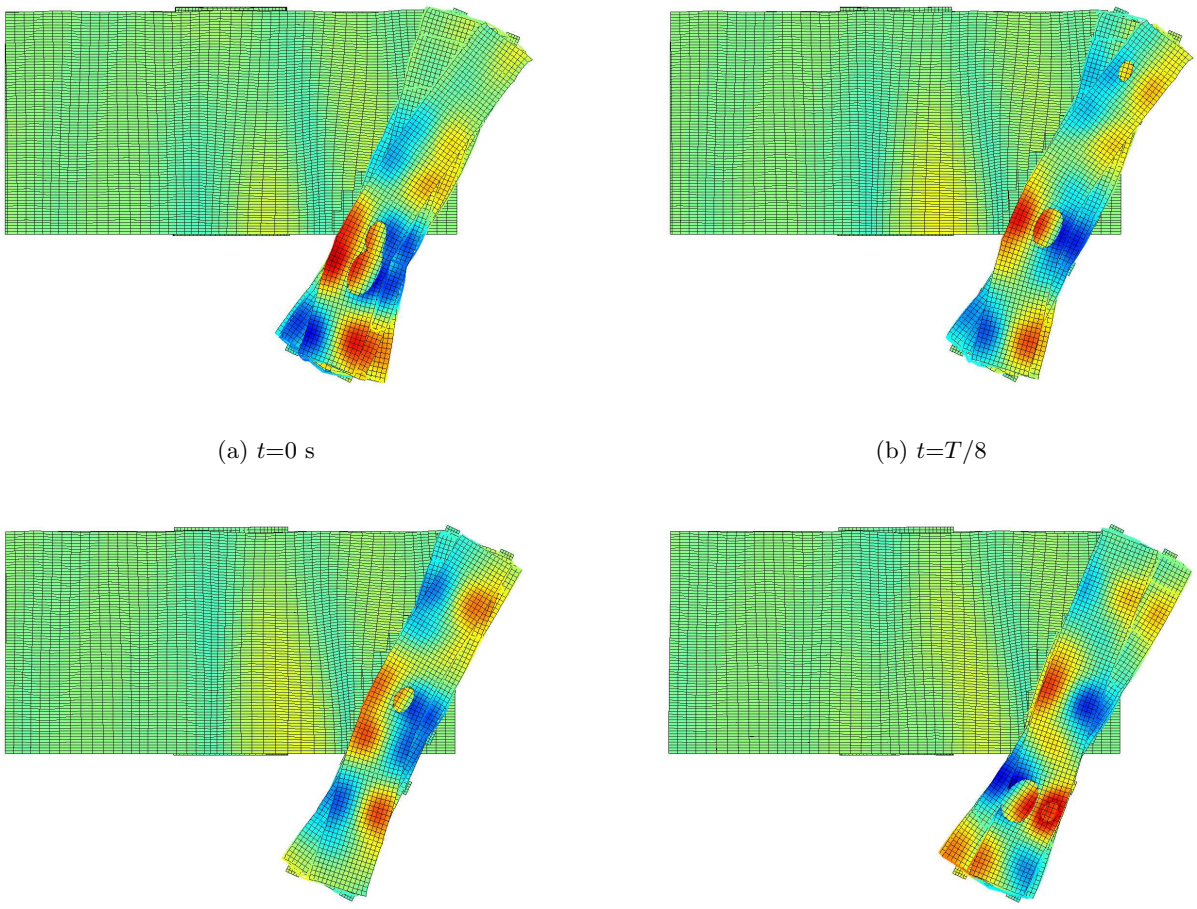

(a) t=0 s

(b) t=$T/8$

(c) t=$T/4$

(d) [t=$3T/8$

Figure 15: The harmonic response at 20 Hz at the timesteps t=0 s, t=$T/8$, t=$T/4$ and t=$3T/8$ with the period T=1/20 s.

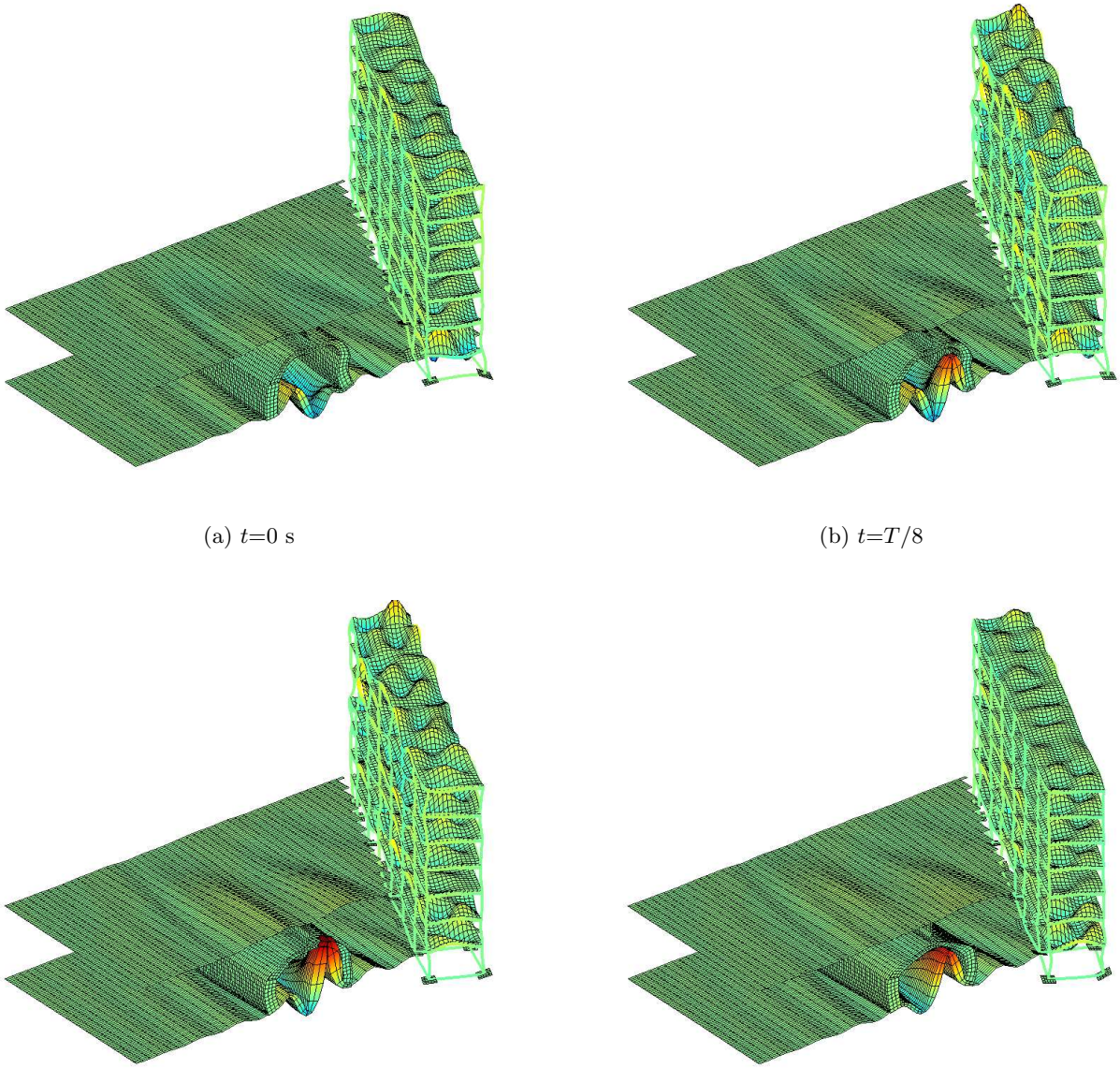

(a) t=0 s

(b) t=$T/8$

(c) t=$T/4$

(d) t=$3T/8$

Figure 16: The harmonic response at 60 Hz at the timesteps t=0 s, t=$T/8$, t=$T/4$ and t=$3T/8$ with the period T=1/60 s.

compatibility between the soil and building displacements at the free surface. This is clearly visible in figure 14.

At low frequencies, the wavelength in the soil is much larger than the transverse dimension of the building. At these frequencies, the translational degrees of freedom of the foundation plates are dominant.

Figure 16 shows the harmonic response at 60 Hz at the instances t=0 s, t=$T/8$, t=$T/4$ and t=$3T/8$, with T=1/60 s. At high frequencies, mainly the plate bending modes of the building are excited. At higher frequencies, higher plate bending modes are excited. The wavelength in the soil gets smaller than the transverse building dimension. At high frequencies, the rotational degrees of freedom of the foundation plates are dominant.

6.4 The transfer functions

Figure 17 shows the average of the vertical velocities in the middle of the transverse beams of the first and the sixth floor, the average of the vertical velocities in the middle of the plates at the first and the sixth floor, as well as the vertical velocity of the field radiated by the tunnel in a point under the building with coordinates (-13,0,-3.235). The velocities are analysed since they are important in a later study of the re-radiated noise. The unity dB is used ((20/log(10))*log(v/v_{ref})) with $v_{ref} = 1$.

At low frequencies (0-10 Hz), the longitudinal and transverse bending and the torsion are excited. The beams and the plates have similar velocities.

At approximately 10 Hz the plate bending modes become important and at around 15-20 Hz, a huge plate bending resonance shows up.

At the frequencies from 20 to 30 Hz, a range of low velocities for plates and beams at the first floor, corresponding to a decrease of the velocity of the radiated field of the tunnel.

At high frequencies, the velocities in the building are smaller than the velocity of the radiated field of the tunnel. A possible reason is that the radiated field of the tunnel mostly excites the rotation of the foundation plates at these frequencies. Those rotations cause bending and torsion in the columns of the basement, but do not cause important displacements in the building.

Figure 18 is similar to figure 17, but shows accelerations. At low frequencies, the plate resonance around 15-20 Hz is again found, together with a range of smaller accelerations between 20 and 30 Hz. The radiated field of the tunnel has smaller accelerations in this range. Only the first floor shows similar, small accelerations in this range too. The accelerations at the sixth floor are larger.

At high frequencies, the accelerations in the building are again smaller than the accelerations of the radiated field of the tunnel.

Finally, figure 19 makes a first comparison of the results of the numerical model with the measurement data. The comparison is made for channel F501z of event Mex06-1, for hammer impact analysis [21]. The measured acceleration is divided by the measured force in order to compare the transfer functions.

The amplitudes at low frequencies seem to correspond. The peak at around 15-20 Hz is found back, but not in the 10-15 range. The range of lower accelerations after this peak is also retrieved.

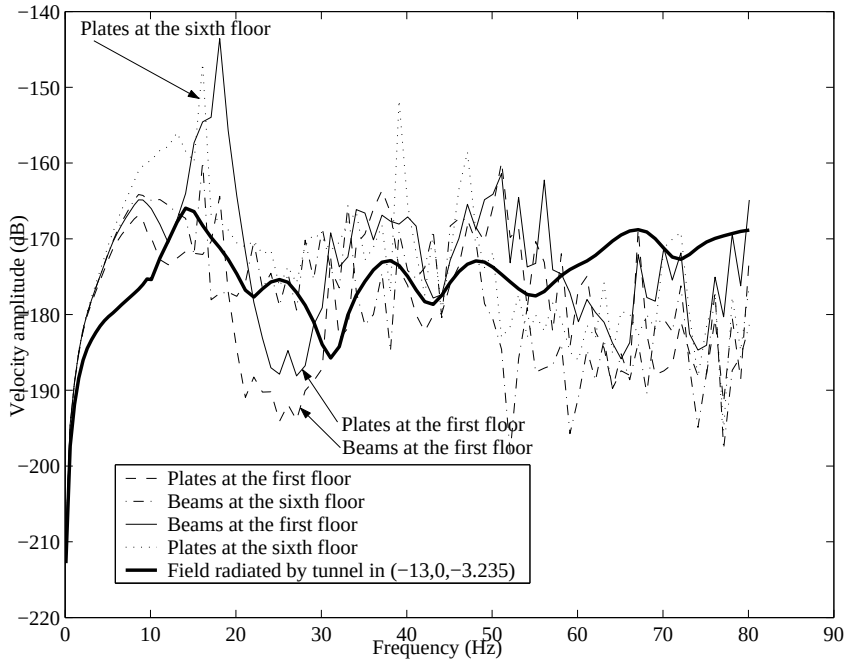

Figure 17: The amplitude of the vertical velocities at the middle of transverse beams and plates at the first and the sixth floor, as well as the amplitude of the vertical velocity component of the field radiated by the tunnel.

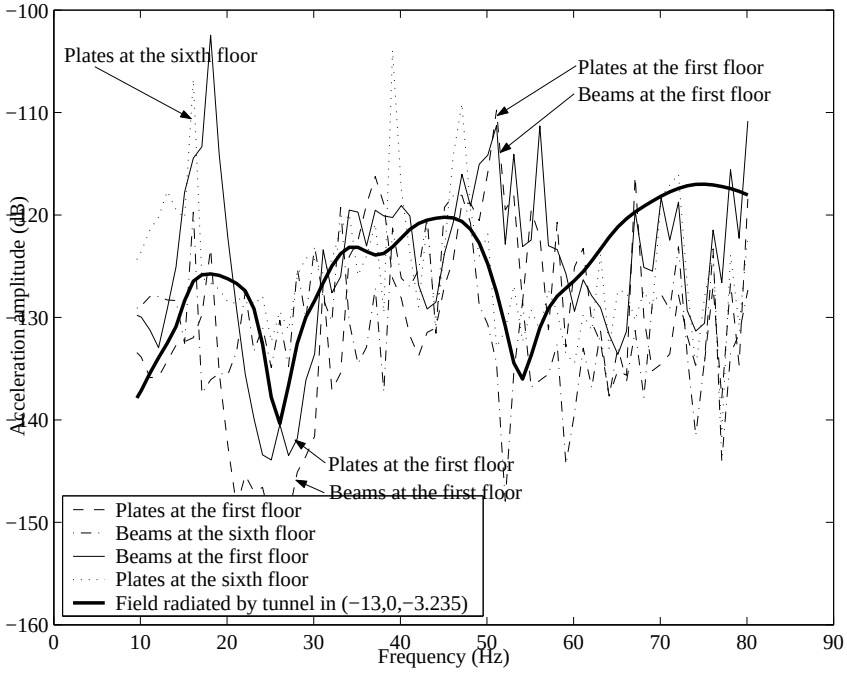

Figure 18: The amplitude of the vertical accelerations at the middle of transverse beams and plates at the first and the sixth floor, as well as the amplitude of the vertical acceleration component of the field radiated by the tunnel.

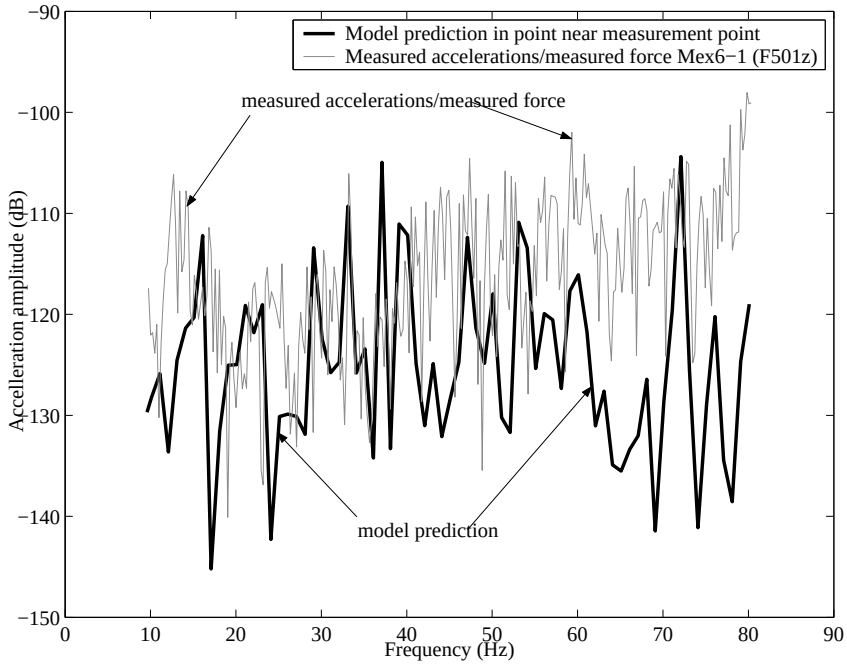

Figure 19: A comparison of the predicted vertical acceleration amplitudes with the measured acceleration amplitudes divided by the measured force in point F501z event m06-1.

At high frequencies, the predicted vertical acceleration amplitudes are smaller than the measured values. This can be due to the fact that the measured data correspond to the impact on the rail track, whereas the predicted values are for a force on the tunnel invert. In the report on the modelling of the track and ballast on the tunnel invert [22], it is found that the track receptance (track displacement divided by applied force) has an important maximum at these high frequencies. This maximum corresponds to the uncoupling of the track on the ballast stiffness. The rail and the sleepers vibrate in phase. In the near future, the track and ballast will be included in the tunnel-soil model. The influence of this maximum can then be studied. Another reason might be a too small modal basis at the highest frequencies.

6.5 Conclusion and further development

In this chapter, a method has been proposed to couple the 3D tunnel-soil interaction model to a 3D soil-building interaction model. The displacement field radiated by the tunnel has been computed without the presence of the building in the model and this radiated field has been used as the incident field for the building.

The soil-building interaction model has been elaborated: a kinematic basis has been proposed and the corresponding variational formulation has been derived.

The presented method has been implemented using the combined programs MISS (BEM) and SDT (FEM). First results have been obtained and few problems have been identified. In the future, the model has to be further developed to improve an already good computation-measurements correlation.

The two major uncertainties encountered in the modelling were about the foundation of the building and about its actual position. In this work, a designed foundation has been assumed and an approximate position of the building with respect to the tunnel has been used. An accurate modelling of the foundation is essential.

The only contact modelled between the soil and the building in the soil-building interaction model, consisted of the building foundation. It has been shown that, at low frequencies, the torsion and the longitudinal and transverse bending are important. As a result, however, the basement can have large displacements uncoupled from the surrounding soil. A solution could consist in including the basement walls in the model and to model a contact between soil and basement walls too. This would also solve the problem of the total field formulation. This solution would however drastically increase the number of points in which the incident field has to be computed and for which the radiated field of the tunnel-soil model thus has to be computed. It is this last computation that is the time and memory demanding part of the computation.

A further development of the building model is necessary. The two small buildings built aside of the main building can be included in the model, as can the walls and stair cases. Including these components will stiffen the building, certainly regarding the torsion and bending modes. Including the walls without coupling them to the soil might even be a sufficient solution for the problem in the previous paragraph.

It has been noted too that the modal basis in the present model probably is not sufficiently large to accurately model the high frequency range. However, 750 modes have been found already between 0 and 100 Hz. A memory of about 1 GB RAM was required to compute this basis.

Significantly detailing the model and thus increasing the number of dofs, combined with a larger modal basis, could however cause serious memory problems regarding the computation of the modes.

The present analysis only consists in the response on harmonic loads on the tunnel invert. An analysis with transient loads can be done. A very fine sampling interval in the frequency domain is necessary due to the heavily oscillating behaviour of the tunnel-soil-building transfer function.

The Convurt consortium will most probably organize a second measurement campaign in the "Maison du Mexique". Further analysis of the developed prediction model will be a very useful source of information for this campaign.

Appendix A

Matlab and MISS input files: the harmonic response of the tunnel-soil-system

Relevant files: createnmodel2.m, createtrans.m, MVFDreadc.m, postanimation.m, postcontrolfigure.m, postcalc5.m, postkselements.m, postmaster3.m, readTOT.m, TOTread.m; ctvar.mat, volmesh.mat; MISS.IN, cititunnel.chp, cititunnel.miss;animationfreq.mat, runanifreq.m; anifreq14hz.avi, ani80hza.avi, ani80hzb.avi, ani80hzc.avi, ani80hz.gif

A.1 The problem characteristics

- $NBFEMelts$: Number of elements of the finite element mesh of the tunnel generic cell.
- $NBFEMnodets$: Number of nodes of the finite element mesh of the tunnel generic cell.
- $NBFEMgroupts$: Number of groups of elements of the finite element mesh of the tunnel generic cell.
- $NBBEMelts$: Number of elements of the boundary element mesh of interface between the soil and the tunnel generic cell.
- $NBDOFts$: Number of degrees of freedom in each node of the mesh of the tunnel generic cell.
- $NBMODEts$: Number of dynamic eigenmodes of the tunnel generic cell.
- $NBFREQts$: Number of frequencies computed for.
- $NBSLOWts$: Number of positive slowness/wave numbers computed for.
- $NBCTRts$: Number of control points in the generic soil cell.
- $NBCELLSts$: Number of repeated cells to compute the Floquet inverse transform for.

A.2 The Matlab pre-processing results files

ctvar.mat

- Description: contains the mass and stiffness matrice $\boldsymbol{m}$ and $\boldsymbol{k}$ of the generic cell of the tunnel, as well as its degrees of freedom $\boldsymbol{mdof}$ and eigenmodes $\boldsymbol{phi}$ with corresponding frequencies $\boldsymbol{wj}$.
- The matrices:

  $\boldsymbol{m} \in \mathcal{M}(NBFEMnodets * NBDOFts, NBFEMnodets * NBDOFts)$

  $\boldsymbol{k} \in \mathcal{M}(NBFEMnodets * NBDOFts, NBFEMnodets * NBDOFts)$

  $\boldsymbol{mdof} \in \mathcal{M}(NBFEMnodets * NBDOFts, 1)$

  $\boldsymbol{phi} \in \mathcal{M}(NBFEMnodets * NBDOFts, NBmodets)$

  $\boldsymbol{wj} \in \mathcal{M}(NBMODEts, 1)$

volmesh.mat

- Description: contains the finite element mesh of the generic cell of the tunnel $\boldsymbol{FEnode}$ and $\boldsymbol{FEelt}$.
- The matrices:

  $\boldsymbol{FEnode} \in \mathcal{M}(NBFEMnodets, 7)$

  $\boldsymbol{FEelt} \in \mathcal{M}(NBFEMelts + NBFEMgroupts, 10)$

A.3 The MISS processing

A.3.1 Description

The MISS3D program is used to compute the periodic BEM problems. It computes the dynamic soil stiffness matrix and the radiated fields in the control points.

A.3.2 The MISS input files

MISS.IN

- Description: MISS main input file containing the commands to be executed and the problem description.

cititunnel.miss

- Description: the boundary element mesh.

cititunnel.chp

- Description: the modes imposed on the boundary element mesh.

A.3.3 The MISS program

miss3d.x

- Description: Miss3d.x running on Unix, Linux and MacOSX platforms.

A.3.4 The MISS output files

cititunnel.01.IMPDC

- Description: the soil impedance matrix.

cititunnel.01.CTR

- Description: the locally diffracted field (if any), and the radiated fields in the control points.

A.4 The Matlab-SDT post processing

A.4.1 Description

The MISS results are imported in the Matlab environment and post processed using Matlab and SDT routines.

A.4.2 The MISS-Matlab coupling routines

MVFDreadc.m

- Description: reads MISS output file .IMPDC (can also read .FS).

TOTread.m, READTOT.m

- Description: read MISS output file .CTR.

A.4.3 The post processing routines

postmaster3.m

- Description: the main post processing file. The characteristics of the problem are specified in this file. Running it from the Matlab prompt then invokes the other routines.

postcalc5.m

- Description: the main computation file. The routine reads the pre-processing and processing results files, assembles and solves the system of equations, and computes the necessary Floquet inverse transformations.
- Input files: cititunnel.miss, cititunnel.chp, ctvar.mat, volmesh.mat and b.mat containing the applied force $\boldsymbol{b}$.
- Output files: ks.mat containing the soil stiffness matrix $\boldsymbol{ks}$, uc.mat containing the radiated fields in the control points $\boldsymbol{uc}$, def.mat containing the displacements of the generic cell in the frequency-slowness/wave number domain $\boldsymbol{def}$, ut.mat containing the displacements in the control points of the generic cell in the frequency-slowness/wave number domain $\boldsymbol{ut}$, and transfer.mat containing the displacements of the tunnel nodes of the repeated cells in the frequency domain $\boldsymbol{deftt}$ and the displacements in the control points of the repeated cells in the frequency domain $\boldsymbol{uttt}$ and the frequency range $\boldsymbol{w}$.

- The matrices:
  $\boldsymbol{b} \in \mathcal{M}(NBDOFts * NBFEMnodets, 1)$
  $\boldsymbol{ks} \in \mathcal{M}(NBMODEts, NBMODEts, NBSLOWts, NBFREQts)$
  $\boldsymbol{uc} \in \mathcal{M}(3, NBCTRts, NBMODEts, NBSLOWts, NBFREQts)$
  $\boldsymbol{def} \in \mathcal{M}(NBDOFts * NBFEMnodets, 2 * NBSLOWts - 1, NBFREQts)$
  $\boldsymbol{ut} \in \mathcal{M}(3, NBCTRts, 2 * NBSLOWts - 1, NBFREQts)$
  $\boldsymbol{deftt} \in \mathcal{M}(NBDOFts * NBFEMnodets, NBFREQts, NBCELLSts)$
  $\boldsymbol{uttt} \in \mathcal{M}(3, NBCTRts, NBFREQts, NBCELLSts)$
  $\boldsymbol{w} \in \mathcal{M}(1, NBFREQts)$

postanimation.m

- Description: output to an animation of the harmonic response.
- Input files: transfer.mat
- Output files: animationfreq.mat containing the mesh of the repeated visualization model $\boldsymbol{FEnode}$ and $\boldsymbol{FEelt}$, the corresponding degrees of freedom $\boldsymbol{mdof}$, the corresponding displacements $\boldsymbol{defttt}$, and the frequency range $\boldsymbol{w}$.
- The matrices:
  $\boldsymbol{FEnode} \in \mathcal{M}(NBFEMelts * (NBCELLS/2 + 1) + NBCTRts * NBCELLS, 7)$
  $\boldsymbol{mdof} \in \mathcal{M}(NBFEMnodets * (NBCELLS/2 + 1) * NBDOFts + NBCTRts * NBCELLS * 3, 1)$
  $\boldsymbol{defttt} \in \mathcal{M}(NBFEMnodets * (NBCELLS/2 + 1) * NBDOFts + NBCTRts * NBCELLS * 3, NBFREQts)$

createnmodel2.m, createtrans.m, postcontrolfigure.m, postkselements.m

- Description: small scripts called by postmaster3.m, postcalc5.m and postanimation.m.

A.5 The Animations

animationfreq.mat and runanifreq.m

- Description: the animation of the harmonic tunnel-soil response presented in chapter 5. Executing the Matlab routine loads the animationfreq.mat file and calls SDT-routines for the animation.

anifreq14hz.avi

- Description: the animation of the harmonic tunnel-soil response at 14 Hz.

anifreq80hza.avi

- Description: the animation of the harmonic tunnel-soil response at 80 Hz.

anifreq80hzb.avi

- Description: the animation of the harmonic tunnel-soil response at 80 Hz. Only upper tunnel parts are shown. All colors are equally scaled.

anifreq80hzc.avi

- Description: the animation of the harmonic tunnel-soil response at 80 Hz. Only visualization surface 2 is shown. All colours are equally scaled.

Appendix B

Matlab and MISS input files: the transient response of the tunnel-soil-system

Relevant files: animationtime.m, createhammer.m; animationtime.mat, runanitime.m; anitime.avi

B.1 The problem characteristics

- $NBFEMelts$: Number of elements of the finite element mesh of the tunnel generic cell.
- $NBFEMnodets$: Number of nodes of the finite element mesh of the tunnel generic cell.
- $NBDOFts$: Number of degrees of freedom in each node of the tunnel generic cell.
- $NBCTRts$: Number of control points in the generic soil cell.
- $NBCELLSts$: Number of repeated cells to compute the Floquet inverse transform for.
- $NBFREQts$: Number of positive frequencies computed for.
- $NBTIMEts$: Number of time samples saved to disk.

B.2 The pre-processing

The transfer functions to all points of the visualization model are computed using the routines described in the previous appendix.

B.3 The processing

B.3.1 Description

The transfer functions are multiplied with the force in the frequency domain, and an inverse Fourier transformation then leads to the transient response in the time domain.

B.3.2 The processing files

createhammer5.m

- Description: computes the Gaussian transient force in the frequency and time domain.
- Output files: b.mat containing the transient force in the frequency domain $\boldsymbol{b}$.
- The matrices:

  $\boldsymbol{b} \in \mathcal{M}(1, 2 * (NBFREQts - 1))$

animationtime2.m

- Description: reads the transfer functions, multiplies them with the force, computes the inverse Fourier transform. The output is the transient animation in the time domain.
- Input files: transfer.mat, b.mat.
- Output files: animationtime.mat containing the mesh of the repeated visualization model $\boldsymbol{FEnode}$ and $\boldsymbol{FEelt}$, the corresponding degrees of freedom $\boldsymbol{mdof}$, the corresponding displacements $\boldsymbol{deftt}$ and the times at the time samples saved to disk $\boldsymbol{time}$.
- The matrices:

  $\boldsymbol{FEnode} \in \mathcal{M}(NBFEMnodets * (NBCELLS/2 + 1) + NBCTRts * NBCELLS, 7)$

  $\boldsymbol{mdof} \in \mathcal{M}(NBFEMnodets * (NBCELLS/2 + 1) * NBDOFts + NBCTRts * NBCELLS * 3, 1)$

  $\boldsymbol{deftt} \in \mathcal{M}(NBFEMnodets * (NBCELLS/2 + 1) * NBDOFts + NBCTRts * NBCELLS * 3, NBTIMEts)$

  $\boldsymbol{time} \in \mathcal{M}(1, NBTIMEts)$

B.4 The animations

animationtime.mat and runanitime.m

- Description: the animation of the transient tunnel-soil response presented in chapter 5. Executing the Matlab routine loads the animationtime.mat file and calls SDT-routines for the animation.

anitime.avi

- Description: the animation of the transient tunnel-soil response.

Appendix C

Matlab and MISS input files: the harmonic response of the tunnel-soil-building system

Relevant input files: createmaison3.m, createmaison4.m, file.RST, createBEM.m, createcontrpos.m, createpsimodessoil.m; MISS.IN, cititunnel.miss, cititunnel.chp, createUI.m, UIwrite.m; createpsimodesrigid.m, normalizepsimodesrigid.m, createphimodes.m, createMISSfiles.m; MISS.IN, mexique.miss, mexique.chp, mexique.UI; assembleandsolverigid.m, createfullmodelrigid.m

Relevant results files: resmaison.mat, BEMmesh.mat, BEMgravpos.mat, psimodesBEM.mat; mexique.UI, normPSImodes.mat, modesphi.mat, mexique.miss, mexique.chp; mexique.01.IMPDC, mexique.01.CTR, mexique.01.FS; u.mat, animationhouse.mat

C.1 The problem characteristics

- $NBFREQbs$: Number of frequencies computed for.
- $NBFEMeltbs$: Number of elements of the finite element mesh of the building.
- $NBFEMnodebs$: Number of nodes of the finite element mesh of the building.
- $NBFEMnodebs$: Number of groups of elements of the finite element mesh of the building.
- $NBFEMMDOFbs$: Total number of dofs of the finite element mesh of the building.
- $NBFEMCDOFbs$: Reduced number of dofs of the finite element mesh of the building, after applying the rigid constraints.
- $NBBEMeltbs$: Number of elements of the boundary element mesh of the soil-building-interface.
- $NBBEMnodebs$: Number of nodes of the boundary element mesh of the soil-building-interface.

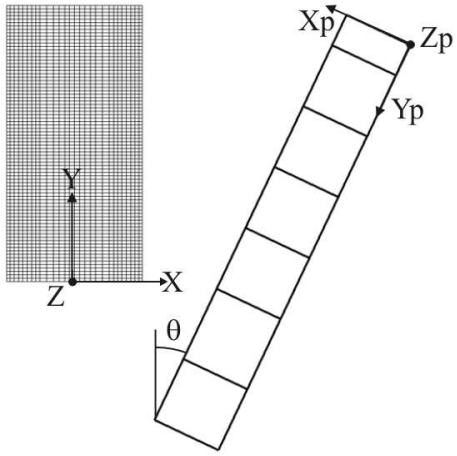

Figure 1: The position of the building with respect to the tunnel. Used axes in the computation.

- *NBpsimodebs*: Number of modes with a non-vanishing trace on the soil-building-interface.
- *NBphimodebs*: Number of modes with a vanishing trace on the soil-building-interface.
- *NBFEMeltbst*: Number of elements of the finite element mesh of the soil-tunnel-building visualization model.
- *NBFEMnodebst*: Number of nodes of the finite element mesh of the soil-tunnel-building visualization model.
- *NBFEMmdofbst*: Number of degrees of freedom of the finite element mesh of the soil-tunnel-building visualization model.

C.2 The Matlab and MISS pre-processing

C.2.1 Description

The position of the building and the tunnel are shown in figure 1, as well as the used axis frames. The used axis frames in the computation differ from those used in the report.

First, the building model is constructed in the Matlab-SDT environment. Then, the mass and stiffness matrix of the building are computed, as well as the basis of modes. At last, the modes on the BEMmesh of the foundation are determined and the necessary MISS input files are written.

C.2.2 The construction of the building model

createmaison3.m and createmaison4.m

- Description: loads the ansys model into the SDT, adds CELAS constraint equations (later manually changed to RIGID constraint equations, introducing matrices $\boldsymbol{T}$ and $\boldsymbol{cdof}$ and computes the mass and stiffness matrices $\boldsymbol{m}$ and $\boldsymbol{k}$.
- Input files: file.rst (the ansys building mesh)

- Output files: resmaison.mat containing the mesh of the building model $\boldsymbol{FEnode}$ and $\boldsymbol{FEelt}$, the transformation matrix of the rigid elements $\boldsymbol{T}$, the degrees of freedom after applying the rigid constraints $\boldsymbol{cdof}$, all degrees of freedom $\boldsymbol{mdof}$, and the mass and stiffness matrices $\boldsymbol{m}$ and $\boldsymbol{k}$.
- The matrices:

  $\boldsymbol{FEnode} \in \mathcal{M}(NBFEMnodebs, 7)$

  $\boldsymbol{FEelt} \in \mathcal{M}(NBFEMeltbs + NBFEMgroupbs, 7)$

  $\boldsymbol{mdof} \in \mathcal{M}(NBFEMMDOFbs, 1)$

  $\boldsymbol{cdof} \in \mathcal{M}(NBFEMCDOFbs, 1)$

  $\boldsymbol{T} \in \mathcal{M}(NBFEMMDOFbs, NBFEMCDOFbs)$

  $\boldsymbol{m} \in \mathcal{M}(NBFEMMDOFbs, NBFEMMDOFbs)$

  $\boldsymbol{k} \in \mathcal{M}(NBFEMMDOFbs, NBFEMMDOFbs)$

createBEM.m, createcontrpos.m

- Description: compute the finite element mesh of the foundation. The BEM mesh of the soil-building interface is equal to this FEM mesh. The centers of gravity of the elements of this mesh are also computed.
- Input files: resmaison.mat
- Output files: BEMmesh.mat containing the finite element mesh of the foundation $\boldsymbol{FEnodexpyp}$ (in the building local reference frame), $\boldsymbol{FEnodexy}$ (in the global axis frame) and $\boldsymbol{FEeltxy}$. BEMgravpos.mat containing the position of the centers of gravity of the elements of the mesh, $\boldsymbol{gravposxpyp}$ (in the building local reference frame) and $\boldsymbol{gravposxy}$ (in the global reference frame).
- The matrices:

  $\boldsymbol{FEnodexpyp} \in \mathcal{M}(NBBEMnodebs, 7)$

  $\boldsymbol{FEnodexy} \in \mathcal{M}(NBBEMnodebs, 7)$

  $\boldsymbol{FEeltxy} \in \mathcal{M}(NBBEMeltbs + 1, 10)$

  $\boldsymbol{gravposxpyp} \in \mathcal{M}(NBBEMeltbs, 3)$

  $\boldsymbol{gravposxy} \in \mathcal{M}(NBBEMeltbs, 3)$

createpsimodessoil.m

- Description: the modes $\boldsymbol{\Psi}_m(\boldsymbol{x})$ defined on the boundary element mesh are computed as proposed in 6.2.1 . A first order approximation of the rotations is made.
- Input files: BEMmesh.mat
- Output files: PSImodesBEM.mat containing the modes PSImodesBEM
- The matrices:

  $\boldsymbol{PSImodesBEM} \in \mathcal{M}(NBBEMnodebs * 3, NBpsimodebs)$

createUI.m

- Description: the tunnel-soil interaction model is used to compute the displacements in the centers of gravity of the foundation elements, due to an excitation on the tunnel invert.

- Input files and used files: MISS.IN, cititunnel.miss, cititunnel.chp, volmesh.mat, ct-var.mat, cititunnel.01.IMPC, cititunnel.01.CTR, postmaster3.m, postcalc5.m, UIwrite.m.
- Output files: mexique.UI containing the displacements in the centers of gravity $\boldsymbol{UI}$ in binary Big Endian 64-bit long data type; and animationfreqgr.mat containing an animation of the harmonic tunnel-soil response.
- The matrices:

  $\boldsymbol{UI} \in \mathcal{M}(3, NBBEMelts, 1, 1, NBFREQbs)$

createpsimodesrigid.m

- Description: the modes $\boldsymbol{u}_b(\boldsymbol{\Psi}_m)(\boldsymbol{x})$ defined on the building finite element mesh corresponding to the modes $\boldsymbol{\Psi}_m(\boldsymbol{x})$ defined on the building foundation are computed.
- Input files: resmaison.mat
- Output files: PSImaison.mat containing the modes $\boldsymbol{psimodes}$.
- The matrices:

  $\boldsymbol{psimodes} \in \mathcal{M}(NBFEMMDOFbs, NBpsimodebs)$

normalizepsimodesrigid.m

- Description: the modes $\boldsymbol{u}_b(\boldsymbol{\Psi}_m)(\boldsymbol{x})$ defined on the building finite element mesh and the corresponding modes $\boldsymbol{\Psi}_m(\boldsymbol{x})$ defined on the building foundation are normalized to the building mass matrix.
- Input files: resmaison.mat, PSImaison.mat, PSImodesBEM.mat
- Output files: normpsimodes.mat containing the modes $\boldsymbol{psimodesnorm}$ defined on the building finite element mesh and the modes $\boldsymbol{psimodesBEMnorm}$ defined on the building foundation.
- The matrices:

  $\boldsymbol{psimodesnorm} \in \mathcal{M}(NBFEMMDOFbs, NBpsimodebs)$

  $\boldsymbol{psimodesBEMnorm} \in \mathcal{M}(NBBEMnodebs * 3, NBpsimodebs)$

createphimodes.m

- Description: the fields $\boldsymbol{\Phi}_i(\boldsymbol{x})$ are added to the basis of modes $\boldsymbol{u}_b(\boldsymbol{\Psi}_m)(\boldsymbol{x})$.
- Input files: resmaison.mat
- Output files: modesphi.mat containing the modes $\boldsymbol{phi}$, the corresponding frequencies $\boldsymbol{wi}$ and $\boldsymbol{mdofphi}$ containing all degrees of freedom of the building.
- The matrices:

  $\boldsymbol{phi} \in \mathcal{M}(NBFEMMDOFbs, NBphimodebs)$

  $\boldsymbol{wi} \in \mathcal{M}(NBphimodebs, 1)$

  $\boldsymbol{mdofphi} \in \mathcal{M}(NBFEMMDOFbs, 1)$

createMISSfiles.m

- Description: the files necessary for the MISS computation of the soil-building-interaction problem are written.
- Input files and used files: BEMmesh.mat, normPSImodes.mat, miswrite.m
- Output files: mexique.miss containing the boundary element mesh, mexique.chp containing the non-vanishing modes defined on the building foundation.

C.3 The MISS processing

C.3.1 Description

The MISS3D program is used to compute the BEM problems. It computes the dynamic soil stiffness matrix, the radiated fields in the control points, and the locally diffracted field in the control points.

C.3.2 The MISS input files

MISS.IN, mexique.miss, mexique.chp, mexique.UI

C.3.3 The MISS program

miss3d.x

C.3.4 The MISS output files

mexique.01.IMPDC

- Description: the soil impedance matrix.

mexique.01.CTR

- Description: the locally diffracted field and the radiated fields in the control points.

mexique.01.FS

- Description: the force induced on the foundation by the incident field.

C.4 The Matlab postprocessing

assembleandsolverigid.m

- Description: the soil-structure interaction system described in section 6.2.2 is assembled and solved. The displacements of the foundation, of the building and of the control points are computed and saved in u.mat.
- Input files: resmaison.mat, modesphi.mat, normPSImodes.mat, mexique.01.IMPDC, mexique.01.CTR, mexique.01.FS.
- Output files: u.mat containing the displacements $\boldsymbol{u}$ defined on the building finite element mesh, and $\boldsymbol{ufond}$ defined on the building foundation.
- The matrices:

  $\boldsymbol{u} \in \mathcal{M}(NBFEMMDOFbs, NBFREQbs)$

  $\boldsymbol{ufond} \in \mathcal{M}(NBBEMeltbs * 3, NBFREQbs)$

createfullmodelrigid.m

- Description: output to an animation of the harmonic tunnel-soil-building response.

- Input files: animationfreqgr.mat, resmaison.mat, BEMmesh.mat, u.mat.
- Output files: fulmodelrigid.mat containing the finite element mesh of the full visualization model described in chapter 6 $\boldsymbol{FEelt}$ and $\boldsymbol{FEnode}$; animationhouse.mat containing the finite element mesh $\boldsymbol{FEelt}$ and $\boldsymbol{FEnode}$, the corresponding degrees of freedom $\boldsymbol{mdof}$, the corresponding displacements $\boldsymbol{deftt}$, and the frequencies $\boldsymbol{freq}$.
- The matrices:

  $\boldsymbol{FEelt} \in \mathcal{M}(NBFEMeltbst, 10)$

  $\boldsymbol{FEnode} \in \mathcal{M}(NBFEMnodebst, 7)$

  $\boldsymbol{mdof} \in \mathcal{M}(NBFEMmdofbst, 1)$

  $\boldsymbol{deftt} \in \mathcal{M}(NBFEMmdofbst, NBFREQbs)$

  $\boldsymbol{freq} \in \mathcal{M}(1, NBFREQbs)$

Bibliography

[1] J.D. Achenbach. *Wave propagation in elastic solids*. North-Holland publishing company, 1973.

[2] K. Aki and P.G. Richards. *Quantitative seismology - theory and methods*. W.H Freeman and Company, 1980.

[3] T.M. Al-Hussaini. Numerical modelling of ground vibrations caused by impulse loads on tunnel invert - The Cité Universitaire test site. Technical report, Ecole Centrale de Paris, 2002.

[4] E. Balmes. *Structural Dynamics Toolbox, User's Guide, Version 4*. Scientific Software Group, 2000.

[5] A. Bedford and D.S. Drumheller. *Elastic Wave Propagation*. John Wiley and Sons Ltd., 1994.

[6] P. Chatterjee and G. Degrande. Free field vibration measurements due to a test train at the site of Cité Universitaire in Paris. Report BWM-2002-09, Department of Civil Engineering K.U.Leuven, November 2002. CONVURT EC-Growth Project G3RD-CT-2000-00381.

[7] D. Clouteau. Interaction Sol-Structures. Cours de DEA Dynamique des Structures et Systèmes couplés, Ecole Centrale de Paris.

[8] D. Clouteau. *ProMiss 0.2: Manuel Scientifique*. Ecole Centrale de Paris, 2000.

[9] D. Clouteau. *ProMiss 0.2: Manuel Utilisateur*. Ecole Centrale de Paris, 2000.

[10] D. Clouteau, M. Arnst, and T.M. Al-Hussaini. Three-dimensional modelling of free field vibration caused by periodic tunnels in stratified media. *Journal of Sound and Vibration*, 2003. Submitted.

[11] D. Clouteau and D. Aubry. Propagation d'ondes dans les solides. Cours de DEA Dynamique des Structures et Systèmes couplés, Ecole Centrale de Paris.

[12] D. Clouteau and D. Aubry. *Computational Soil-Structure Interaction*, chapter 1. In press, 2001.

[13] C. Coster. *Finite element modelling of the Maison du Mexique*, chapter 4. Department of Civil Engineering K.U.Leuven, 2001.

[14] G. Degrande. Hc01 seismic wave propagation. Course notes.

[15] A.S. Bonnet-Ben Dhia and C. Hazard. Ondes dans les milieux continus. Cours de DEA Dynamique des Structures et Systèmes couplés, Ecole Centrale de Paris.

[16] J.F. Doyle. *Wave Propagation in Structures.* Springer Verlag, 1997.

[17] M.-L. Elhabre. *Modelisation de l'interaction sismique sol-fluide-parois moulées suivant une approche périodique.* PhD thesis, Ecole Centrale de Paris, 2001.

[18] J. Miklowitz. *The theory of Elastic Waves and Waveguides.* North-Holland publishing company, 1978.

[19] L. Pyl and G. Degrande. Determination of the dynamic soil characteristics with the SASW method at the site of Cité universitaire in Paris. Report BWM-2002-08, Department of Civil Engineering K.U.Leuven, October 2002. CONVURT EC-Growth Project G3RD-CT-2000-00381.

[20] L. Pyl and G. Degrande. Numerical modelling of traffic induced vibrations in buildings using a dynamic soil-structure interaction analysis. Report BWM-2002-11, Department of Civil Engineering K.U.Leuven, December 2002.

[21] P. Chatterjee S. Jacobs and G. Degrande. Vibrations due to service trains in the 'Maison du Mexique' on the RER B line at Cité Universitaire in Paris. Report BWM-2003-02, Department of Civil Engineering K.U.Leuven, February 2003. CONVURT EC-Growth Project G3RD-CT-2000-00381.

[22] N. Vincent, P. Bouvet, and J. Charlier. Convurt, development of excitation model. Technical report, Vibratec, 2002. CONVURT EC-Growth Project G3RD-CT-2000-00381.